

**BREATHING THERAPY AIR DELIVERY UNIT:
SIMULATION, DESIGN AND DEVELOPMENT**

David Edward White

Thesis submitted in partial fulfilment of the degree of Master of Engineering

**Auckland University of Technology
Auckland
New Zealand**

October 2003

This thesis contains confidential material. The thesis shall not be used, copied, given or conveyed to anyone who is not directly involved in the examination of this work.

Acknowledgments

Firstly, I would like to express my sincere gratitude to my supervisor, Dr Ahmed Al-Jumaily, who has mentored me through the labyrinth of post graduate study. His generosity and friendship, combined with seemingly unlimited patience, has enabled me to attain my goal.

I would also like to thank Lewis Gradon of Fisher & Paykel Healthcare, sponsors of my research project, for providing me with such an interesting project, also Doug Makinson, John Atkins and Mark Carter for patiently providing both time and equipment support when testing equipment.

Thanks also to Ross Reichardt, senior technician at the Auckland University of Technology, for his support during the manufacturing phase of the compressor.

My sincere thanks also go to my family for tolerating my frequently tired demeanour when occasionally I did manage to attend social gatherings.

Finally, and most importantly, I must thank my wife Kathy, who has never known me not to study, for her patience and understanding that for something to be of any worth, it must be gained at a cost.

Abstract

Although constant positive airway pressure therapy is currently the most effective form of non-invasive treatment to relieve obstructive sleep apnea symptoms, it has relatively low treatment compliance due to pressure related side effects.

Existing commercial continuous positive airway pressure (CPAP) devices rely on the combined airflow characteristics of both the air delivery unit and nasal mask vent to regulate treatment pressure. Fluctuation in mask pressure occurs however, due to patient breathing, presenting an opportunity to develop an alternative breathing therapy device capable of achieving dynamic control of mask pressure.

Within this research, a computer model of a proposed patient breathing therapy device, based on characteristics of a prototype system, is developed to determine the breathing system air delivery requirements whilst operating under a simulated patient breathing load. This model initially utilises an idealised, zero order, air delivery unit behaviour, since this system element is yet to be built.

A review of different types of air compressors is undertaken and the diaphragm type compressor selected as being best suited for practical implementation within the air delivery unit of the breathing system, based on constraints of air quality, available machining resource and materials. Thermodynamic design of the compressor is undertaken to determine physical dimensions and a range of actuation methods are reviewed, based on force and speed requirements. A speed controlled 3 phase AC induction motor is selected to actuate the compressor.

The diaphragm compressor is built and tested under both steady state and dynamic conditions and proven capable of meeting the breathing system air supply for both air pressure and flow requirements.

The air delivery unit within the model simulation, previously based on an idealised, zero order element, is characterised with the same dynamic behaviour as the prototype unit built, established during testing, and shown by simulation to meet the breathing system requirements under dynamic patient breathing load.

Implementation of the air delivery unit within the completed prototype breathing system shows the mask pressure to fluctuate outside the desired pressure tolerance range; however, to remedy this situation, the compressor requires the development of an appropriate control scheme which is beyond the scope of this work.

Table of Contents

Title Page	i
Acknowledgements	ii
Abstract	iii
Table of Contents	v
List of Figures	x
List of Tables	xiv
Nomenclature	xv
Chapter 1 Introduction	1
1.1 Background	1
1.2 Treatment	4
1.2.1 Oral Appliances	4
1.2.2 Surgery	6
1.2.3 Continuous Positive Airway Pressure	7
1.2.4 Bi-Level Positive Airway Pressure	10
1.2.5 Automatic Positive Airway Pressure	10
1.3 Literature Review	11
1.3.1 Positive Airway Pressure Devices	11
1.3.2 Sensing Methods	15
1.3.3 Improving CPAP Compliance	17
1.4 Research Objectives	19
Chapter 2 System Modelling	21
2.1 Introduction	21
2.2 Model Development	23
2.2.1 Reservoir	23
2.2.2 Transmission Tube	24
2.2.3 Mask	29

2.3	Justification of Neglected Terms	33
2.3.1	Compliance Effects	33
2.4	Closure	37
Chapter 3	Model Simulation	40
3.1	Introduction	40
3.2	SIMULINK Model	40
3.2.1	Air Delivery Unit	41
3.2.2	Reservoir and Transmission Tube	41
3.2.3	Nasal Mask	42
3.2.4	Patient	43
3.3	Dynamic Testing Model	43
3.3.1	Test Setup	43
3.3.2	Air Mass Flow Calibration	45
3.3.3	Pressure Transducer Calibration	46
3.3.4	System Dynamic Testing	47
3.3.5	Model Simulation	48
3.3.6	Results	50
3.3.7	Conclusions	51
3.4	Air Delivery Unit Specifications	52
3.4.1	Controller	52
3.4.2	Model Configuration	52
3.4.3	Results	53
3.4.4	Conclusions	55
3.5	Closure	55
Chapter 4	Air Delivery Unit	56
4.1	Introduction	56
4.2	Air Delivery Unit Selection	56
4.2.1	Non-Positive Type Air Compressors	57
4.2.2	Positive Type Air Compressors	58
4.2.3	Preliminary Considerations	59
4.3	Compressor Design	60
4.3.1	Compressor Thermodynamic Design	60
4.3.2	Swept Volume	61

4.3.3	Clearance Volume	62
4.3.4	Total Volume	62
4.3.5	Volume at Commencement of Induction	62
4.3.6	Effective Volume	63
4.3.7	Volume of Free Air Delivered	63
4.3.8	Maximum Air Mass Discharge Rate	63
4.4	Actuation Requirements	65
4.4.1	Diaphragm Gas Pressure Force	65
4.4.2	Power Requirement	65
4.5	Actuation Selection	66
4.5.1	Direct Acting Solenoid	66
4.5.2	Linear Motor	66
4.5.3	Oscillating Rotary Actuation	67
4.5.4	Continuous Rotary Actuation	68
4.5.5	Actuation Selection	71
4.6	Compressor Detailing	71
4.6.1	Design Detailing	71
4.7	Gear and Bearing Loads	73
4.7.1	Gear Design	73
4.7.2	Gear Forces	75
4.7.3	Gear Tooth Strength	77
4.7.4	Bearing Loads	80
4.8	Closure	81
Chapter 5	Testing Air Delivery Unit	82
5.1	Introduction	82
5.2	Steady State Compressor Testing	82
5.2.1	Test Setup	82
5.2.2	Results	84
5.3	Assembly of Air Delivery Unit	85
5.4	Dynamic Testing of Air Delivery Unit	85
5.4.1	Test Setup	86
5.4.2	Results	87
5.5	Completion of Prototype System	88
5.5.1	Pressure Transducer Selection	88

5.5.2	Final Assembly	90
5.6	Characterisation of Model Simulation	90
5.6.1	Air Delivery Unit	90
5.6.2	Mask Pressure Transducer	91
5.7	Model Simulation Dynamic Testing	91
5.7.1	Simulation Configuration	91
5.7.2	Simulation Results	91
5.8	ADU Implementation within Prototype	93
5.8.1	Test Setup	93
5.8.2	Results	95
5.9	Conclusions	97
5.10	Further Research	98
Appendices		100
Appendix A	Air Transmission Tube	100
A1	Tube Air Flow Resistance	100
A2	PVC Tube Properties	101
Appendix B	Air Supply Options	102
B1	Non-Positive Air Compressors	102
B2	Positive Type Air Compressors	105
B3	Regulated Air Supply	107
Appendix C	Compressor Actuation	109
C1	Direct Acting Solenoid	109
C2	Linear Motor	110
C3	Rotary Solenoid	111
C4	Stepper Motor	111
C5	Servomotor	112
C6	Speed Controlled DC Motor	112
C7	Speed Controlled AC Motor	113
C8	AC Induction Motor Specifications	113
C9	Motor Speed Controller Specifications	114
Appendix D	Design Details of Diaphragm Compressor	115
D1	Reed Valve Material	115
D2	Nylon Gear-Crank Material	116
D3	Diaphragm Material	117

D4	Compressor Drawings	118
Appendix E	ADU Dynamic Test Data	133
E1	ADU Test Results	133
Appendix F	Mask Pressure Transducer	134
F1	Application Data	134
F2	Operating Characteristics	135
F3	Compensation, Calibration and Signal Conditioning	136
References		137

List of Figures

Figure 1.1	Normal patient airway.	1
Figure 1.2	Obstructed patient airway.	2
Figure 1.3	Enlarged Uvula resting on base of tongue.	2
Figure 1.4	Elongated soft palate resting on base of tongue.	3
Figure 1.5	Mandibular repositioning device.	5
Figure 1.6	Tongue retaining device.	5
Figure 1.7	Jaw and tongue retaining device.	6
Figure 1.8	Commercially available CPAP ADU and humidification unit.	7
Figure 1.9	Schematic of typical CPAP device.	8
Figure 1.10	Patient oral CPAP.	8
Figure 1.11	Patient wearing nasal CPAP mask.	9
Figure 1.12	Typical nasal CPAP mask.	9
Figure 1.13	Fluctuation in CPAP nasal mask pressure.	10
Figure 1.14	Schematic of transient breathing system.	19
Figure 2.1	Block diagram of I-CPAP system model showing physical parameters considered.	22
Figure 2.2	Schematic representation of reservoir.	23
Figure 2.3	Fluctuating patient breathing load.	25
Figure 2.4	Schematic representation diagram of air transmission tube.	25
Figure 2.5	Schematic representation of air transmission tube test setup.	27
Figure 2.6	PVC tube, 5.5 mm internal diameter, airflow pressure drop.	28
Figure 2.7	Schematic representation of nasal mask.	30
Figure 2.8	Schematic representation of nasal mask vent flow test.	32
Figure 2.9	Comparison of predicted and measured mask vent flow characteristics.	32
Figure 2.10	Schematic representation of air transmission tube.	35
Figure 2.11	Tube divided into 10 lumps.	36
Figure 2.12	Percentage lumped air volume reduction within tube.	36

Figure 2.13	Block diagram of breathing system model.	39
Figure 3.1	SIMULINK I-CPAP breathing system model.	41
Figure 3.2	SIMULINK model of idealised air delivery unit.	41
Figure 3.3	SIMULINK model of reservoir and transmission tube.	42
Figure 3.4	SIMULINK model of nasal mask.	44
Figure 3.5	Schematic representation of prototype I-CPAP system test setup.	44
Figure 3.6	Orifice plate calibration air mass flow curves.	46
Figure 3.7	Orifice plate calibration prediction over normal system air mass flow range.	47
Figure 3.8	System and model simulation dynamic test response.	50
Figure 3.9	Model simulation controller modes.	52
Figure 3.10	Model simulation air pressure and flow results.	53
Figure 4.1	Finite element model of diaphragm stress at 5mm displacement.	60
Figure 4.2	Typical diaphragm compressor pressure-volume cycle.	61
Figure 4.3	Diaphragm swept volume measured at extremes of stroke.	62
Figure 4.4	Schematic representation of oscillating rotary actuator mechanism.	69
Figure 4.5	Schematic representation of continuous rotary actuator crank mechanism.	69
Figure 4.6	Sectional view of diaphragm compressor.	72
Figure 4.7	Completed diaphragm compressor.	73
Figure 4.8	Schematic representation of compressor crank-gear actuator arrangement.	74
Figure 4.9	Side view of offset idler half-width gears.	74
Figure 4.10	Gear crankshaft dimensions.	76
Figure 4.11	Gear forces.	77
Figure 4.12	Gear strength analysis.	78
Figure 4.13	Bearing radial loads due to diaphragm air pressure force.	80
Figure 5.1	Schematic representation of steady state compressor test setup.	83
Figure 5.2	Steady state testing of diaphragm compressor.	83
Figure 5.3	Steady state compressor performance over range of speeds.	84
Figure 5.4	Completed air delivery unit.	85
Figure 5.5	Schematic representation of ADU dynamic test setup.	86
Figure 5.6	Photo of ADU dynamic test setup.	87
Figure 5.7	Dynamic response of ADU.	87
Figure 5.8	Pressure transducer mounted on nasal mask.	89

Figure 5.9	Completed prototype I-CPAP breathing system.	90
Figure 5.10	Characterised ADU model element within model simulation.	91
Figure 5.11	Model simulation mask pressure under simulated patient breathing load.	92
Figure 5.12	Schematic representation of patient breathing simulator.	93
Figure 5.13	Schematic representation of simulated patient test setup.	94
Figure 5.14	Patient simulation test setup.	94
Figure 5.15	Patient breathing simulator connected to prototype system.	98
Figure 5.16	Comparison between prototype and characterised model simulation mask pressures utilising lower controller gain setting.	96
Figure A1	5.5 mm tube air flow resistance based on velocity.	100
Figure B1	Fan air output characteristics.	102
Figure B2	Commercial centrifugal fan performance curve.	103
Figure B3	Pictorial view of regenerative fan.	103
Figure B4	Sectional view of regenerative fan.	104
Figure B5	Regenerative fan performance graph.	105
Figure B6	Schematic of diaphragm compressor operation.	106
Figure B7	Two-stage stepper motor driven diaphragm air compressor.	107
Figure C1	LEDEX H1 STA 1" diameter x 2" direct acting solenoid performance specifications.	109
Figure C2	LEDEX 6EC low profile solenoid performance graph.	109
Figure C3	LEDEX soft-shift 6EP solenoid performance graph.	110
Figure C4	Performance characteristics for platen-type linear actuator.	110
Figure C5	Torque characteristics of LEDEX 6EV BTA solenoid.	111
Figure C6	LEDEX Ultimag 6EM rotary solenoid torque output.	111
Figure C7	Typical torque output for hybrid stepper motor.	111
Figure C8	MOOG model G412-2xx servomotor performance graph.	112
Figure C9	Shunt wound DC motor operating characteristics.	112
Figure C10	Series wound DC motor operating characteristics.	112
Figure C11	AC induction motor operating characteristics.	113
Figure D1	Detail drawing of diaphragm outer housing.	118
Figure D2	Detail drawing of inner housing.	119
Figure D3	Detail drawing of full width gear.	120
Figure D4	Detail drawing of half width gear_1.	121
Figure D5	Detail drawing of half width gear_2.	122

Figure D6	Detail drawing of bearing, shafts and pins.	123
Figure D7	Detail drawing of diaphragm piston link.	124
Figure D8	Detail drawing of ported piston.	125
Figure D9	Detail drawing of valve small hole and countersunk washer.	126
Figure D10	Detail drawing of discharge housing.	127
Figure D11	Detail drawing of connecting rod.	128
Figure D12	Detail drawing of ported diaphragm.	129
Figure D13	Detail drawing of countersunk ported piston.	130
Figure D14	Detail drawing of air outlet adaptor.	131
Figure D15	Diaphragm compressor assembly.	132
Figure E1	ADU response, test 1.	133
Figure E2	ADU response, test 2.	133
Figure F1	Motorola mask pressure transducer configuration data.	134
Figure F2	Motorola mask pressure transducer operating characteristics.	135
Figure F3	Motorola mask pressure transducer compensation, calibration and conditioning data.	136

List of Tables

Table 3.1	Test equipment details.	45
Table 3.2	Computer simulation parameters.	49
Table 3.3	Model simulation ADU delivery pressure and mass flow rates over patient breathing cycle.	54
Table 3.4	Model simulation controller settings.	54
Table 4.1	Summary of diaphragm compressor thermodynamic design specifications.	64
Table 4.2	Comparison between design and manufacturer maximum stress levels for GS nylon 66 gears	80
Table 5.1	Details of equipment used in steady state compressor test.	84
Table 5.2	Details of equipment used in ADU dynamic test.	86
Table 5.3	Controller settings predicted by model simulation.	92
Table 5.4	Details of equipment used in test.	95
Table 5.5	Variation in prototype and model simulation controller settings.	96
Table A1	Properties of flexible PVC tube.	101
Table C1	Performance specifications for commercial linear servomotor.	110
Table C2	Compressor motor technical data.	113
Table C3	Speed controller general specifications.	114
Table D1	KKPC Kuhmo GP 125H high transparency GPPS specifications.	115
Table D2	Nylatron® GS nylon, type 66, MoS2 filled, specifications.	116
Table D3	Neoprene nylon diaphragm material.	117

Nomenclature

A_b	Cross sectional Area of mask bias vent hole.	m^2
A_t	Cross sectional Area of tube.	m^2
C	Speed of sound.	m/s
C_{brg}	Basic specified bearing load.	N
C_d	Coefficient of discharge.	
C_r	Reservoir capacitance.	kg/Pa
C_m	Mask Capacitance.	kg/Pa
C_p	Specific heat capacity during constant pressure process.	$J/kg.K$
C_v	Specific heat capacity during constant volume process.	$J/kg.K$
D	Gear pitch diameter.	m
d_t	Tube inside diameter.	mm
D_{min}	Gear tooth root diameter.	m
D_{max}	Gear tooth major diameter.	m
dP_f	Pressure drop due to friction.	Pa
F_c	Maximum compressor con-rod force.	N
F_r	Total gear radial force.	N
F_s	Gear separating force.	N
F_t	Gear tangential force.	N
F_{br}	Bearing radial force.	N
g	Gravity.	ms^{-2}
h_f	Pressure head lost to friction.	m
I	Tooth root second moment of area.	M^4
J	Gear tooth addendum height.	m
K	Gear tooth dendendum height.	m
k_s	Pressure loss shock factor.	
L_t	Tube length.	m
L_{10}	Basic rated bearing life.	10^6 rev

m	Gear module.	
\dot{m}_c	Compressor air mass flow rate.	kg/s
\dot{m}_b	Mask bias air flow mass flow rate.	kg/s
$\dot{m}_{c,max}$	Maximum compressor air discharge mass flow rate.	kg/s
\dot{m}_t	Tube air mass flow rate.	kg/s
\dot{m}_p	Patient air mass flow rate.	kg/s
M	Mach number.	
m_m	Mask air mass.	kg
m_r	Reservoir air mass.	kg
N	Number of gear teeth.	
n	Number of mask bias vent holes.	
n_{max}	Maximum compressor speed.	rev/min
P_a	Diaphragm air pressure.	Pa
P_{brg}	Basic specified bearing load.	N
P_f	Free air pressure.	Pa
P_r	Reservoir air pressure.	Pa
P_m	Mask air pressure.	Pa
P_t	Tube air pressure.	Pa
P_1	Compressor inlet air pressure.	Pa
P_4	Compressor discharge air pressure.	Pa
Q_b	Mask bias flow volume flow rate.	m^3/s
R_a	Gas constant for air.	J/kg.K
R_b	Gradient of linear mask bias vent model prediction.	Pa/kgs^{-1}
R_m	Gradient of tube mass flow pressure drop model.	Pa/ms^{-1}
R_v	Gradient of tube velocity pressure drop model.	Pa/gs^{-1}
S_c	Compressor stroke offset.	m
T	Torque.	N-m
T_a	Compressor actuator torque.	N-m
t	Tube wall thickness.	mm
T_r	Absolute reservoir Temperature.	K
T_m	Absolute mask temperature.	K

V	Volume of each tube lump.	m^3
V_f	Volume of free air delivered.	m^3
V_m	Mask volume.	m^3
V_r	Reservoir volume.	m^3
V_t	Tube air velocity.	m/s
V_1	Compressor total volume.	m^3
(V_1-V_3)	Compressor Swept volume.	m^3
V_3	Compressor clearance volume.	m^3
V_4	Compressor volume and commencement of induction.	m^3
W_d	Diaphragm work.	J
W_{max}	Maximum compressor power requirement.	W
Y_b	Y intercept of mask bias flow linear model.	Pa
Y_m	Y intercept of tube pressure drop mass linear model.	$Pa/g s^{-1}$
Y_v	Y intercept of tube pressure drop velocity linear model.	$Pa/m s^{-1}$
β_a	Bulk modulus of air.	Pa
$\beta_{a,eff}$	Effective air/tube bulk modulus.	Pa
β_t	Bulk modulus of tube.	Pa
ε	Tube roughness.	mm
γ	Ratio of specific heats.	
ρ_a	Air density.	kg/m^3
$\rho_{a,ave}$	Average air density.	kg/m^3
η_{vol}	Compressor volumetric efficiency.	%
σ_t	Gear tooth bending stress.	Pa
$\sigma_{t,max}$	Principal bending stress at tooth root.	Pa
τ_t	Gear tooth shear stress.	Pa
$\tau_{t,max}$	Principal shear stress at tooth root.	Pa

Chapter 1 Introduction

1.1 Background

Sleep apnea, deriving its name from the Greek word apnea meaning ‘want of breath’, is used to describe a breathing disorder that causes interruption to breathing whilst sleeping [1]. This syndrome is defined as a reduction of respiratory movements by 95% for more over a ten seconds period, whereas, a decrease of at least 50% over the same time period is defined as hypopnoea [2]. Apnea can be categorised as either central sleep apnea, where the brain fails to send the appropriate message to the breathing muscles or obstructive sleep apnea (OSA) where the breathing airway is obstructed, restricting the air flow to and from the lungs. Physiological problems characterising OSA vary; however, obesity in the patient commonly causes blocking of the airway opening with a relaxed throat or tongue muscle, resulting in laboured breathing or choking occurring [1]. During sleep, when the patient reclines, the patient’s airways offer multiple sites where obstruction can occur, including an elongated and enlarged soft palate impinging against the oropharynx and nasopharynx, Figures 1.1 and 1.2.

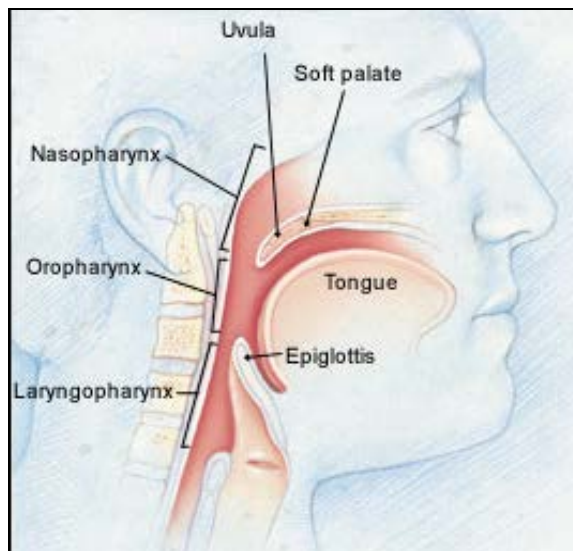


Figure 1.1 Normal patient airway [3].

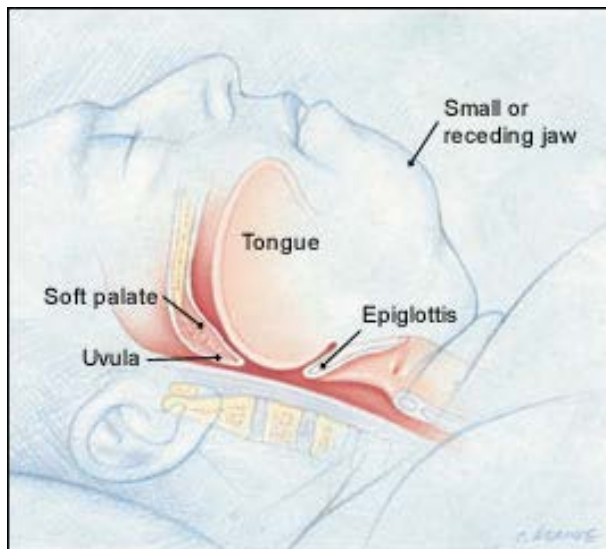


Figure 1.2 Obstructed patient airway [3].

Other physical attributes, apart from obesity, can contribute to the likelihood of suffering OSA, including an enlarged uvula resting on the base of the tongue, along with hypertrophied tonsils, Figure 1.3. An elongated soft palate can also rest on the base of the tongue, Figure 1.4, causing an obstruction to the breathing airway. Lower face abnormalities such as receding jaw as well as large tongue can also contribute to the likelihood of OSA occurring [1].

In the western world, approximately 4% of middle aged men and 2% of middle aged women suffer OSA, effecting over 20 million adult Americans [4]. This group is also most likely to be overweight, have high blood pressure or some abnormality in the upper airway.

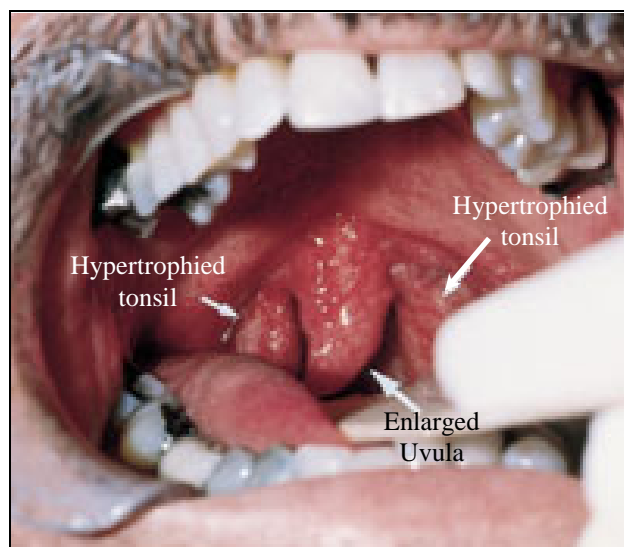


Figure 1.3 Enlarged Uvula resting on base of tongue [3].

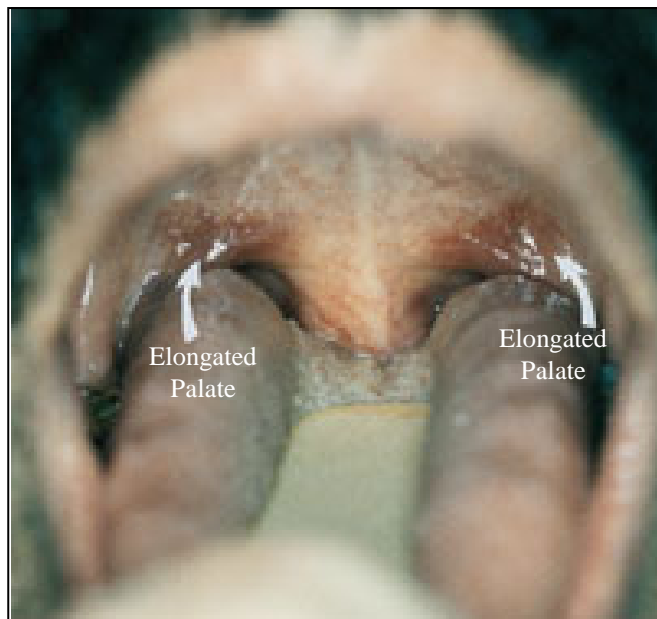


Figure 1.4 Elongated soft palate resting on base of tongue [3].

Pauses in breathing causes low oxygen and high carbon dioxide levels in the patient's lungs, triggering an alert within the brain to urgently commence breathing; interrupting the normal sleeping pattern. As many as 60 or more involuntary pauses in breathing can occur each hour with each 'apneic event' being almost always accompanied by snoring. Continual interruption to the normal deep sleeping pattern causes excessive sleepiness whilst awake and this has been associated with irregular heartbeat, high blood pressure, heart attack and stroke [1]. When untreated, OSA sufferers are 3 times as likely to have car accidents as well as suffer other symptoms such as irritability, depression, sexual dysfunction, learning and memory difficulty. Falling asleep whilst at work or on the phone, another commonly misdiagnosed OSA symptom, cannot be treated by sleeping pills which, rather than improving sleep quality, increase both the frequency and duration of breathing pauses [3].

The diagnosis of OSA is not simple since there are many different reasons, many not physical, why sleep may be disturbed so a technique called nocturnal polysomnography is commonly utilised [3,5]. Here the patient sleeps in a controlled environment whilst various parameters are monitored. Equipment and techniques typically used to identify OSA events, when chest movement fails to produce a corresponding airflow and oxyhemoglobin de-saturation occurs, include:

- Eye movement observations, to detect rapid-eye-movement sleep.
- Electroencephalogram, to measure arousals from sleep.
- Chest wall monitors, to document respiratory movements.

- Nasal and oral air flow measurements.
- Electrocardiogram to measure heart beat.
- Electromyogram to measure limb movements that cause arousals.
- Oximetry to measure oxygen saturation.

The results of nocturnal polysomnography generate a respiratory disturbance index (RDI) which expresses the number of abnormal respiratory events per hour of sleep with 20 being the minimum level commonly considered as requiring some form of treatment [3]. The recent development of artificial neural networks [2] has enabled automatic diagnosis of breathing patterns from polysomnographic information and is now frequently used to detect the occurrence of apnea or hypopnea events.

1.2 Treatment

Treatment of OSA can vary, depending upon a range of factors; however, in all cases the goal is to remove the airway obstruction. Costs play a significant part in determining an appropriate method of OSA treatment, with surgery to either remove soft tissue from the throat or open up an alternative air path through the windpipe, usually being avoided due to cost, even though the remedy may be permanent. Less invasive forms of treatment such as the use of dental appliances to reposition the jaw and tongue [5] or the use of air pressure to hold the airway open, is a popular choice of therapy. This is likely due to both the low costs involved and the avoidance of unpleasant surgery.

1.2.1 Oral Appliances

Although not always effective in treating patients suffering from OSA, oral devices provide a cheap and easy alternative to other forms of treatment. Oral appliances can be divided into two main groups:

- a) The mandibular repositioning devices (MRD), Figure 1.5, is the largest group of oral treatment devices, which operate by tightly fitting over the patient's teeth and pulling the bottom jaw forward, holding the teeth in the closed position.

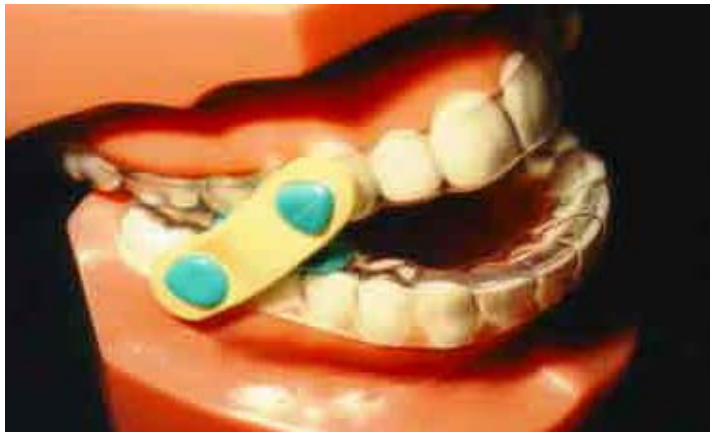


Figure 1.5 Mandibular repositioning device [6].

MRD treatment is suited to OSA sufferers who have normal sized tongues and soft palates since the jaw is pulled forward, moving soft tissue away from the airway opening. Complications can occur with this form of treatment including loosened teeth, joint pain, muscle aches and tissue sores [6].

- b) The tongue retaining device (TRD), Figure 1.6, is used in patients suffering from OSA who have either very large tongues, no teeth or chronic joint pain, making them not suited to MRD oral devices [6]. The TRD works by the patient's teeth (or gums) compressing a soft polyvinyl bubble shaped device, creating a cavity that projects beyond the lips. The patient then sticks their tongue into the bubble, displacing the air, and thus holding the tongue in the projected position.



Figure 1.6 Tongue retaining device [6].



Figure 1.7 Jaw and tongue retaining device [6].

- c) A variation on the TRD, the jaw and tongue retaining device, Figure 1.7, utilises two separate appliance portions, each fitted to the top and bottom row of teeth. The patient simply projects the jaw forward, with their tongue placed behind the lower teeth, until the two portions lock together, trapping the tongue and jaw away from the airway [6].

1.2.2 Surgery

Surgery to remedy OSA is normally used in young patients or those who cannot tolerate using any of the non-invasive forms of treatments. Uvulopalatopharyngoplasty (UPPP) involves the removal of parts of the uvula, soft palate and any other redundant soft tissue including the tonsils, if deemed necessary [3]. This procedure often eliminates snoring, however, it may not always treat OSA since other parts of the air way may be causing the obstruction. Laser-assisted uvuloplasty (LAUP) has become more popular than UPPP since it allows the surgery to be progressively completed over several sessions at a doctor's surgery, eliminating the need for hospitalisation.

More invasive surgical procedures, such as genioplasty where the tongue is pulled forward, are normally conducted when more conservative forms of OSA treatment have failed. In extremely severe cases, a tracheotomy, where an air pipe is inserted directly into the patient's lower airway, may be considered due to the high rate of mortality associated with suffers of extreme OSA.

1.2.3 Continuous Positive Airway Pressure

The use of continuous positive airway pressure (CPAP) therapy, where the patient breathes air pressurised slightly above atmospheric pressure, effectively prevents collapse or blocking from occurring by forming a pneumatic splint within the patient's breathing airways and is the most common form of OSA treatment. The CPAP therapy device, Figures 1.8 and 1.9 respectively, consists of an air delivery unit (ADU), typically a centrifugal fan, supplying low pressure air to the nasal mask via a 20mm internal diameter flexible plastic hose. Frequently, an air reservoir containing water is utilised between the fan and mask to humidify the breathing air, preventing the patient's airways becoming dry and irritated [3].

The level of air pressure required for CPAP treatment is frequently a trade-off between being sufficient to prevent obstruction of the airway whilst minimising pressure related side effects. Typical CPAP titration air pressures range from 6 to 20 cm water gauge (Wg) [7]. The prescribed CPAP mask air pressure is determined by nocturnal polysomnography testing of each patient to determine the minimum CPAP titration pressure required to prevent OSA from occurring.



Figure 1.8 Commercially available CPAP ADU and humidification unit [8].

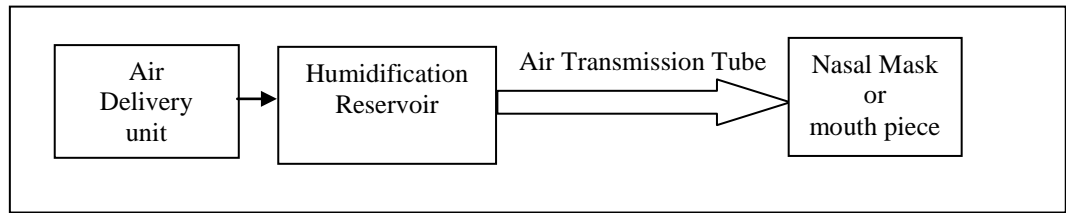


Figure 1.9 Schematic of typical CPAP device.

The CPAP therapy can be applied to the patient either orally (O-CPAP), Figure 1.10, or through the nasal mask (N-CPAP), Figure 1.11, the latter having the advantage of avoiding drying of the patient's throat due to the continuous airflow. Despite using a nasal mask, some patients develop dry mucus membranes; however, this problem can be reduced by humidification of the air flowing into the mask [3].

To date, CPAP is the treatment preferred by most patients suffering OSA since it is currently the most effective form of treatment [9]; however, the method of management is dependant upon the patient response not including any adverse pressure related effects [3].



Figure 1.10 Patient oral CPAP [6].

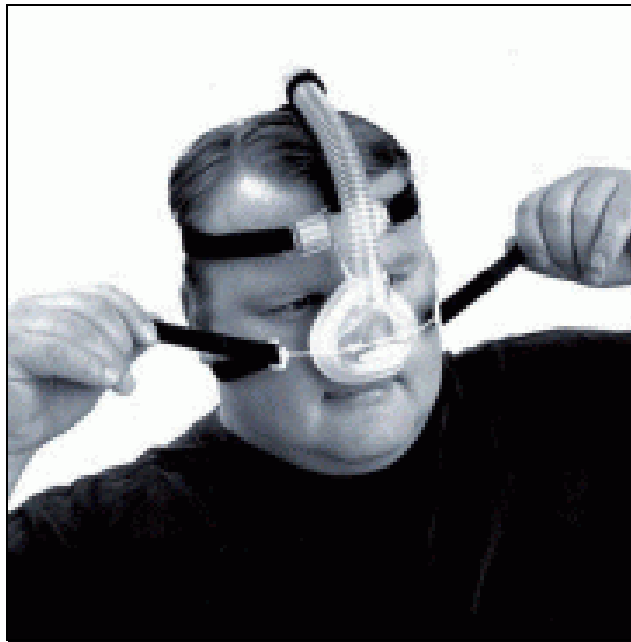


Figure 1.11 Patient wearing nasal CPAP mask [10].

The N-CPAP mask, Figure 1.12, utilises continuous vent airflow through 8 fixed orifices, ensuring continuous purging of the air contained within the mask. Unfortunately, the operational characteristics of the fixed orifice mask vents permit the mask pressure to fluctuate as a result of both the patient's breathing and the pressure flow characteristics of the centrifugal fan used within the CPAP ADU. The results of testing a commercially available CPAP unit, Figure 1.13, shows regular fluctuations occurring in mask pressure under simulated patient breathing load.



Figure 1.12 Typical nasal CPAP mask.

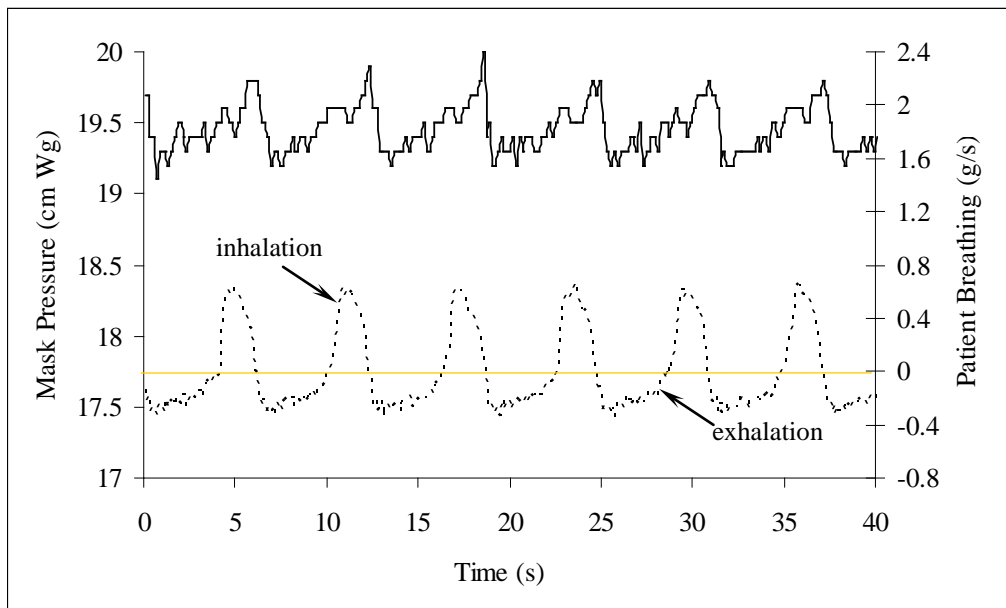


Figure 1.13 Fluctuation in CPAP nasal mask pressure;— mask air pressure,— — patient breathing.

1.2.4 Bi-Level Positive Airway Pressure

Bi-level positive airway pressure (Bi-PAP) breathing therapy devices operate in a similar fashion to CPAP devices with the exception of offering two air output pressure levels from the ADU. By utilising a flow sensor, such as a thermistor within the ADU outgoing air stream, the air delivery pressure can be alternated between preset higher and lower values during patient inhalation and exhalation, respectively. This variation in supply pressure is usually achieved by altering the ADU fan speed and results in a relatively constant mask pressure being achieved despite the fluctuating patient breathing load.

1.2.5 Automatic Positive Airway Pressure

Developments have been made to CPAP devices to achieve an automatic positive-pressure airway pressure (APAP) control. These devices sense nasal mask pressure and appropriate control action is taken by the ADU, typically achieved by altering the fan speed, enabling mask pressure to be progressively reduced during periods of absence of apnoeic events [11].

APAP therapy systems are effectively conventional CPAP devices modified to include the attachment of a sensing tube to the nasal mask, the other end of which

is connected to a pressure sensor and micro-controller contained within the ADU [11]. The mask pressure transducer has two functions:

1. Sensing of mask air pressure.
2. Detection of pharyngeal wall vibration (PWV); signalling the onset of OSA, through filtering of the pressure signal to eliminate background noise.

The PWV detection algorithm, used to analyse the processed pressure – time signal, considers both the time duration of the latest signal to the previous 10 recorded signals. Detection of an apnea event is achieved by the APAP micro-processor examining the processed signal for three consecutive PWV episode signals with no more than 20 seconds between any two signals. If the signal exceeds the respective thresholds of time and magnitude then the mask air pressure is raised by 2 cm Wg. Conversely, when after a time period of 5 minutes, the area and duration of the processed signal does not exceed the two threshold parameters then the air pressure is lowered 1 cm Wg until a pre-set minimum mask pressure is reached.

Unlike other forms of air pressure therapy, APAP treatment is intended to continuously take corrective action over a period of time and offers the advantage, over conventional CPAP therapy, of reduced adverse pressure related side effects due to lower average mask air pressures. It does not, however, offer any remedy for fluctuations in mask pressure due to the fluctuating patient breathing load.

1.3 Literature Review

Extensive literature review has been undertaken on positive airway pressure therapy devices, methods utilised to sense patient breathing effort and treatment compliance.

1.3.1 Positive Airway Pressure Devices

The high efficacy of CPAP has established this form of therapy as the gold standard in treating OSA [9]; however, despite this effectiveness, over 40% of

patients using this form of treatment find it difficult to use over long periods due to pressure related side effects which include abdominal bloating, sore eyes and headaches [1]. A Comparative test between MRD type oral appliances and CPAP treatment methods, on study group of 20 patients suffering from OSA [12], found that the MRD treatment was successful in treating 55 % of the patients whilst 5 % were compliance failures, defined as unable or unwilling to use the treatment. When the same group undertook CPAP therapy it resulted in a 70 % treatment success rate, however, the remaining 30 % of patients were compliance failures. This result confirms the effectiveness of CPAP therapy; however, also highlights the long term acceptance by patients to this form of treatment as being poor. Recent research indicates that long term CPAP therapy compliance is lower than 68% [9].

Maintaining control of CPAP treatment mask pressure must improve patient comfort since pressure related side effects contribute significantly to the poor CPAP therapy compliance. The air flow characteristics of the small mask vent orifices provided within the mask, designed to ensure continuous purging of the mask air contribute to the fluctuation in air pressure experienced in N-CPAP systems. Variation experienced in mask air pressure is predominately due to the mask vent air flow characteristics failing to match the fluctuating patient breathing load. Testing of 8 commercial CPAP therapy devices has shown that mask pressure fluctuates from -1.3 to + 5.6 cm Wg around the desired set point during simulated patient breathing load [13]. Because of this pressure fluctuation, conventional CPAP therapy requires the mask to operate at a mean pressure higher than that prescribed to ensure the minimum air pressure is always maintained.

Other research has confirmed that both improved patient comfort and treatment compliance occurs when mask pressure is stabilised, achieving this by cycling inspiration pressure higher than expiration pressure to produce a reduced patient breathing work load [14]. Bi-PAP breathing devices modify the timing of the nasal mask pressure fluctuations to follow the natural breathing pattern, resulting in a relatively stable mask pressure when the patient breathes. These devices are often more comfortable for the patient to use, when compared to CPAP therapy devices [4]. Comparative testing of 4 commercial Bi-PAP devices, under the

same conditions, has shown the mask pressure to fluctuate from -1 to -0.3 cm Wg, significantly less than that experienced by the CPAP breathing systems [13]. Research into other benefits of Bi-PAP therapy has shown that morbidly obese patients, suffering OSA, are more likely to respond to this form of treatment than CPAP therapy [15].

An alternative development of the CPAP breathing system is continuous automatic positive airway pressure (APAP) control of mask pressure, where, rather than switching between two pre-determined mask pressure levels to accommodate the fluctuating patient breathing load, as in Bi-PAP devices, APAP systems dynamically control mask air pressure. Studies have shown that the patient's body position also causes variation in the incidence of OSA, APAP attempts to accommodate this variable and achieve a lower average nasal mask air pressure, reducing the occurrence of pressure related side effects [11].

Early work on APAP systems utilised a controller capable of proportional integral and derivative (PID) action to regulate ADU fan speed. With these systems it is possible to locate the mask pressure sensor at the ADU air outlet rather than at the mask due to the low air pressure drop experienced across the ends of the large 20 mm diameter air transmission tube. The objectives of this early system was to both produce a stable mask pressure, despite fluctuating patient breathing load and adjust the ADU to accommodate any mask leaks by dynamically controlling the air output. Subsequent testing of this system found the response time of the fan was too slow, taking as much as 2.5 seconds to react to reductions in mask air pressure changes. This effect was contributed to the reliance on frictional and fan forces to slow the fan [16].

Later APAP systems do not try to stabilise the fluctuating mask pressure, rather, these systems attempt to minimise the mean mask air pressure, to a pre-set level, during periods of absence of OSA occurring [11]. This is achieved by analysing the signal from a pressure transducer, mounted in the nasal mask, over a specified time period before appropriate control action is taken by the ADU controller. This method of control results in mask air pressure being reduced, by a set increment, if PWV is not detected during the measured time period. With ADU control action being based on PWV detection, variations in fan speed occur

gradually so speed of response is not an issue as described with earlier APAP systems. Current nasal mask design, utilised in all commercial air pressure therapy systems, rely on fixed vent holes to continually purge mask air, however, since APAP devices operate the mask at lower mean pressures than both CPAP and Bi-PAP systems this results in smaller fluctuations in mask pressure occurring.

An APAP device was randomly tested on 10 patients, 5 of whom were diagnosed as suffering from OSA and undertaking CPAP therapy. APAP therapy effectively reduced the mean air treatment pressure from 12.6 cm Wg, prescribed for conventional CPAP therapy, to a lower value of 6.8 cm Wg [11]. This result was confirmed later when APAP therapy provided a significant reduction in mask air pressure to successfully treat OSA in a sample of patients compared to previous CPAP therapy [7]. Although no testing could be found comparing patient therapy compliance between CPAP and APAP treatment it is obvious that a 50% reduction in mask pressure must improve patient comfort as well as relieve pressure related side effects.

A problem encountered with some of the APAP devices tested was attenuation of the pressure signal, due to the long small diameter tube connecting the nasal mask to the pressure transducer, giving poor detection of PWV [11]. Another unavoidable factor also considered to affect the detection of PWV was the natural damping present within the patient upper airway. To reduce the pressure attenuation effect experienced along the long thin tube, it was felt that the pressure transducer should be located as close as practical to the nasal mask.

A variation to APAP treatment, capable of maintaining nearly constant mask pressure throughout the patient breathing cycle, is achieved by the use of air jet flow control valves connected to the mask air supply [17]. This system permits dynamic changes in mask air pressure to be made in phase with the patient breathing without the delays inherent with changing fan speed, as experienced in earlier APAP systems. Here, the mask air in-flow is controlled by an inspiratory demand flow valve whilst the rate of air outflow is controlled by an opposing air jet flow. A pressure transducer, connected via a pipe to the ADU output, sends a pressure signal to a microcomputer. The computer compares the prescribed mask

pressure level to the signal pressure every 5 ms, when the mask pressure is below that desired; the inspiratory demand flow valve permits air flow from the ADU. When mask pressure drops below the desired level, the air jet flow from the ADU opposes the outflow of air from the mask, increasing the mask pressure. Testing has shown that this type of APAP device has smaller mask pressure fluctuations, during patient breathing, compared to conventional CPAP devices.

Recent research has found, however, that although improvements in patient compliance have been reported in random trials comparing APAP devices to CPAP therapy, there was no difference in objective outcome, such as subjective sleepiness and it was felt that the additional cost of this device was not justified [18].

1.3.2 Sensing Methods

The sensing method used in Bi-PAP and APAP breathing therapy devices is different since the two systems are effectively controlling different system variables, the former controls the air flow whilst the latter controls air pressure. Within this section a review is undertaken on the different sensing methods utilised in Bi-PAP, APAP and mechanical ventilation devices.

As previously mentioned, Bi-PAP systems try to synchronise a step change in ADU delivery pressure between two pre-set values of air pressure, offsetting the effect fluctuating patient breathing load has on mask pressure. Typically, Bi-PAP systems utilise a thermistor to sense air mass-flow from the ADU since this parameter is in phase with the patient's breathing. In contrast, APAP systems utilise a single pressure sensor at the mask to enable both the detection of PWV and mask pressure to be achieved through complex signal processing. Other forms of OSA detection have previously been proposed, but have not yet found application in commercially available Bi-PAP and APAP breathing therapy devices.

Within Bi-PAP devices, alternatives to the use of a thermistor to sense air flow have been successfully implemented, including the passive acoustic sensor. This device consists of two microphone elements exposed to the air flow stream and

connected in a bridge configuration to detect air flow as low frequency noise [19]. This method has the advantage over remote flow sensing of being able to use long transmission tubes, if required, without the problem of signal delay occurring. Another acoustic air flow sensing method utilises two ultrasonic waves, travelling in opposite directions within the air flow stream. The air flow rate is determined by measuring difference in transmission time between the opposing waves. A range of clinical trials have shown the passive acoustic sensor capable of detecting between 52 – 82% of all OSA events.

To help identify possible alternatives to the existing methods of sensing patient breathing, currently utilised in commercial Bi-PAP and APAP devices, methods used to trigger mechanical ventilation, where patient breathing effort is sensed, is also reviewed. Typically a patient receives mechanical ventilation, controlling both air volume and pressure, for reasons other than to relieve OSA symptoms, however, in both cases the goal is to ensure efficient filling of the lungs. Computer modelling of a two compartment human lung system, with unequal time constants, has shown the volume-control ventilation to achieve a more even filling of the lungs compared to pressure-control ventilation, despite differing lung compliances, suggesting this method is superior in filling the lungs [20].

A study of both the accuracy and sensitivity of devices used to detect breathing effort in newborn babies, during mechanical ventilation, indicates existing trigger methods are prone to lacking sensitivity to detect small breathing effort and tend to falsely initiate mechanical breathing if the ventilator trigger sensitivity is set higher [21]. There are two methods commonly employed to detect patient breathing effort through abdominal movement during mechanical ventilation. The first being a Graseby capsule, a small flat plastic capsule which is filled with foam and tightly taped to the abdomen of the patient. Here, breathing effort compresses the capsule, causing a rise in tube pressure that is sensed [21]. An alternative to the Graseby capsule is an induction type sensor that detects breathing effort by minute variation in distance between a coil and magnet taped to the front and back of the abdomen respectively. With this method, the trigger signal is initiated by movement of the abdomen which occurs prior to inspiratory air flow, resulting in a negative trigger delay since initiation of air flow is deemed to be the commencement of inspiration. Testing of this trigger method shows that any

abdominal motion, such as random physical activity, could falsely create a trigger signal. Despite this problem, recent research has found the phase relationship between abdominal and thoracic excursion to be an effective method of detecting the formation and occurrence of an apnoeic event [22].

The measurement of patient breathing tidal volume by an anemometer attached to the endotracheal tube, supplying air to the patient, is an alternative ventilation triggering method used to measure air mass flow. This method operates in the same way as the thermistor sensor used in Bi-PAP therapy devices and is considered to be both robust and the least susceptible to false triggering due to body motion [21]. The signal response time for the anemometer trigger method is instantaneous whilst the response time of the volume flow method is considered satisfactory, taking approximately 135 ms to trigger after inhalation occurred.

Transthoracic impedance offers an alternative method to the direct measurement of airflow by sensing patient breathing effort through the attachment of electrodes mounted in pairs on the patient's skin. One electrode injects current, at a known amplitude and frequency, whilst the other electrode, mounted across the patient's chest, detects breathing through variations in electrical impedance [23]. Testing has shown this technique is not capable of differentiating between hypopnoea and OSA events and problems included the interference of cardiac activity and random body activity results in the greatest rate of false triggering out of all the ventilation triggering methods tested. A review of commercially available home breathing therapy devices fails to find any of the mechanical ventilation triggering methods implemented within OSA air pressure therapy devices.

1.3.3 Improving CPAP Compliance

Many healthcare providers consider patient non-compliance to be the biggest problem with CPAP therapy, based on patients using the machine only a few hours each night or a few days each week [3]. Despite perceived discomfort appearing to be the main cause of treatment failure, patients suffering severe OSA are often more compliant than mild sufferers due to the benefits of treatment success.

Recent sleep laboratory studies, comparing patient response to CPAP and APAP treatment has shown all the patients benefited from air pressure therapy; however, variations occurred in the patients' sleep response to either form of treatment [24]. These results were confirmed by later studies which also indicated patient compliance improved when lower mean mask pressures were used and suggested that long-term studies could quantify the beneficial effects, such as greater comfort and reduction in cardiac strain, for the patient when mask pressure was reduced [25,26].

There is an opportunity to produce an improved CPAP (I-CPAP) breathing therapy device, capable of achieving a constant nasal mask pressure despite the fluctuating patient breathing cycle, to improve patient treatment compliance. This will be achieved by combining the mask pressure sensing system used in APAP systems with the variable output ADU, similar to that utilised in Bi-PAP devices. This system will also feature the replacement of the large 20 mm internal diameter air transmission hose, currently utilised in all CPAP and APAP devices to supply the mask, with a smaller, less intrusive, 5.5 mm internal diameter PVC tube, to further improve patient comfort. The I-CPAP ADU will, however, be required to generate greater air pressure than existing systems in order to overcome the additional air flow resistance offered by the small diameter air transmission tube.

Earlier research work, undertaken in conjunction with Fisher & Paykel Healthcare [27], based on computer simulation, has proven the feasibility of implementing a transient breathing system, Figure 1.14. The goal of this system was to maintain mask air pressure within ± 0.5 cm Wg of the desired value whilst the patient is breathing by utilising pressure feedback control of the ADU. An idealised positive displacement variable stroke compressor, with stroke ranging from 0 mm to 12 mm, was simulated to identify various control scenarios; however, a constant compressor speed of 300 cycles per second was required to meet the breathing system air requirements. It was concluded that there would be manufacturing and inertia difficulties associated with this type of compressor, leading to the requirement for an alternative ADU to that initially proposed.

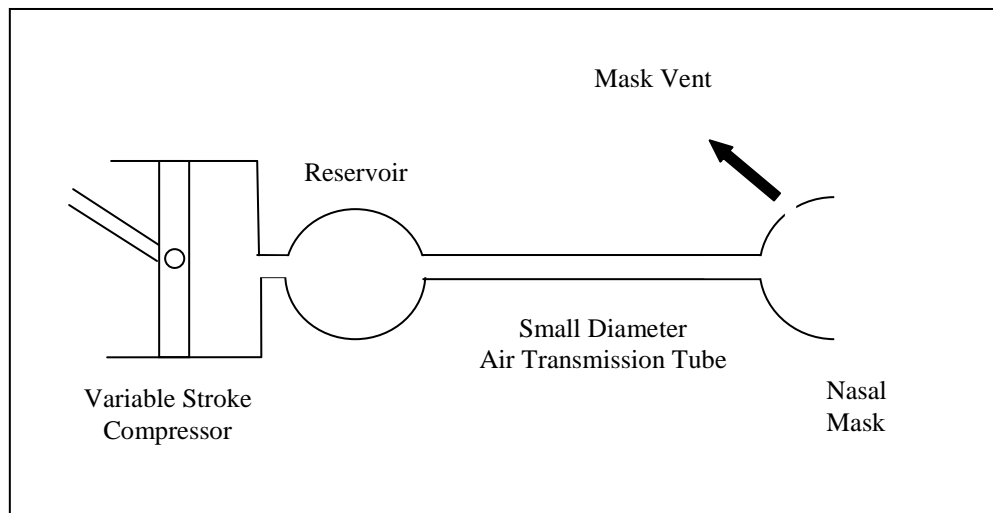


Figure 1.14 Schematic of transient breathing system [27].

1.4 Research Objectives

The objective of this research is to develop a compressor suited to operate within the ADU element of the I-CPAP breathing therapy system. The compressor design performance specifications will be based on a breathing system model simulation, incorporating characteristics of gas inertia, effects of sudden contraction and expansion, fluctuating flow resistances and characterised mask vent behaviour, not previously utilised. System design parameters will be taken from components intended for use within a prototype breathing system. To achieve this goal, the following work is undertaken:

- a) Determination of physical properties and attributes of commercially available reservoir, air transmission tube and nasal mask identified as suited for application within a prototype I-CPAP system.
- b) Development of a breathing system model, based on the proposed prototype, utilising an idealised, zero order, compressor element but incorporating the attributes of varying air flow resistances, gas inertia and compliance of the flexible air transmission tube.
- c) Verification of computer model simulation by comparison with prototype system steady state and dynamic behaviour.

- d) Determination of the air compressor performance specifications required by the prototype breathing system from the results of model simulation.
- e) Synthesis of compressor design and production of a device capable of satisfying the breathing system performance requirements, identified by the model simulation.
- f) Production of compressor performance calibration charts and ADU dynamic behaviour.
- g) Use of model simulation to verify compressor as being capable of meeting breathing system air requirements.
- h) Implementation of the compressor within the ADU element of the prototype I-CPAP system and test the overall system performance.

Chapter 2 System Modelling

2.1 Introduction

To assist in the initial air compressor design, a model of the I-CPAP system is developed with the primary purpose of determining the minimum air requirements of the system. This leads to the identification of air compressor design specifications, used in the compressor design, required by a prototype I-CPAP breathing system.

The proposed breathing system, Figure 2.1, consists of an ADU, controlled by mask pressure, delivering air to a humidification reservoir before passing through an air transmission tube supplying the patient nasal mask. The output signal from the mask pressure transducer (P_m) is compared to a desired value (DV) by the ADU controller and appropriate action is taken to maintain a constant mask air pressure. To simplify the configuration of the prototype system, the humidification reservoir and nasal mask of an existing CPAP breathing device, the Fisher & Paykel HC220 is utilised. As proposed in Chapter 1, the air transmission tube, connecting the reservoir to the mask, will be reduced from 20 mm to 5.5 mm internal diameter for both patient comfort and convenience.

A lumped dynamic breathing system model, Figure 2.1, is developed, based on a prototype I-CPAP system incorporating the physical parameters of a proposed prototype system that accounts for varying air flow resistances, gas inertia, air fluid properties and compliance of the flexible air transmission tube.

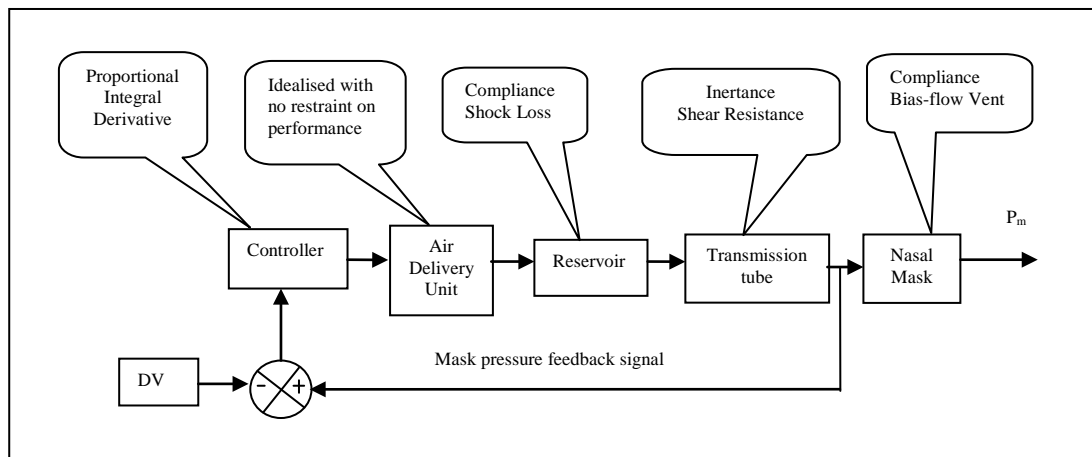


Figure 2.1 Block diagram of I-CPAP system model showing physical parameters considered.

Conservation laws of physics combined with fluid flow equations are used to develop the mathematical representation of the initial simulation [28,29]. Each physical element making up the system is analysed as separate blocks within the model with equations predicting the behaviour of each block being developed.

In this research, the effects of non-linear system characteristics, such as turbulent flow resistance and orifice discharge characteristics, are linearised over the system's normal operation range [29,30]. Checks are made to ensure any deviation between predicted and linearised value, due to the linearisation process, are insignificant. This is done to generate an overall breathing system linear model.

Assumptions are made to characterise the flow process and simplify the initial model. The thermodynamic gas processes are assumed to be isothermal, since changes in pressure are sufficiently low and the system operates at room temperatures. The effect of mass transfer from water contained within the humidification reservoir is also ignored.

In the following sections the derivation of each model block is developed, then assembled to form the completed system model. Since the initial purpose of the model is to predict the air delivery specifications of the ADU element within the breathing system, this block initially considered to be an ideal zero order device, with the output directly proportional to the input signal, with no time delay present. Later, when the compressor is built, the response characteristic of this element can be tested and built into the model to represent the prototype breathing system.

2.2 Model Development

Since, at this stage, neither the type of compressor nor the controller specifications are known for the ADU within the proposed breathing system, modelling will start from the reservoir and proceed through to the transmission tube and finally the nasal mask. Once completed, the model will give the overall air output characteristics required by the ADU.

2.2.1 Reservoir

The primary function of the reservoir is to humidify the air entering the mask, preventing the patient's throat from becoming dry and irritable. Changes in air properties are neglected since it is assumed that the process is isothermal, due to the very low pressure variation experienced. Applying conservation of mass across the reservoir, Figure 2.2, in a period of time dt leads to:

$$\left(\dot{m}_c - \dot{m}_t \right) dt = dm_r \quad (2.1)$$

Where \dot{m}_c is the air mass flow rate entering the reservoir, \dot{m}_t is the out-flowing tube air mass flow rate and dm_r is the change of air mass within the reservoir.

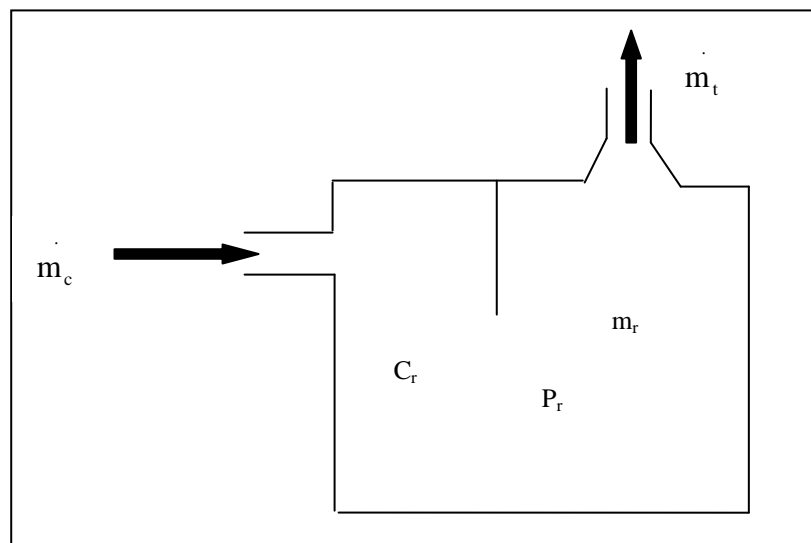


Figure 2.2 Schematic representation of reservoir.

To determine the rate of change of the air mass within the reservoir, one can use the equation of state:

$$P_r V_r = m_r R_a T_r \quad (2.2)$$

Assuming constant temperature and volume results in:

$$\frac{dm_r}{dt} = \frac{V_r}{R_a T_r} \frac{dP_r}{dt} \quad (2.3)$$

Substituting Eq. (2.3) into Eq. (2.1) results in an expression relating the reservoir mass flow and pressure, namely:

$$\dot{m}_c - \dot{m}_t = C_r \frac{dP_r}{dt} \quad (2.4)$$

where $C_r = V_r/R_a T_r$.

The effect of the shock loss due to the reduction in flow area experienced by air passing into the tube from the reservoir is modelled as a scaling factor (k_s) to keep the model simple.

2.2.2 Transmission Tube

Due to the relatively high peak air velocity experienced it is necessary to consider both the air inertia and shear flow resistance occurring within the 5.5mm internal diameter transmission tube. To simplify the tube analysis, both the air and flexible tube wall are combined to determine an equivalent effective bulk modulus; however, due to the relatively low peak pressures involved, the compliance effect, given in Section 2.3, can be neglected without any significant effect on the dynamic behaviour of the model.

The fluctuating patient breathing load experienced by the model, Figure 2.3, ranges from 0.7 g/s outflow to 0.3 g/s inflow, during inhalation and expiration respectively, and is based on an average adult patient breathing at rest.

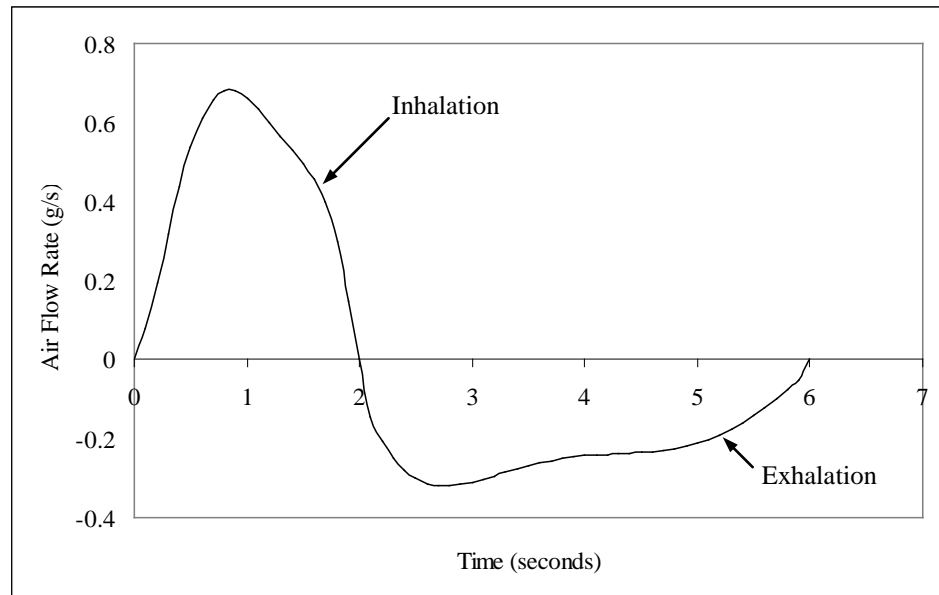


Figure 2.3 Fluctuating patient breathing load.

For the breathing system to achieve a constant mask pressure, the fluctuating breathing load requires the mask air mass inflow rate to range from 1.4 g/s down to 0.7 g/s during patient inhalation and exhalation, respectively. This figure is based on a nasal mask air pressure of 16 cm Wg which produces a continuous mask vent bias flow of 0.7 g/s.

During patient breathing, the air velocity within the transmission tube ranges from 15 m/s up to 45.3 m/s, based on the fluctuating mask air mass inflow rate. The maximum rate of acceleration of the tube airflow is in the order of 30.3 m/s^2 requiring the resulting inertia effect to be considered.

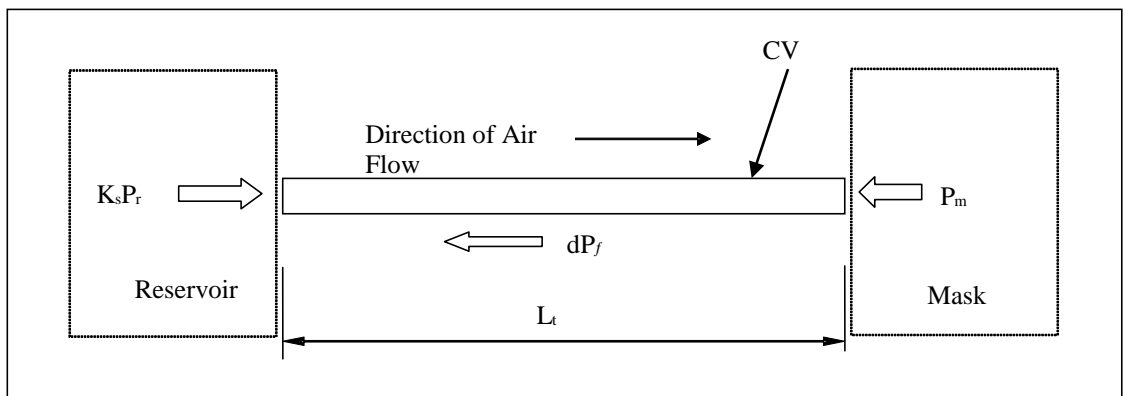


Figure 2.4 Schematic representation of air transmission tube.

Figure 2.4 shows a control volume surrounding the air within the tube, with the main forces being the pressure and friction forces. Applying Newton's second law across the control volume results in:

$$(K_s P_r - P_m) A_t - dP_f A_t = \rho_a A_t L_t \frac{dV_t}{dt} \quad (2.5)$$

where K_s is the reservoir contraction shock loss, P_r reservoir pressure, P_m mask pressure, A_t tube cross sectional area, dP_f air shear resistance force, ρ air density, L_t tube length and V_t air velocity within the tube.

The air flow regime within the tube is predicted as being exclusively turbulent with Reynold's number (R_e) exceeding 2800 for a minimum airflow through the tube of 0.4 g/s. Utilising Miller equation [31] enables an initial air flow friction factor (f_1) to be estimated:

$$f_1 = 0.25 \left[\log \left(\frac{\left(\frac{\varepsilon}{d_t} \right)}{3.7} + \frac{5.74}{R_e^{0.9}} \right) \right]^{-2} \quad (2.6)$$

where ε is the relative surface roughness and d_t the internal diameter of the tube. It is believed that this initial calculation will eliminate the need for an iterative process and enable the final friction factor (f_2) to be calculated by:

$$\frac{1}{f_2^{0.5}} = -2.0 \log \left[\frac{\left(\frac{\varepsilon}{d_t} \right)}{3.7} + \frac{2.51}{R_e f_1^{0.5}} \right] \quad (2.7)$$

The pressure loss due to air-tube wall shear forces (dP_f) can be determined by:

$$dP_f = \rho_a g h_f = \frac{\rho_a f_2 L_t V_t^2}{2d_t} \quad (2.8)$$

The air velocity within the tube may be written as:

$$V_t = m_t / \rho_a A_t \quad (2.9)$$

Substituting this into Eq. (2.8) results in:

$$dp_t = \frac{f_2 L_t m_t^2}{2d_t \rho_a A_t^2} \quad (2.10)$$

It is anticipated that the pressure drop characteristic of the small diameter air transmission tube, due to air-tube wall shear forces, will have the single most significant impact on both the pressure attenuation and dynamic behaviour of the breathing system. To give confidence to the tube air pressure drop calculated by Eq. (2.10), testing on the tube was conducted and the results compared to calculated values. Testing consisted of a pressure regulated air supply connected to a pressure transducer, supplying air to one end of the tube via a hot wire aneometer. The other end of the tube was open to atmosphere, Figure 2.5. The air mass flow rate through the tube was recorded over a range of supply pressures and the results compared to the calculated values. The experimental air pressure drop characteristics compare very well with the calculated values, predicted by Eq. (2.10), Figure 2.6. Tube air flow resistance based on air flow velocity is given in Appendix A1.

As mentioned earlier, the mask air inflow rate from the supply tube varies between 1.4 and 0.6 g/s to achieve a constant nasal mask pressure of 16 cm Wg, requiring a mean operating value of 1 g/s to be used for linearization purposes. Using the slope at this point results in a straight line that is slightly offset to minimise any error over the breathing system operating range. The percentage error present between the predicted linear and non-linear values, over the calculated system air mass flow range, varies from +4% to -11 %.

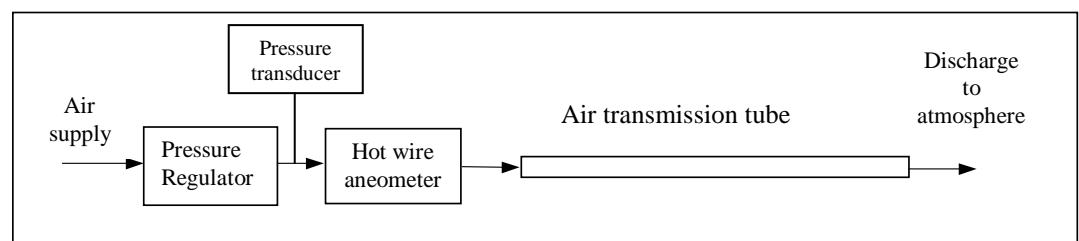


Figure 2.5 Schematic representation of air transmission tube test setup.

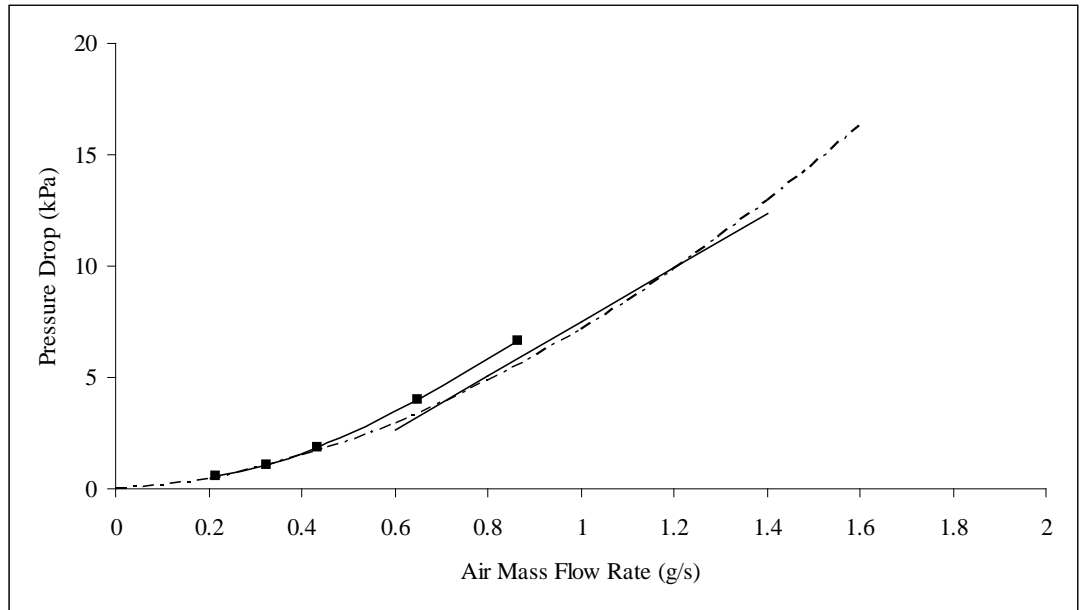


Figure 2.6 PVC tube, 5.5 mm internal diameter, airflow pressure drop; ■—■ measured, - - - - predicted, — linear model.

The linearised tube air flow characteristics are used to express the shear forces (dP_f) in terms of the slope (R) and the intercept (Y) as:

$$dP_f = R_m \dot{m}_t + Y_m \quad (2.11)$$

where the subscript m refers to air mass flow basis for the tube air pressure drop. This pressure drop may also be represented in terms of the pressure difference experienced at either end of the tube, shown previously in Figure 2.4, and written as:

$$dP_f = K_s P_r - P_m \quad (2.12)$$

Combining Eq. (2.11) and Eq. (2.12) allows the air mass flow rate within the tube to be expressed in terms of the linearised resistance and air pressure experienced at either end of the tube, namely:

$$\dot{m}_t = \frac{K_s P_r - P_m - Y_m}{R_m} \quad (2.13)$$

Combining Eq. (2.13) with Eq. (2.4) leads to:

$$\dot{m}_c - \frac{(K_s P_r - P_m - Y_m)}{R_m} = C_r \frac{dP_r}{dt} \quad (2.14)$$

Rearranging Eq. (2.14) yields the expression used to model the breathing system reservoir pressure (P_r):

$$\frac{P_r}{\dot{m}_c + \frac{P_m}{R_m} + \frac{Y_m}{R_m}} = \frac{\frac{R_m}{K_s}}{\frac{R_m}{K_s}(C_r D + 1)} \quad (2.15)$$

where $D = \frac{d}{dt}$.

Combining Eqs. (2.5) and (2.12) leads to:

$$K_s P_r - P_m - (R_v + Y_v) = \rho L_t \frac{dV_t}{dt} \quad (2.16)$$

Rearranging Eq. (2.16) yields an expression for tube air velocity (V_t) to be used in the breathing system model.

$$\frac{V_t}{(K_s P_r - P_m - Y_v)} = \frac{\frac{1}{R_v}}{\frac{\rho L_t}{R_v} D + 1} \quad (2.17)$$

2.2.3 Mask

Air is supplied to the patient via a nasal mask that is continually purged through 8 small vents, ensuring that fresh air is always available to breathe. As with the reservoir, changes in air properties are neglected since it is assumed that the process is isothermal due to very low pressure variation occurring. With reference to Figure 2.7, applying the mass continuity equation across the mask in a period of time dt leads to:

$$\left(\dot{m}_t + \dot{m}_p - \dot{m}_b \right) dt = dm_m \quad (2.18)$$

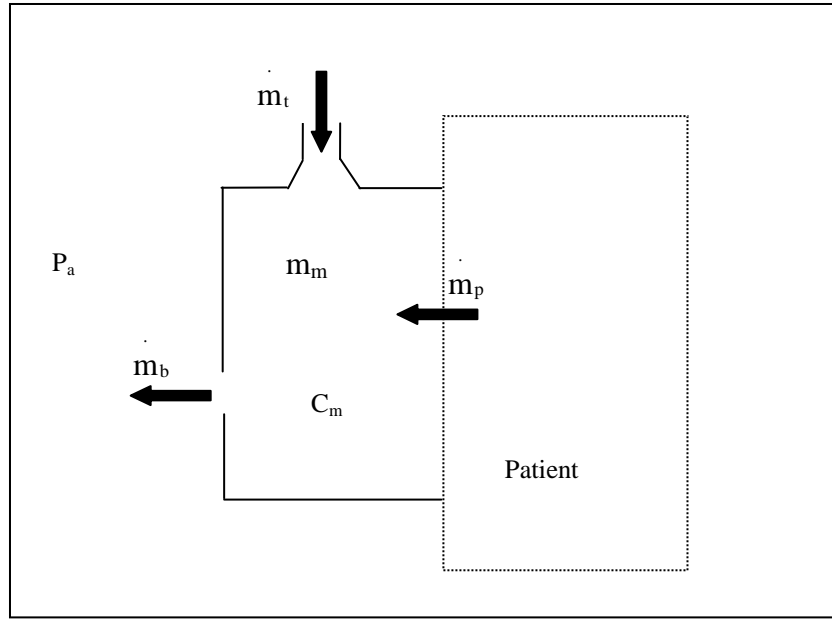


Figure 2.7 Schematic representation of nasal mask.

where m_t and m_b is the air mass flow rate entering from the tube and exiting from the mask vents and m_p and m_m represent the fluctuating patient breathing airflow rate and the mass of air contained within mask, respectively.

Using the equation of state to determine the rate of change of air mass contained within the mask results in:

$$P_m V_m = m_m R_a T_m \quad (2.19)$$

Assuming constant temperature and volume results in:

$$\frac{dm_m}{dt} = \frac{V_m}{R_a T_m} \frac{dP_m}{dt} \quad (2.20)$$

Substituting Eq. (2.20) into Eq. (2.18) results in:

$$m_t - m_b + m_p = C_m \frac{dP_m}{dt} \quad (2.21)$$

where mask capacitance $C_m = V_m/R_a T_m$.

Accurate determination of the nasal mask vent flow discharge coefficient (C_d) is difficult since the 8 vent holes are physically characterised as being a combination

of a sharp edged orifice and a sudden expansion into open space. The prediction of the airflow behaviour through the vent is based on pressure differential experienced between mask pressure (P_m) and atmospheric pressure (P_a) and is based on the governing equations for flow through an orifice plate [32], namely:

$$P_m - P_a = \frac{\rho_a}{2C_d^2 A_b^2} Q_b^2 \quad (2.22)$$

Where ρ_a is the density of the air contained within the mask, A_b the minimum area of the bias vent hole, C_d the discharge coefficient and Q_b the vent volume flow rate. The vent volume flow rate (Q_b) may be expressed as:

$$Q_b = \frac{\dot{m}_b}{\rho_a n} \quad (2.23)$$

where n is the number of holes venting mask air. Substituting Eq. (2.23) into Eq. (2.22) results in:

$$P_m - P_a = \frac{\dot{m}_b^2}{2C_d^2 A_b^2 \rho_a n^2} \quad (2.24)$$

Examination of the bias flow holes in the nasal mask reveals them to be of tapering diameter and short length. A loss coefficient C_d of 0.8 is assumed, which is between the coefficient for a sudden expansion, $C_d = 1$, and a sharp edged hole, $C_d = 0.6$. Testing of the mask bias airflow was conducted to give confidence in the prediction of mask vent behaviour, made by Eq. (2.24), and the two results compared. Mask vent flow testing, Figure 2.8, consists of a pressure regulated air supply connected to the mask via a hot wire anemometer. Mask air pressure was sensed by pressure transducer, connected to the air supply, and the open end of the mask, normally containing the patient's nose, was blanked off with plastic sheet. The air mass flow entering the mask was recorded over a range of supply pressures and the results compared to the calculated values. The experimental mask bias flow compares very well with the calculated value, predicted by Eq. (2.24), over the normal mask operating pressure range of 6 – 20 cm Wg, Figure 2.9.

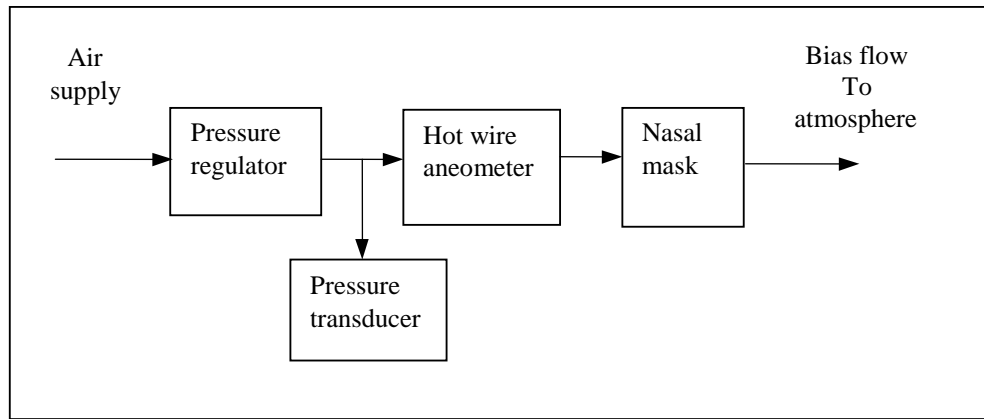


Figure 2.8 Schematic representation of nasal mask vent flow test.

Obviously the mask vent relationship is nonlinear so to linearise this behaviour, a reference point of 10 cm Wg is considered which is between the normal operating pressure range of 6 – 20 cm Wg [9], producing an error of –6 to +5%.

The mask vent bias flow can now be represented by:

$$P_a - P_m = R_b m_b + Y_b \quad (2.25)$$

where R_b is the gradient of the linearised flow characteristic and Y_b represents the y co-ordinate.

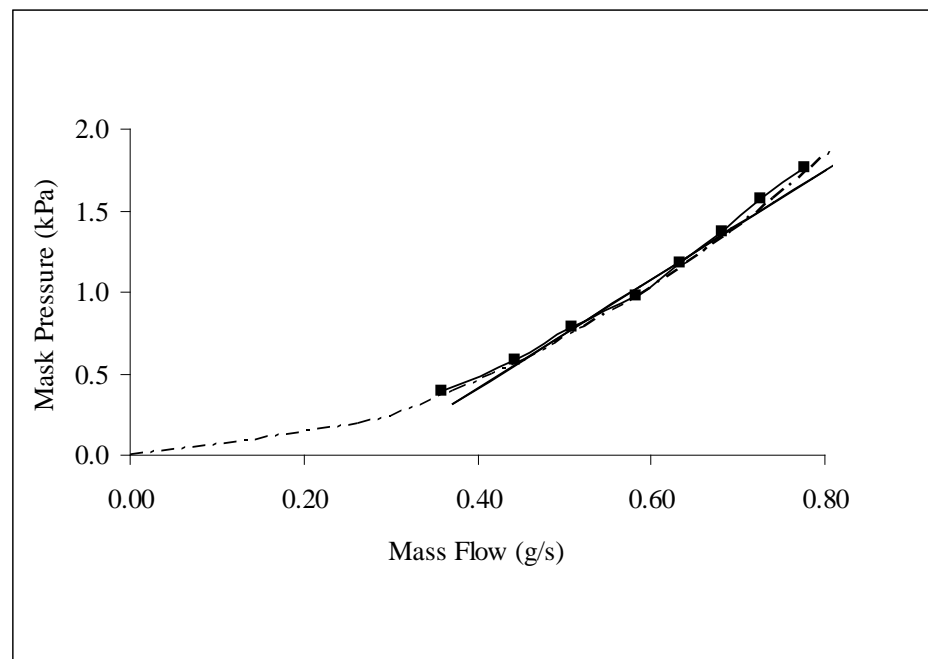


Figure 2.9 Comparison of predicted and measured mask vent flow characteristics; ■—■ measured, - - - - predicted, — linear model.

Rearranging Eq. (2.25) yields:

$$\dot{m}_b = \frac{P_m - P_a - Y_b}{R_b} \quad (2.26)$$

Substituting Eq. (2.26) into Eq. (2.21) results in an expression that enables mask pressure to be expressed in terms of supply tube and patient breathing air mass flow rates:

$$\dot{m}_t - \left(\frac{P_m + P_a + Y_b}{R_b} \right) + \dot{m}_p = C_m D P_m \quad (2.27)$$

where mask capacitance $C_m = V_m/R_a T_m$.

Rearranging Eq. (2.27) yields the expression used to model the breathing system nasal mask pressure:

$$\frac{P_m}{\dot{m}_t + \frac{P_a}{R_b} + \dot{m}_p + \frac{Y_b}{R_b}} = \frac{R_b}{R_b C_m D + 1} \quad (2.28)$$

2.3 Justification of Neglecting Terms

In the previous sections, the air and tube compliance were neglected along with changes in tube air density, however, in this section justification is given as to why this was done.

2.3.1 Compliance Effects

The significance of the combined effect of air and tube wall compliance within the system needs to be quantified since inclusion of this effect will result in significant complications within the lumped model due to the progressive pressure reduction experienced along the length of the tube. Variation in air pressure causes corresponding variations in air density, however, it is anticipated that this effect will be insignificant due to the relatively low pressures involved.

Preliminary calculations, based on steady state flow conditions, indicate a maximum air gauge pressure difference of 12.9 kPa is experienced across the ends of the transmission tube. This figure is derived from the maximum transmission tube air mass flow requirements, under steady state conditions, requiring a reservoir gauge pressure of 14.5 kPa to supply the patient mask operating at a constant pressure of 16 cm Wg.

Utilising the characteristic gas relationship allows the air density within the tube to be determined,

$$\rho = \frac{P_t}{R_a T_a} \quad (2.29)$$

where P_t is the absolute air pressure, R_a the gas constant and T_a the absolute temperature. Based on the calculated steady state maximum pressures experienced at either end of the tube, Eq. (2.29) yields a maximum air density (ρ_1) of 1.376 kg/m³ and minimum air density (ρ_2) of 1.222 kg/m³ for the air contained within the high and the lower pressure ends of the tube respectively.

By calculating an average air density ($\rho_{a,ave}$) of 1.299 kg/m³ it is now possible to determine a combined effective bulk modulus of both the air and the PVC plastic tube by utilising the relationship between the speed of sound in a rigid tube and the speed of sound in a flexible tube [33].

For the former:

$$C = \sqrt{\frac{\beta_a}{\rho_a}} \quad (2.30)$$

and for the latter:

$$C = \sqrt{\frac{\beta_a}{\rho_a}} \sqrt{\frac{1}{1 + d_t \frac{\beta_a}{t\beta_t}}} \quad (2.31)$$

where C is the speed of sound, β_a the bulk modulus of the air, ρ_a the air density, β_t the tube bulk modulus, d_t the tube diameter and t the tube wall thickness.

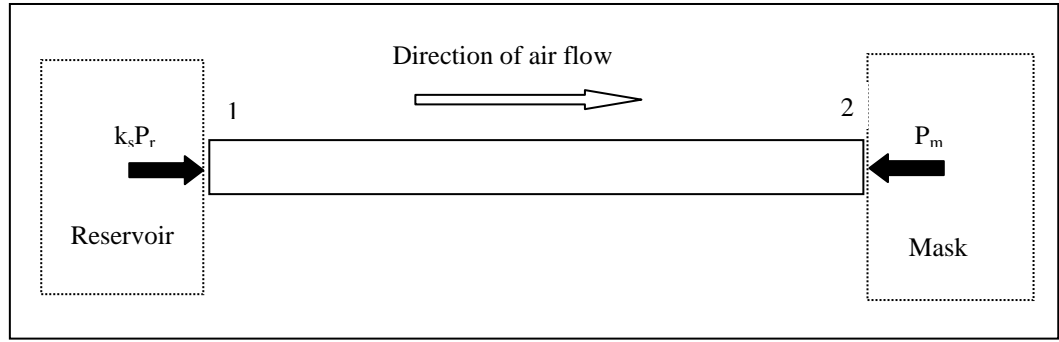


Figure 2.10 Schematic representation of air transmission tube.

Combining Eq. (2.30) and Eq. (2.31) results in:

$$\sqrt{\frac{\beta_{a,eff}}{\rho_{a,ave}}} = \sqrt{\frac{\beta_a}{\rho_{a,ave}}} \sqrt{\frac{1}{1 + d_t \frac{\beta_a}{t\beta_t}}} \quad (2.32)$$

where the combined air and tube compliance is expressed as an effective bulk modulus, $\beta_{a,eff}$.

Considering the bulk modulus for the PVC tube (β_t), Appendix A2, and the bulk modulus for air (β_a) as being 7.6 MPa, [34], and 145 kPa, [31], respectively, results in an effective bulk modulus ($\beta_{a,eff}$) of 133.34 kPa.

The influence of the combined air and flexible tube compliance effect is now determined by considering the percentage change in air volume within the tube. Dividing the tube into 10 lumps, Figure 2.11, accounts for the pressure drop experienced along the tube length, this is achieved using:

$$dP = \beta_{eff,air} \frac{dV}{V} \quad (2.33)$$

where dV is the variation in the lumped tube volume V based on an average pressure for each lump under consideration.

By utilising the air shear resistance pressure drop, expressed as a function of air velocity within the tube, calculated using Eq. (2.10), the percentage variation in volume of each lump is then determined, Figure 2.12.

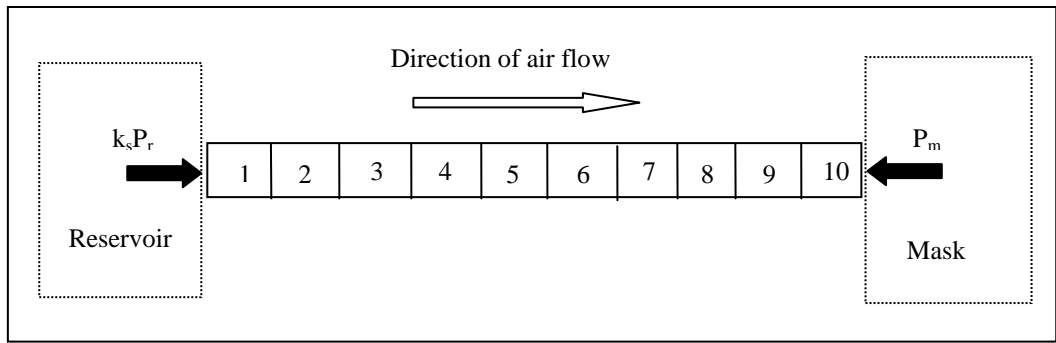


Figure 2.11 Tube divided into 10 lumps.

Based on steady state maximum air flow conditions occurring within the tube, the total variation in air volume along the tube length, due the combined compliance of both the air and flexible PVC tube, is 7.9%. If this variation in volume was approximated to corresponding changes in air velocity and acceleration within each lump then the combined compliance effect of the tube and air would have an insignificant affect in the dynamic model behaviour. Therefore the combined compliance effect of the flexible tube and air has been neglected within the model.

The significance of changes in air density occurring within the tube, due to the high flow velocities encountered, also needs to be quantified. Calculations, based on a the maximum tube air mass flow rate of 1.4 g/s, show a maximum air flow velocity of 45.3 m/s occurs within the tube.

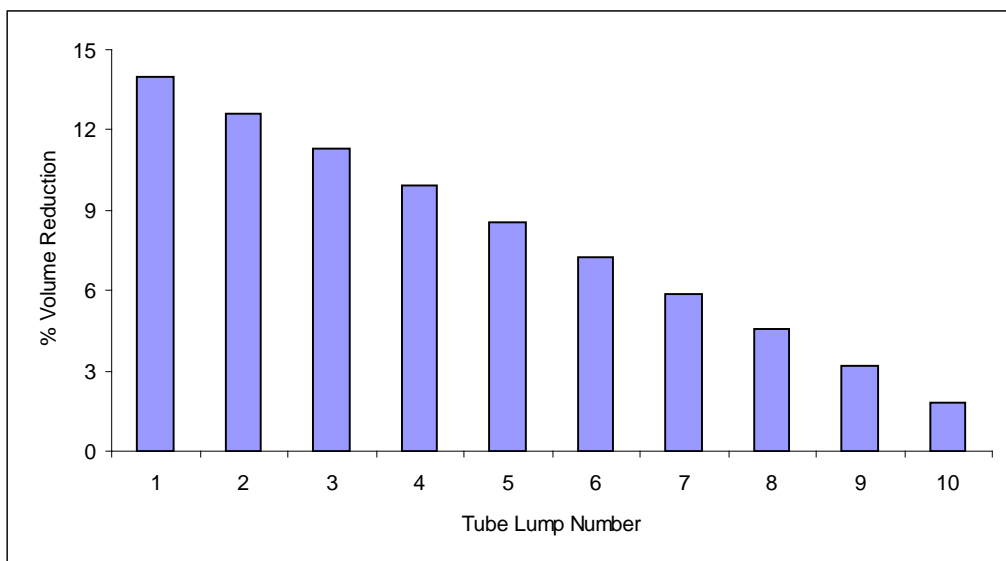


Figure 2.12 Percentage lumped air volume reduction within tube.

The significance of air compressibility, due to flow velocity, can be determined by considering the magnitude of air flow mach number (M) occurring within the tube. This is achieved by first considering:

$$\gamma = \frac{C_p}{C_v} \quad (2.34)$$

where γ is the ratio of specific heats given by the air specific heat capacities for constant pressure (C_p) and constant volume (C_v) processes respectively.

The mach number can now be determined from:

$$M = \frac{V_a}{\sqrt{\gamma R_a T_a}} \quad (2.35)$$

where R_a is the characteristic gas constant for air and T_a the absolute air temperature.

The effects of compressibility on air density must be considered for air flow mach numbers above 0.3 [35], however, calculation of the maximum air flow mach number occurring within the tube, using Eq. (2.35), yields a maximum value of 0.17, indicating this effect is insignificant. Therefore, any change in air density due to the high tube air flow velocities encountered has been neglected in the model.

2.4 Closure

The three main breathing I-CPAP system elements, consisting of the reservoir, transmission tube and nasal mask, derived in earlier sections are now brought together to represent the complete breathing system model.

A breathing model block diagram, Figure 2.13, shows the transfer function reflecting the physical action controlling that element. In Chapter 3, a computer model simulation is used to predict the air output specifications of the ADU required by the prototype breathing system. Later, when the ADU element is built, the dynamic response

characteristic of this element will be tested and built into the model, completing the breathing system model simulation.

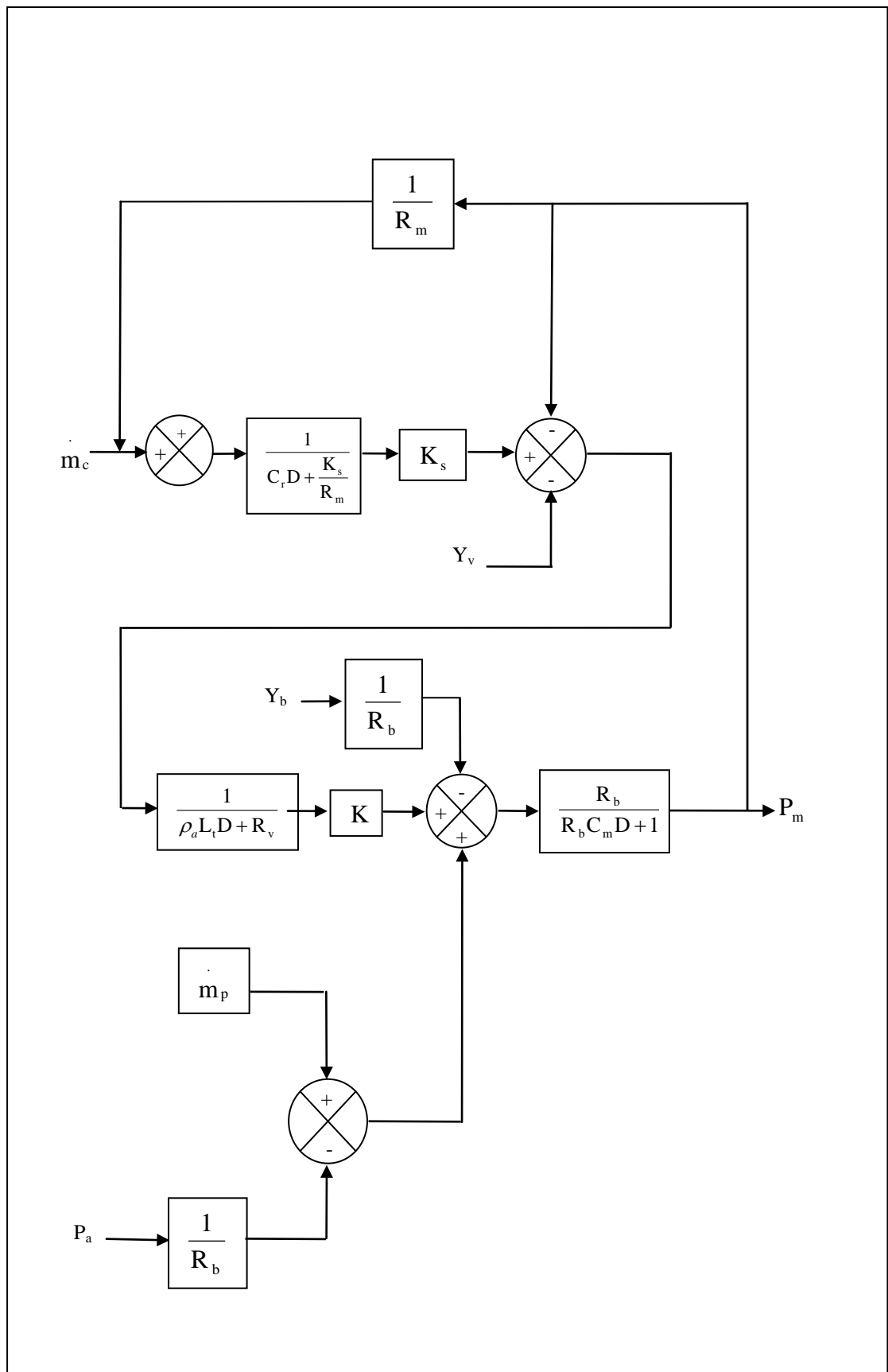


Figure 2.13 Block diagram of breathing system model.

Chapter 3 Model Simulation

3.1 Introduction

A computer simulation model of the proposed breathing system is developed, using SIMULINK® within MATLAB® environment, utilising an idealised ADU. The governing equations used within the model simulation are detailed through the use of block diagram algebra obtained from the SIMULINK program.

Confirmation that the model simulation can accurately predict the breathing system dynamic behaviour is required since it will subsequently be used to determine the breathing system ADU performance specifications. This will be achieved by comparing the model and the prototype system steady state and dynamic testing mask pressure responses.

3.2 SIMULINK Model

Equations governing the dynamic behaviour of the breathing system model, developed in Chapter 2, are now used to produce a SIMULINK computer breathing model within MATLAB environment.

The complete model, Figure 3.1, shows the breathing system is being divided into three main sections, the ADU, reservoir and transmission tube and the nasal mask. Closed loop pressure feedback control of the ADU is utilised to control nasal mask pressure fluctuations during patient breathing. Model simulation pressure and mass flow rates have been sensed to enable comparisons to be made with the prototype breathing system.

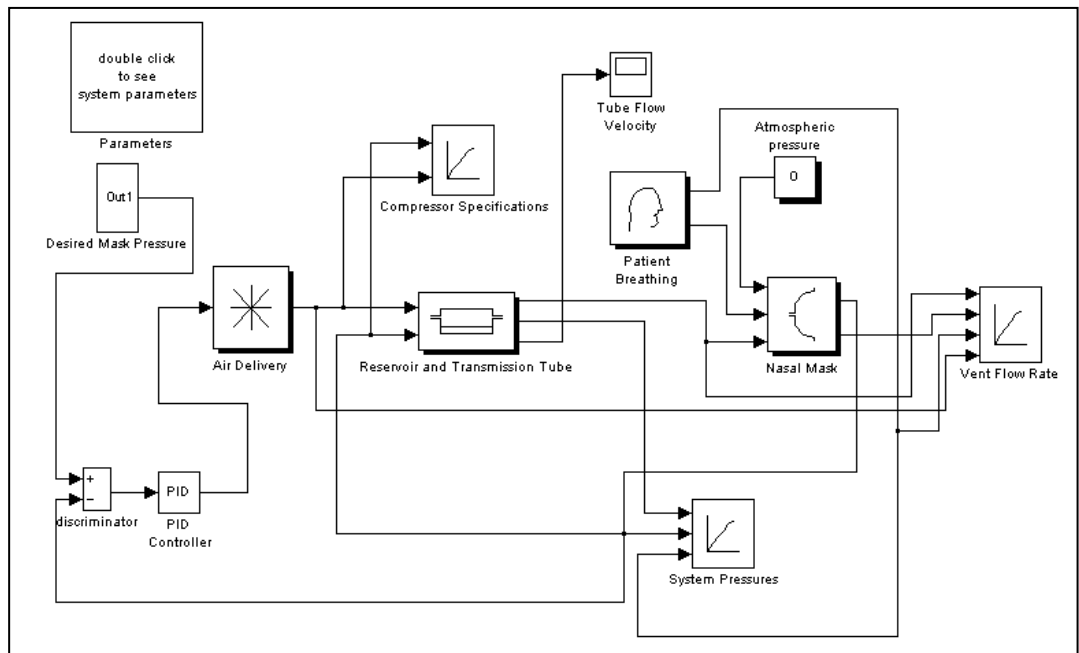


Figure 3.1 SIMULINK I-CPAP breathing system model.

3.2.1 Air Delivery Unit

The idealised zero-order ADU model simulation element, Figure 3.2, gives an output value directly proportional to the input signal with no adverse operational characteristics. Later, once the complete prototype system has been built, dynamic testing of the ADU, Chapter 5, will enable its operational characteristics to be added, completing the model simulation.

3.2.2 Reservoir and Transmission Tube

The reservoir and transmission tube model elements, Figure 3.3, are combined into one model simulation block to simplify construction. Provision is made to input the prototype breathing system physical parameters into the combined reservoir-transmission tube model simulation element. To facilitate the assembly of the prototype breathing system, the humidification reservoir is sourced from a commercially available CPAP unit [8].

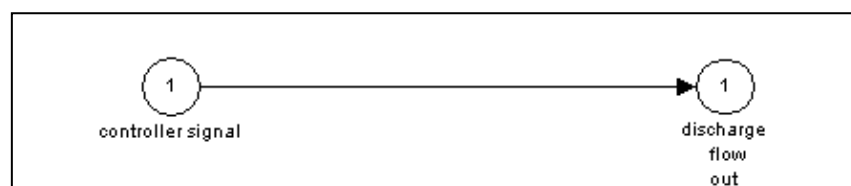


Figure 3.2 SIMULINK model of idealised air delivery unit.

3.2.4 Patient

The patient breathing load, Figure 2.3, is input into the model simulation as an independent variable, read from a text file *breath.txt*, representing the relaxed breathing cycle typical of a sleeping adult patient, and is supplied by Fisher & Paykel Healthcare. Patient breathing air mass flow-rate (g/s) is shown as a function of time; inhalation and exhalation being given as a positive and negative quantity respectively.

3.3 Dynamic Testing Model

Within this section, the reservoir, transmission tube and nasal mask elements of the SIMULINK model simulation are dynamically tested by comparing the system mask pressure response prior to and after a disturbance occurs within the system. Previous steady state testing, Chapter 2, of the two sources of pressure drop within the breathing system, the small diameter air transmission tube and nasal mask vent, has shown the predicted steady state behaviour of these two breathing system elements to closely follow that of the real system components. There is also the need, however, to establish confidence in the model simulation accurately predicting the behaviour of the prototype breathing system.

3.3.1 Test Setup

The dynamic behaviour of the prototype system is determined by introducing an air flow disturbance into the reservoir, during operation of the system to produce a corresponding dynamic response in mask air pressure.

The flow disturbance for the breathing system is achieved by utilising two air pressure regulators, connected in parallel, to supply air to the system reservoir, Figure 3.5. Each pressure regulator is pre-set to produce a steady state mask pressure within the system of 8 cm Wg and 18 cm Wg for the low and high pressure settings respectively.

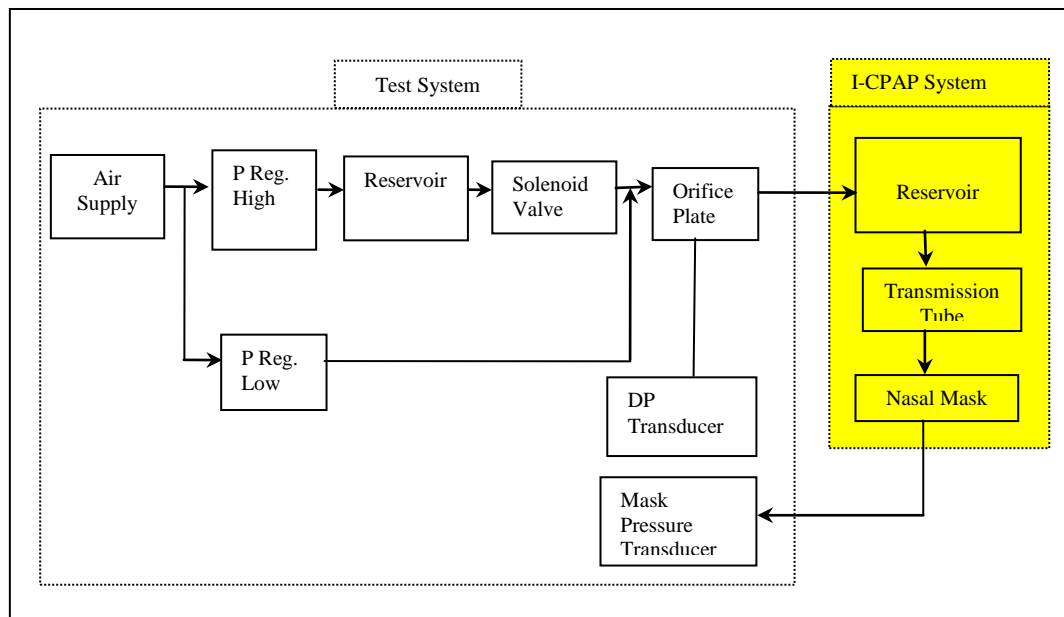


Figure 3.5 Schematic representation of prototype I-CPAP system test setup.

Initial testing of the breathing system showed that it responded rapidly to any dynamic change, either in load or air supply, and that any transducers used in measuring this system needed to respond within 10 ms if meaningful dynamic information is to be recorded. Thermal inertia experienced by the hot wire measurement system within the TSI 4040 air mass flow meter, initially considered for dynamic measurement of air entering the system, resulted in a measurement time delay of approximately 20 ms. To overcome this problem, the incoming air mass flow was measured using an orifice plate and differential pressure (DP) transducer.

Both low and high pressure regulator air flows pass through the orifice plate, enabling air mass flow onto the prototype system reservoir to be measured and recorded. The low pressure regulator was constantly supplying the nasal mask whilst the high pressure regulator was isolated from the system by a solenoid valve. Actuating the solenoid valve permitted the higher pressure supply air to enter the system reservoir whilst the low pressure regulator, sensing the increase in downstream pressure, shut off its air supply.

The high pressure regulator is connected to a 6 litre air reservoir which provided additional high pressure air capacitance in order to minimise the fluctuation in supply air pressure when the solenoid valve was opened.

Table 3.1 Test equipment details.

Equipment	Manufacturer	Model	Serial Number
Precision Pressure Regulators	Unmarked	Unmarked	Unmarked
Solenoid Valve	Burkert	Unmarked	136679A
DP Transducer	Motorola	MPXV4006G	Unmarked
Reservoir	Wolfendale Eng. LPG Bottle	6 Litre	SNP 001314
Storage Oscilloscope	TDS	3034	B013155

The disturbing input air mass flow rate measured by means of the orifice plate and DP transducer was recorded to be later used as an input air disturbance within the model. The system's mask air pressure response to the incoming air disturbance was recorded by a pressure transducer. Table 3.1 details the equipment used in the test.

3.3.2 Air Mass Flow Calibration

Calibration of the orifice plate and DP transducer measuring the incoming air was necessary prior to any dynamic testing being conducted. This was achieved by using the existing test set up with the addition of a calibrated hot wire anemometer connected in series with the orifice plate. Steady state calibration of the airflow orifice entailed incrementing the air supply mass flow rate in steps whilst simultaneously recording both the measured output from the calibrated hot wire anemometer and the output voltage from the DP transducer.

As expected, the output signal from the DP transducer, Figure 3.6, had a distinct non-linear behaviour, characteristic of airflow through an orifice plate. Initial assessment of the calibration curve showed a distinct straightening above an air mass flow rate of 1 g/s, possibly due to the geometry of the orifice plate. Despite this effect, it was still possible to produce a calibration equation for the orifice plate and DP transducer, enabling accurate flow measurements to be determined. Calibration of the DP transducer and orifice plate was made possible by the fact that air mass flow within the prototype breathing system is predominantly around the 0.5 g/s to 0.8 g/s range, Figure 2.9, under steady state conditions.

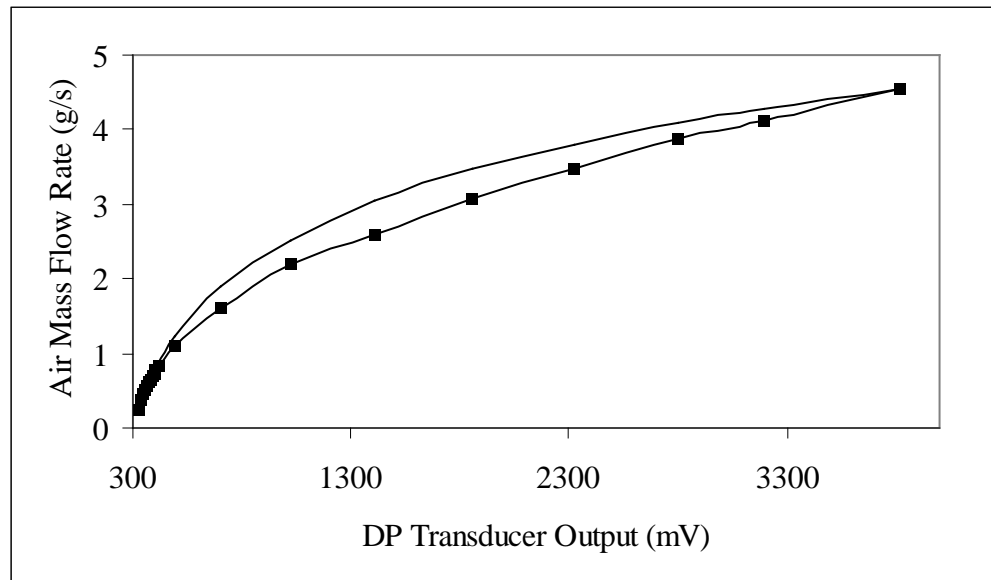


Figure 3.6 Orifice plate calibration air mass flow curves; — calibration prediction, ■— DP transducer output.

There is clearly a deviation, shown in Figure 3.6, between the DP transducer output calibration and measured air mass flow rate curves over the midrange output, however, this calibration error is not considered significant to the overall calibration of the DP transducer or the breathing system dynamic test results. This is justified by the air mass flow rate rising to 3.7 g/s for approximately 30 ms, during the transition from low to high pressure air supply in subsequent testing of the prototype system. Any deviation between actual and measured air flow, due to the transducer mid range calibration error, would simply have resulted in a minor variation in the gradient of the measured transient airflow curve. The system steady state and maximum air inflow values would however have been accurately measured over the predominant flow range, as shown by Figure 3.7.

3.3.3 Pressure Transducer Calibration.

The pressure transducer sensing mask pressure was capable of responding within 8 ms and considered sufficiently fast for testing the dynamic response of the prototype system.

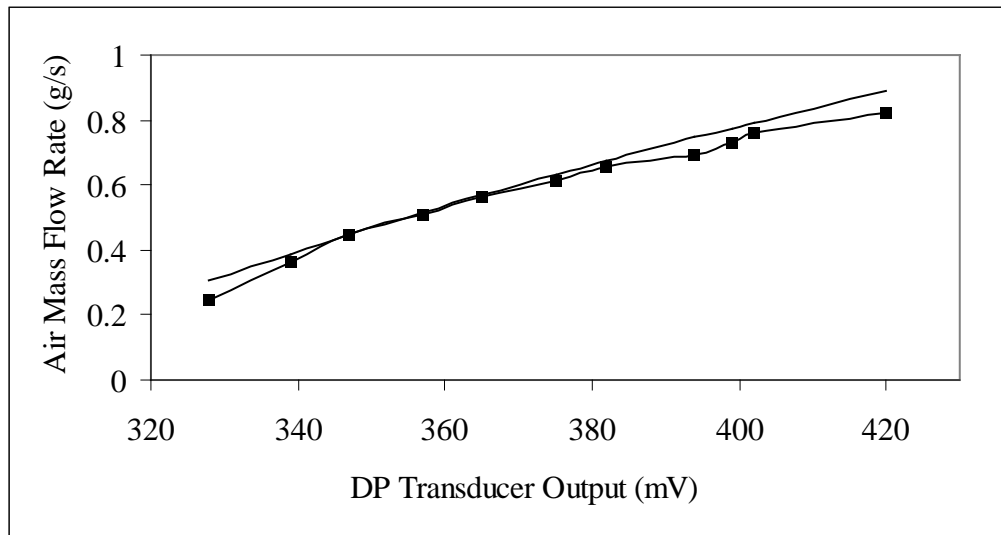


Figure 3.7 Orifice plate calibration prediction over normal system air mass flow range. — calibration prediction, —■— measured DP transducer.

Since this device has an in-built calibration correction circuit combined with the factory calibration, it is not necessary to correct for any non-linear characteristics. Calibration of this transducer simply involved conversion of the voltage output signal to air pressure in cm Wg.

The open-end of the nasal mask, normally containing the patient's nose and face, was blanked off with a thin plastic diaphragm. The pressure transducer sensing mask pressure was connected to the mask volume by a short length of small diameter plastic tube.

3.3.4 System Dynamic Testing

Initially the system was operating at a steady state with air being supplied by the low-pressure regulator producing a constant low mask pressure. The high pressure air supply solenoid was then actuated, allowing high pressure air to enter the system reservoir, producing a mask pressure response that settled to a new steady state value. During this time both the air mass flow disturbance entering the system reservoir and corresponding response in mask pressure were recorded by the storage oscilloscope.

Initial dynamic testing using the DP transducer and orifice plate air mass flow measurement system indicated that a measurement delay of approximately 8 ms

was occurring. This effect is likely due to air compliance within the pressure sensor tubes leading from the orifice plate, however, this time delay is not considered significant to warrant concern.

Despite the use of the 6 litre reservoir of high pressure air within the test circuit, it was not physically possible to produce a step change in the system input air mass flow due to the compliance characteristic of the air volume contained within both the test apparatus hose and the breathing system reservoir. Complicating this problem was the second order dynamic characteristic of both precision pressure regulators used to supply air to the system, responding to the changing air volume demand, causing additional air flow and pressure disturbances. Despite it not being possible to produce a step input, it was possible to measure the system response to an input air flow disturbance.

Upon completion of the dynamic test, both pressure and air mass flow transducer signals contained within the storage oscilloscope were displayed and stored to floppy disc. The files containing both the time and transducer voltage values were transferred to Microsoft Excel® where signals were converted into measured parameters through application of the appropriate calibration equation.

To enable the measured system reservoir air mass inflow rate to be input into the SIMULINK model, both the time and transducer air mass flow recorded on spreadsheets were transferred to Microsoft Notepad®, permitting the data to be read by the SIMULINK model.

3.3.5 Model Simulation

To ensure accuracy of the breathing model simulation, the physical properties of the prototype breathing system were carefully determined through measurement of the apparatus used or reference to appropriate property tables.

The model simulation variable parameters, Table 3.2, are configured to match the prototype system elements tested.

Table 3.2 Computer Simulation Parameters.

Reservoir	Capacitance	0.005604	g/kPa
	Shock Factor into Tube	0.9	
Tube	Internal Diameter	5.5	mm
	Length	1.8	m
	Tube Velocity Pressure Drop Gradient	0.3752	kPa/ms ⁻¹
	Tube Velocity Pressure Drop Y Coordinate	-4.6587	kPa
	Tube mass Flow Pressure Drop Gradient	12.147	kPa/ms ⁻¹
	Tube mass Flow Pressure Drop Y Coordinate	-4.6587	kPa
Air Properties	Average Air Density	1.334	Kg/m ³
	Effective Air Bulk Modulus	136330	Pa
Nasal Mask	Capacitance	0.0011768	g/kPa
	Bias Mass Airflow Pressure Drop Gradient	3.3483	kPa/m/s
	Bias Mass Airflow Y Coordinate	-0.981	kPa

Reservoir capacitance is determined for being void of water, the worst possible condition, and a shock factor of 0.9 is estimated to account for the sudden change in flow area encountered when the air discharges from the reservoir into the small, 5.5 mm internal diameter, PVC air transmission tube, 1.8 metres long, used to transmit air from the reservoir to the nasal mask. The flow resistance experienced by the air within the tube is expressed in a linear format in terms of both air velocity and mass flow. Mask capacitance took into account the plastic plate used to blank off the open end normally covered by the patient's upper face and nose. No change was required for the mask vent flow since the input air mass flow rates are pre-set to produce mask pressures within the normal operating range of 6 cm to 20 cm Wg.

Air density throughout the breathing system is assumed to be constant and of an average value due to the relatively small variation in air pressure experienced. The effective air bulk modulus, defined in Chapter 2, is used to account for the elastic behaviour of both the compliant tube and air compression effect. The mask vent airflow resistance, defined in Chapter 2, is expressed in a linear format in terms of air mass flow rate.

Both the measured signal disturbance and resultant mask air pressure fluctuation, input into the model, are delayed one second after model initiation to ensure that the simulation was stable prior to the measured disturbance being input into the system. This ensured any transient behaviour in the model simulation, due to the initial starting and filling conditions, did not coincide with the time period where dynamic testing occurred.

3.3.6 Results

Operation of the model with the airflow disturbance being read from data obtained during testing of the prototype system resulted in a combined plot of model simulation and prototype system mask pressure dynamic response, Figure 3.8, to the same dynamic input air disturbance. Both the steady state values and dynamic response behaviour of the model compare very favourably with that of the actual breathing system tested.

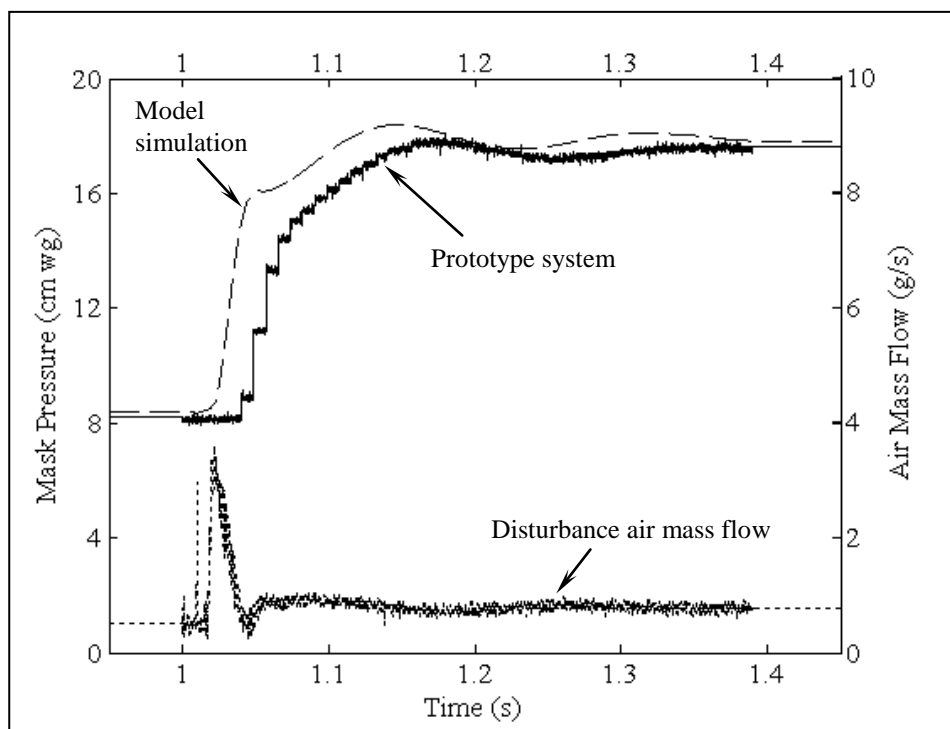


Figure 3.8 System and model simulation dynamic test response.

The measured system mask pressure response is slower than the model by about 20 ms, this time delay has most likely two causes:

1. No consideration was given within the model simulation to the additional capacitance effect of the flow measuring equipment, installed in series prior to the reservoir of the prototype system.
2. The response time delay of 8 ms, mentioned previously in Section 3.3.2, occurring within the nasal mask pressure transducer.

The mask pressure transducer took samples in increments of 8 ms which characterises the recorded mask pressure, Figure 3.8, with step increments in pressure values measured at each time interval. The mask pressure also responds very quickly, taking approximately 150 ms to stabilise to a new steady state value. The response in mask pressure, between the prototype breathing system tested and the model simulation, shows to be nearly identical for the same dynamic change in input air mass flow rate. The steady state mask pressures on both sides of the system disturbance also coincide. A signal interference spike in the input air mass flow is shown, Figure 3.9, at the 1.01 second interval and is believed to be due to electromagnetic interference from the high pressure supply solenoid air valve and does not represent measured air mass flow.

3.3.7 Conclusions

Dynamic testing of the breathing system model simulation shows it to closely mimic the dynamic behaviour of the prototype system, despite both minor calibration and measurement time delay errors being present within the measuring systems. There is also an excellent correlation in steady state mask pressure between the simulation and prototype test data. This result verifies the model simulation as being able to predict the air output specifications of the prototype system ADU.

3.4. Air Delivery Unit Specifications

Within this section model simulation is now used to determine the prototype ADU output air pressure and mass flow specifications. This is achieved by operating the model whilst measurements of ADU air mass flow and pressure are recorded.

3.4.1 Controller

Prior to operating the model it is necessary to create a model ADU controller, acting on mask pressure feedback signal, Figure 3.9.

3.4.2 Model Configuration

As mentioned earlier in Section 3.2.1, it is necessary to assume at this stage that the ADU element within the model simulation is operating as an idealised, zero order element, previously shown in Figure 3.2, since the dynamic characteristics of this model element are currently unknown. All other system parameters, defined earlier for the reservoir and transmission tube, Table 3.2, are utilised within the model simulation.

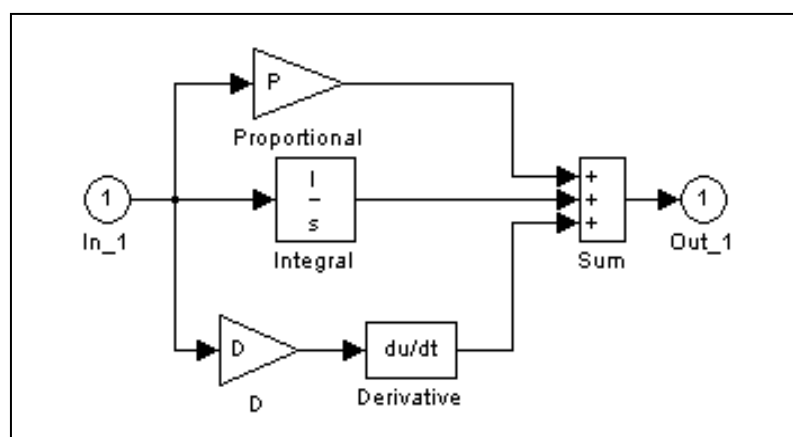


Figure 3.9 Model simulation controller modes.

3.4.3 Results

Model simulation has predicted the air delivery requirements of the prototype breathing system ADU necessary to maintaining a stable mask pressure of 18 cm Wg to within a tolerance of ± 0.5 cm Wg during patient breathing, Figure 3.10. Both the model simulation air pressure and delivery mass flow rates are shown along with the patient breathing load and nasal mask pressure. The ADU delivery gauge pressure fluctuates between 35-170 cm Wg (3.5kPa-17 kPa) with the mass flow ranging from 0.5-1.45 g/s (25 l/s to 72.5 l/s) respectively.

By considering the reservoir air pressure and mass flow rates over the 2 to 8 second time period, representing one complete patient breathing cycle, at one second intervals, it is then possible to establish the breathing system air supply pressure and mass flow requirements. These are summarised in Table 3.3.

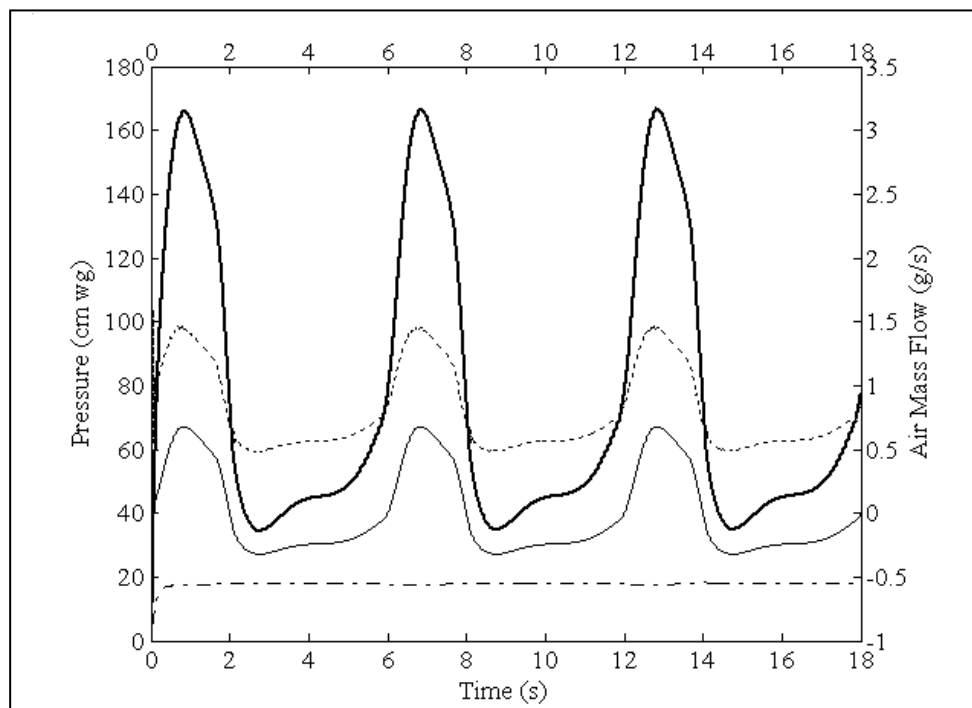


Figure 3.10 Model simulation air pressure and flow results; mask pressure, — patient breathing, — ADU delivery pressure, ---- ADU delivery mass flow.

Table 3.3 Model simulation ADU delivery pressure and mass flow specifications over patient breathing cycle.

Time Interval (s)	Pressure (cm wg)	Mass Flow (g/s)
2	70	0.75
3	35	0.55
4	42	0.60
5	45	0.65
6	85	0.95
7	170	1.45
8	70	0.75

It must be remembered, however, that the patient breathing load utilised for the model simulation is typical for an adult person at rest and that no consideration is given to greater patient breathing demands or rapid changes in breathing pattern due to yawning or sneezing effects. It is hoped that by designing the ADU with reserve delivery capacity for both pressure and air mass flow will enable additional breathing demands outside those given for a standard adult patient at rest to be accommodated.

The model controller settings, Table 3.3, are determined empirically to produce a maximum fluctuation in mask pressure within the desired pressure tolerance.

Table 3.4 Model simulation controller settings.

Controller Domain	Model Simulation
Proportional Action	20
Integral Time (s)	0.5
Derivative Time (s)	0.5

3.4.4 Conclusions.

The air delivery specification of an idealised ADU operating within the prototype breathing system have been determined by model simulation, Table 3.3, permitting the ADU element to now be designed. Controller settings, Table 3.4, are based on an idealised ADU element and have been determined empirically to achieve a fluctuation in mask pressure within the desired pressure tolerance. These controller settings will, however, likely change once the ADU model behaviour has been characterised.

3.5 Closure

A model simulation of the I-CPAP breathing system has been developed and proven to accurately predict the behaviour of the prototype system reservoir, air transmission tube and mask system elements. Configuration of the simulation to match equipment used in the prototype system has enabled the minimum air output requirements of the prototype ADU element, yet to be implemented within the prototype system, to be quantified. This permits the design of the compressor within the ADU element to commence.

Chapter 4 Air Delivery Unit

4.1 Introduction

The computer model simulation of the breathing system, Chapter 3, has determined the ADU specifications required to satisfy the prototype breathing system air requirements. A thorough analysis, undertaken within this chapter, indicates a small and portable variable speed double diaphragm compressor, implemented within the ADU, would best meet the air delivery requirements of the prototype breathing system whilst simultaneously satisfying other financial and practical constraints.

Initial design synthesis of the diaphragm air compressor allows both the general configuration and basic geometric boundaries to be identified. This leads to the determination of power and load forces necessary for compressor actuation. Analysis of possible actuation methods identifies the speed controlled, 3 phase AC induction motor as best suited to meet the varying load and speed requirements of the ADU compressor.

Final detailing of the compressor design is undertaken, based on the use of readily available components and materials, to determine the physical characteristics of size and configuration of operational elements. Throughout this process, consideration is given to both minimise complexity of the compressor design and simplify the manufacturing process.

4.2 Air Delivery Unit Selection

Within this section the possible air delivery options available for the breathing system are now reviewed giving consideration to the operational advantages and constraints offered by each option. Two generic types of air compressor options are considered suitable for practical implementation within the prototype breathing system. These are

summarised in the following sections, commencing with non-positive type air compressors – the type utilised in most commercial CPAP breathing devices. A comprehensive discussion of the ADU air supply selection is contained within Appendix B.

Although no details of health requirements for air cleanness are available, it is reasonable to assume that freedom from particulate, chemical and lubricant contamination along with absence from odour are essential operational requirements.

4.2.1 Non-Positive Type Air Compressors

Commonly called fans, due to the relatively low air pressures achieved during operation, these utilise the rotor to add kinetic energy to the air, resulting in an increase in pressure when the flow is partially decelerated at the exhaust port.

Centrifugal single-stage fans are ideally suited for use within CPAP therapy devices since they do not require any form of liquid seal or lubrication, however, they have relatively low air pressure output due to internal leakage and recirculation within the rotor and shroud. Due to the low airflow resistance encountered within the large diameter tube supplying the nasal mask, the low-pressure output is, however, not a problem for the CPAP therapy devices. The model simulation, however, predicts the prototype system will require a supply air pressure of approximately ten times greater than that generated by the commercial CPAP ADU devices. Centrifugal fan performance predictions are used to ascertain if this method of air supply is capable of meeting the prototype requirements. Analysis, based on idealised fan equations [36], of a commercially available CPAP fan unit [8], indicates this ADU should produce a static pressure of 37 cm Wg when operating at a maximum rotational speed of 21,000 rpm. Subsequent testing of this CPAP fan unit confirms these predictions. The option of enlarging this fan from 50mm to 130mm diameter to achieve the higher air pressure required by the prototype system has failed to produce the pressure required by the I-CPAP system, therefore this option will not be considered any further.

Higher air pressures from a centrifugal fan may still be attainable without the problem of utilising higher rotational speeds or enlarged diameter through the use of multistage compression [37]. Based on the idealised assumption that each rotor stage will double the static air pressure, a 5-stage compression will result in improving the commercial fan unit to produce 185 cm Wg pressure. In practice, however, when the fan rotors are assembled in axial alignment on the same shaft, the airflow must turn 180° when passing between stages, resulting in lower efficiencies and hence lower air pressures. Furthermore, consideration must also be given to the air mass flow control, since the higher mass moment of inertia given by a multistage rotor would also increase the delay in the ADU response to variation in mask pressure.

A possible alternative to the multistage fan is the regenerative blower which produces a significantly higher static pressure when compared to the conventional centrifugal fan, however, this device is characterised by a lower efficiency than a multistage centrifugal fan and produces higher noise levels due to increased air turbulence [38]. A literature survey has failed to produce information detailing the performance prediction for these types of fans, however, basic descriptions on operating principles were found [39]. Lack of information and complexity of rotor design prevented this option of air supply from being implemented.

4.2.2 Positive Type Air Compressors

Positive displacement compressors, such as reciprocating and rocking piston, rotary vane, rotary screw and lobed rotor are a good option to achieve very high air pressures and mass flow rates, without the need for high operational speeds. However, contamination of the breathing air through oil or carbon particles is a significant problem encountered in most of these compressor types. Despite refinement in seal quality and the use of metallic coatings to reduce friction, there is still a lubrication requirement and oil carry-over into the air stream is still a problem [40]. The Diaphragm type positive displacement compressor avoids these problems, however, by utilising a thin elastic diaphragm, eliminating the need of piston or compressor scroll lubrication, that isolates the air flow from the operational mechanism if desired and seems a good option for the breathing system under consideration.

4.2.3 Preliminary Considerations

A variable speed multiple-diaphragm compressor is best suited for implementation within the ADU of the prototype breathing system. Although this decision is based on being able to achieve the desired air pressure and flow requirements with minimal design complexity, being portable, avoiding the problem of lubricant air contamination and enabling a range of actuation options to be considered; nevertheless, it is a choice made by Fisher & Paykel Healthcare.

The problem of fluctuations in mask pressure occurring due to the pulsing air discharge characteristic of the diaphragm compressor is considered a possible problem. This effect will, however, be minimised through the use of a twin diaphragm assemblies, operating half a cycle out of phase with each other. Furthermore, the system air reservoir capacitance and the pressure attenuation effects experienced along the 5.5 mm diameter transmission tube will be beneficial in reducing this effect.

The undesirable attributes of noise and vibration, inherent with these types of compressors, is not of primary concern in the prototype breathing system since these problems can be overcome by development at a later stage.

To initiate the compressor thermodynamic analysis and permit actuation options to be considered, it is first necessary to formulate an initial concept based on the practical constraint of having to build the device utilising available resources. The following design parameters are selected, based on experience and availability.

1. The outside diameter of the compressor is initially set at 100 mm diameter since a 4020 aluminium alloy billet is available and makes an ideal material for main housings.
2. Neoprene-nylon diaphragm material, Appendix D3, is selected for its high flexibility and crack resistance. A SolidWorks® finite element model, utilising the same outside diameter as the main housing, Figure 4.1, has

shown that the diaphragm stroke must be limited to 10 mm in order for the material to be within allowable stress levels.

3. The use of two diaphragm assemblies, co-axially opposed, enables a single actuator of either oscillating linear or rotary type to be utilised and enables favourable phasing to minimise air pressure fluctuations.

4.3 Compressor Design

In this section, a summary of all the necessary steps undertaken by this research to produce the diaphragm air compressor is presented.

4.3.1 Compressor Thermodynamic Design

Detailed sizing of the twin diaphragm compressor assembly is achieved by considering the compressor thermodynamic cycle, based on meeting the system maximum air pressure and flow requirements, previously given in Table 3.3.

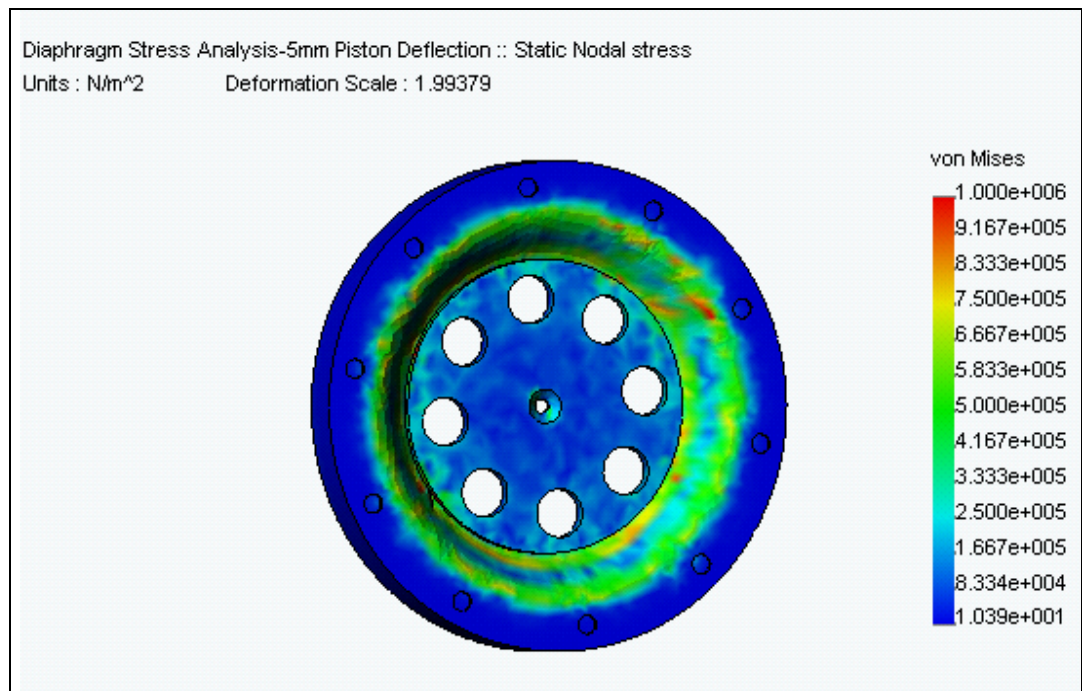


Figure 4.1 Finite element model of diaphragm stress at 5mm displacement.

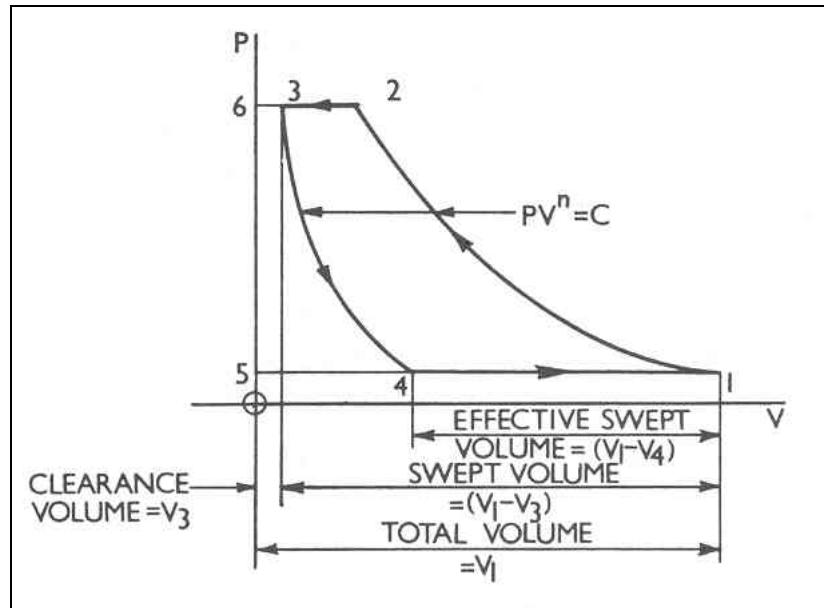


Figure 4.2 Typical diaphragm compressor pressure-volume cycle.

Since the maximum air gauge pressure required by the prototype system is 17 kPa, this relatively low value allows us to assume constant absolute air properties during the compression cycle. These are given at 101 kPa and 289 K for air pressure and temperature respectively.

4.3.2 Swept Volume

In this work an effective diaphragm diameter of 80 mm is assumed, based on the fact that the main casing has an outside diameter of 100 mm and allows a 10 mm wide sealing surface around the periphery of the diaphragm.

The swept volume of each diaphragm ($V_1 - V_3$), Figures 4.2 and 4.3, is determined by assuming the diaphragm membrane is stretched taut at the two extreme positions of full stroke. Implementing an assumed maximum diaphragm stroke of 10 mm and central rigid piston diameter of 60 mm leads to the swept volume of 39.27 ml.

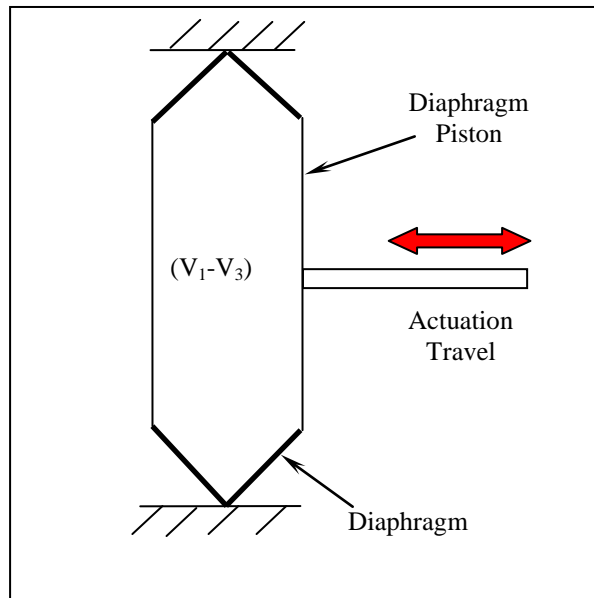


Figure 4.3 Diaphragm swept volume measured at extremes of stroke.

4.3.3 Clearance Volume

The determination of the desired compressor clearance volume (V_3), Figure 4.2, is achieved by balancing two requirements; the desire to produce a compressor with a relatively high volumetric efficiency requiring a minimal clearance volume and the need to avoid mechanical contact between fixed and moving components. On this basis, a clearance volume of 10% swept volume is assumed, giving a clearance volume of 3.927 ml.

4.3.4 Total Volume

The maximum volume of each diaphragm chamber (V_1), Figure 4.2, must be determined for further computation. This is found by summing the swept volume ($V_1 - V_3$) and the clearance volume (V_3). For the present compressor the total chamber volume is 43.197 ml.

4.3.5 Volume at Commencement of Induction

The diaphragm chamber volume at the point where air enters (V_4), Figure 4.2, must be determined for further computation and is based on the assumption of a pressure drop across the inlet valve of 4 kPa, resulting in an absolute inlet air pressure (P_3) of 97 kPa. The compressor discharge air absolute pressure (P_4) must

exceed 118 kPa to meet the system requirements, previously given in Table 3.5, determining the diaphragm chamber volume at commencement of induction. Assuming isothermal gas compression due to relatively low pressure ratio between compressor inlet and discharge results in:

$$V_4 = V_3 \left(\frac{P_3}{P_4} \right) \quad (4.1)$$

leading to a chamber volume at the commencement of induction of 4.777 ml.

4.3.6 Effective Volume

It is necessary to account for the expansion of the air trapped in the clearance volume leading to a reduction in the swept volume since this reduces the total volume of air delivered. This can be implemented by subtracting the volume at commencement of induction (V_4) from the total volume (V_1) resulting in an effective volume of 38.420 ml.

4.3.7 Volume of Free Air Delivered

The discharge air volume flow rate, corrected to atmospheric pressure and temperature, termed volume of free air delivered (V_f), is now determined. For isothermal gas compression, the general gas equation can be written as:

$$V_f = \frac{P_1}{P_f} (V_1 - V_4) \quad (4.2)$$

where P_1 and P_f represent the inlet and free air absolute pressures, respectively. Using the values previously obtained leads to a volume of free air delivered per compression cycle of 36.898 ml.

4.3.8 Maximum Air Mass Discharge Rate

It is undesirable to operate the compressor at high speeds, since this will result in increased noise, reduction in volumetric efficiency and additional forces on compressor actuation components. The maximum compressor speed is based on

readily attainable commercial rotary and linear actuators achieving a maximum compressor speed of 1200 cycles per minute (cpm). Assuming a compressor volumetric efficiency (η_{vol}) of 90%, based on losses due to the effects of valves, the air mass flow rate from the compressor discharge can be calculated using:

$$M_{c,max} = V_f \times n \times C \times \rho \times \eta_{vol} \quad (4.3)$$

Considering the number of diaphragm assemblies, $n = 2$, and the compressor speed, $C = 20$ cycles per second, results in a maximum compressor air discharge mass flow rate of 1.59 g/s.

The calculated diaphragm compressor air delivery mass flow rate of 1.59 g/s is slightly higher than the 1.45 g/s predicted as necessary by the model simulation, however as mentioned earlier, it is prudent to allow for reserve capacity in air supply to account for rapid and unpredicted changes in patient breathing requirements. For brevity, all other details are summarised in Table 4.1.

Table 4.1 Summary of diaphragm compressor thermodynamic design specifications.

Swept Volume	0.00003927 m ³
Clearance Volume	0.000003927 m ³
Effective Swept Volume	0.000038365 m ³
Total Volume	0.000043197 m ³
Volume of Free Air Delivered	0.000036846 m ³
Maximum Air Mass Outflow	1.59 g/s
Absolute Inlet Air Pressure	97 kPa
Absolute Maximum Outflow Air Pressure	118 kPa
Maximum Compressor Speed	1200 cpm

4.4 Actuation Requirements

In this section, calculations are made to determine the force and power requirements for both linear and rotary methods to actuate the compressor diaphragm, based on a maximum compressor air gauge pressure of 18 kPa. No account is made for inertia forces, due to reciprocating, oscillating or rotational inertia forces since at this stage the mass of the moving components is not yet known. To achieve rapid speed of compressor response, requiring additional motor torque, it is intended that the power of driving motor selected will be double that necessary for maximum steady state power requirement [41].

Electrical diaphragm compressor actuation devices, considered to be both practical to implement and capable of providing oscillating linear, oscillating rotary and continuous rotary motion are reviewed with respect to meeting the speed and power characteristics necessary to drive the compressor.

4.4.1 Diaphragm Gas Pressure Force

Considering the normal force exerted on the diaphragm of active diameter 80 mm by an air gauge pressure of 18 kPa results in a pressure force of 90.48 N.

4.4.2 Power Requirement

Calculation has determined that 0.91 J of work (W_d) is required, per compression cycle, to move the diaphragm against the air pressure force over a stroke length of 10 mm. Preliminary compressor design synthesis, Sections 4.2.3 and 4.3.8, has already identified the need to have 2 compression cycles, directly out of phase, to minimise the discharge pressure fluctuations, and maximum actuation speed (n_{max}) should be 1200 cpm. The maximum compressor power requirement (W_{max}) can be determined from:

$$W_{max} = \frac{2 \times W_d \times n_{max}}{60} \quad (4.4)$$

Giving due considerations to achieving rapid compressor acceleration, the minimum motor power requirement is estimated to be 146 W.

4.5 Actuation Selection

It is necessary at this stage to determine the most suitable form of compressor actuation since, for the ADU to be compact; the compressor main housing should contain as much of the actuation element as possible. Within this section, a summarised review of possible compressor actuators is presented and final conclusions made. Performance data for actuators considered is contained within Appendix C.

The simplest method to achieve oscillating linear motion to stroke the diaphragm within the compressor would be by direct acting solenoid, eliminating the need for any secondary driving mechanism. Electrical problems normally associated with solenoids, such as coil inductive load and voltage spikes, are easily resolved through rectification and suppression methods [42].

4.5.1 Direct Acting Solenoid

These types of actuators are available with either a single push or pull action, requiring a return spring to return the two diaphragm assemblies, effectively doubling the actuation force required. Appendix C1 gives solenoid performance data; however, these were not selected in this research due to the following facts:

1. The force available from direct acting solenoids, over their stroke range, has the unfavourable characteristic of rapidly diminishing as the stroke increases, making them unsuited for diaphragm compressor actuation
2. This type of actuation produces insufficient force to actuate the diaphragm assembly unless the diaphragm size is reduced. Although this would reduce the gas pressure force, the compressor would then be required to operate at a higher speed in order to produce the same air mass flow, leading to an increase in inertia forces that would likely offset any benefits gained.

4.5.2 Linear Motor

To achieve continuous oscillating linear motion, the linear servomotor requires an ac inverter and positional feedback to control the speed and direction at which the thrust tube travels [43]. The high inertia forces generated by thrust tube mass

diminish the output force when operating at the maximum compressor operating frequency of 20 Hz. Commercial units capable of providing sufficient force cannot dissipate the heat energy generated by the coil, resulting in a very short operational time. Appendix C2 gives performance data for this type of actuator; however, it is also eliminated from consideration due to the following facts:

1. A quote of approximately NZ \$16,000 to build a special linear actuator capable of continuous actuation of the diaphragm compressor was beyond the financial resources available for this project [44].
2. Despite the linear induction motor being identical in construction to the linear servomotor this form of actuation is impractical since there is no feedback signal to compensate for the inherent slip present between the fixed coil and moving tube magnets [45].
3. Platen type linear step motors provide insufficient actuation force and are too slow in operation to achieve the desired compressor output [46].
4. The screw-type linear step motor displaces a threaded shaft by converting the motion of a rotary step motor into a linear actuation by driving a threaded nut [47]. This method of linear actuation offers the advantage of being cheaper than the platen type; however, it still requires the microprocessor controller to operate the stepping function which makes it more costly than other options. This actuator is also likely to be incapable of achieving the desired oscillating speed of 20 Hz due to the mass moment of inertia of its rotating motor components. Commercially available units, capable of meeting the desired speed of operation, utilise a coarse pitch screw thread and high motor step increment to achieve the required diaphragm displacement of 10mm. Unfortunately, there is no information to support this motion being achieved at 20 cycles per second.

4.5.3 Oscillating Rotary Actuation

Achieving an oscillating linear motion to actuate the diaphragm compressor requires the simple crank system, shown in Figure 4.4.

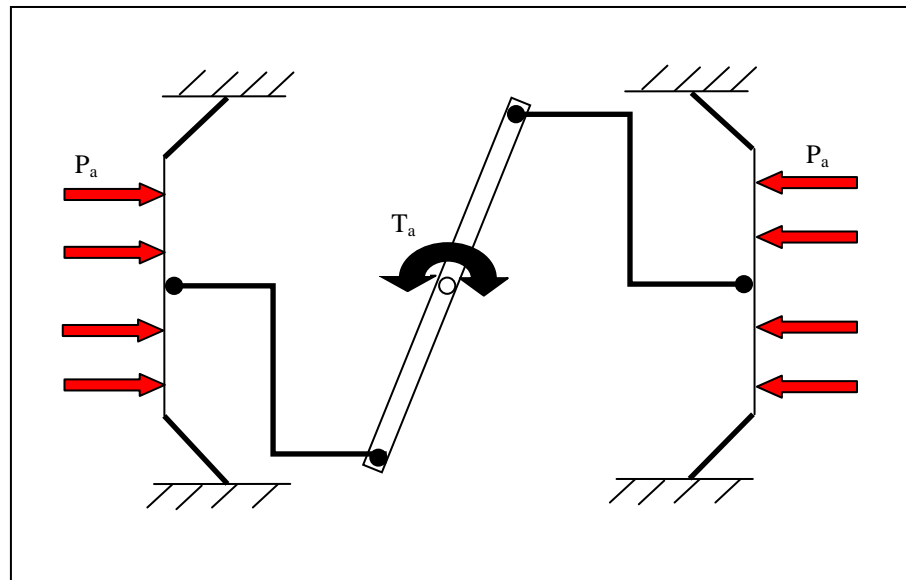


Figure 4.4 Schematic representation of oscillating rotary actuator mechanism.

The linear displacement of the diaphragm is governed by both the crank offset and the angle of actuator rotation. A total rotary actuation displacement of 45° is chosen, requiring an actuator crank offset of 12.73 mm to achieve the desired diaphragm stroke. Analysis of this actuation method determines an actuation torque (T_a) of 3.33 N-m is required to oppose the maximum diaphragm air pressure force.

Several different types of rotary solenoids are assessed for use in this research; however, both the high torque output brushless torque actuator (BTA) [48] and similar alternative types of solenoids all proved incapable of providing sufficient torque to actuate the diaphragm compressor [49]. Appendix C3 details the performance data for these solenoids, however, this type of actuator is eliminated from consideration since the maximum rated operation is very close to the compressor speed of 20 Hz, preventing the reduction of diaphragm area to reduce the actuation torque requirement.

4.5.4 Continuous Rotary Actuation

A simple continuous crank mechanism, Figure 4.5, offers an alternative to the rotary oscillating actuators previously discussed and enables higher torques and speeds to be utilised. The negative mass moment of inertia effect of the crank and oscillating components can easily be overcome by utilising an actuator of higher

torque capability. Calculation of torque requirement to actuate this system is achieved by considering a connecting rod, normal to the crank offset (S_c) of 5 mm, acting against maximum air pressure, requiring a minimum continuous actuation torque of 0.634 N-m. Considering the proposed double diaphragm assembly, the worst possible loading would be for both diaphragms to act together resulting in a minimum actuation torque of 1.27 N-m. Based on the proposed operational speed of 1200 cpm, the power requirement for this type of actuation system is 159.6 W.

The precision speed and position control offered by stepper motors lends them to being the most suitable form of actuation when combined with a simple crank mechanism, however, these motors trade off available torque for shaft speed with resultant desynchronising or ‘stalling’ of the motor occurring when utilising small step increments to achieve the desired torque at high frequencies [50].

To achieve the maximum compressor speed of 20 Hz, the motor must have a step size of no smaller than 7.5 degree per step for a 4 pole motor to avoid the problem of desynchronising occurring. Appendix C4 details typical stepper motor performance data, however, despite an extensive search, no commercially available units were found that met the compressor requirements.

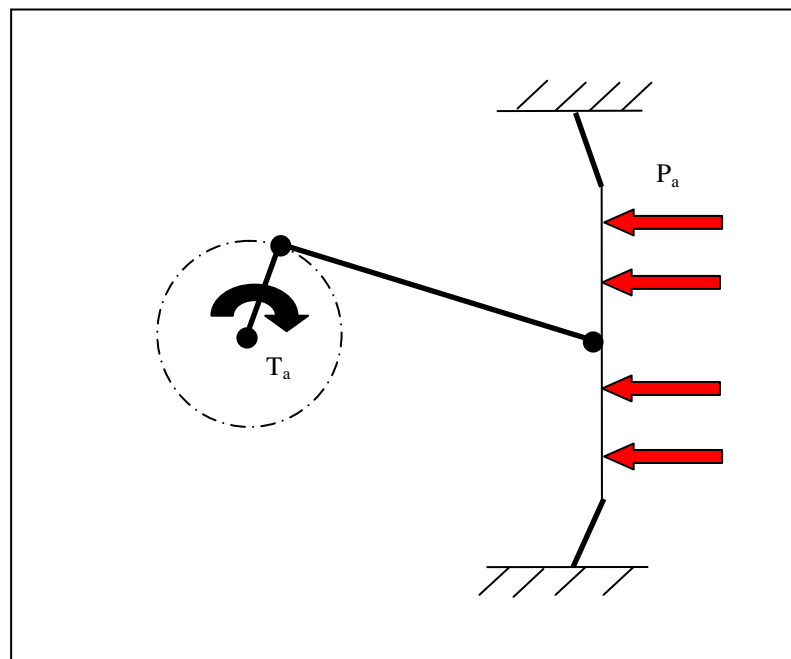


Figure 4.5 Schematic representation of continuous rotary actuator crank mechanism.

Alternating current (AC) servomotors achieve accurate speed control, despite dynamic variation in loading occurring by utilising inverter frequency control and rotary encoder feedback of both angular position and rotational velocity [51]. Appendix C5 contains performance data for this actuator which, although ideally suited to actuate the compressor, contain the unnecessary feature of positional control which adds significantly to the purchase cost. To minimise cost, both the direct current (DC) and AC speed control motors are now considered as alternatives to the servomotor.

Speed control of DC electric motors is achieved through voltage control, however, the operational characteristics of the motor needs to be consideration. Shunt wound DC motors produce low torque figures during start up and at low speeds, Appendix C6, making them unsuited to diaphragm compressor actuation [52]. Series wound DC motors produce maximum torque at low speeds; Appendix C6, however, this value diminishes rapidly as armature speed increases making them unsuited for compressor actuation. There is also the undesirable tendency for series wound DC motors to over-speed when unloaded. The DC compound motor has a combination of series and shunt windings, allowing this type to have the torque characteristics of the series motor combined with the speed characteristics of the shunt motor. Despite the potential of DC compound motor to actuate the compressor all DC motors suffer a falloff in driving torque when the applied voltage is reduced for speed control, Appendix C6. All these characteristics make DC motors unsuited to drive the compressor due to the dynamic variation in compressor loads experienced.

AC induction motor, however, offer the advantage over the DC types by producing a torque output that is proportional to the applied load, due to armature slip, making them ideally suited to the varying speed and loading requirements of the compressor. This characteristic produces a starting torque of up to 150% greater than the rated full load torque and a pullout torque of up to 250% greater than rated full load torque [52], Appendix C7. Speed control can easily be achieved through the use of an AC frequency inverter, which although costly, is offset by the relatively inexpensive motor. Three phase AC motors offer additional advantages of self starting due to the rotating field in the stator

producing a rotating magnetic field and an almost uniform running torque, rather than a pulsating torque characteristic of single phase types.

4.5.5 Actuator Selection

The combined speed and torque characteristics of the inverter speed controlled 3 phase AC induction motor make it the most practical means by which to actuate the diaphragm compressor. Readily available and affordable units make this type of compressor actuation the most practical choice. Technical data for both motor and speed controller is contained within Appendices C8 and C9 respectively.

4.6 Compressor Detailing

Within this section, design detailing of the double diaphragm compressor is undertaken with the goal of achieving simplicity of design and minimising the number of parts required by providing multiple function for individual compressor components wherever possible.

4.6.1 Design Detailing

Below is a summary of the compressor design, however, a complete set of compressor assembly and detail drawings is given in Appendix D4.

1. Reed valves are the obvious choice to minimise the pressure drop provided the air can act over a large area. Plastic transparency film, Appendix D1, is used for the reed valves because this material is compliant in bending yet sufficiently rigid to avoid distortion under the action of air pressure. Valves are located within the compressor to take advantage of the area over which the pressure acts.
2. Four small meshing gear sets, Figure 4.6, double up as crankshafts, enabling dual connecting rods to actuate each diaphragm assembly. This distributes the load carried by each gear tooth and increases the connecting rod bearing surface area. The counter rotating actuation gears, actuating each

diaphragm, also eliminate side thrust on the diaphragm, improving diaphragm life and eliminate secondary mechanical imbalance. Standard 20° pressure angle metric gear form is determined from standard gear equations, however, gear tooth strength, Section 4.5.1, is based on first principles analysis.

3. The gear main shafts are mounted on paired sealed ball bearing races, eliminating the possibility of oil contaminating the air whilst simultaneously sealing the compressor input drive shaft against air leaks. The bearing radial load capacity is checked against gear radial reaction forces, Section 4.7.4.
4. The co-axial diaphragm design utilises the central compressor actuation housing as an air discharge manifold for the two diaphragm air streams. The gear sets are paired in dry lubricant impregnated nylon [53], Appendix D2, and aluminium alloy mesh sets to minimise any possible contamination of the air.

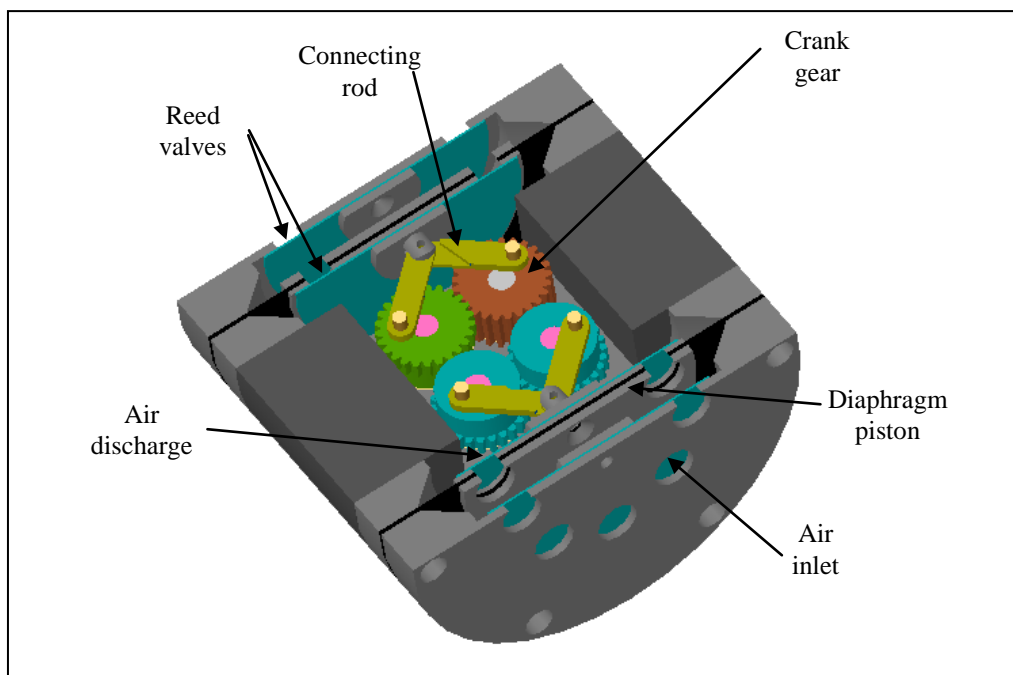


Figure 4.6 Sectional view of diaphragm compressor.

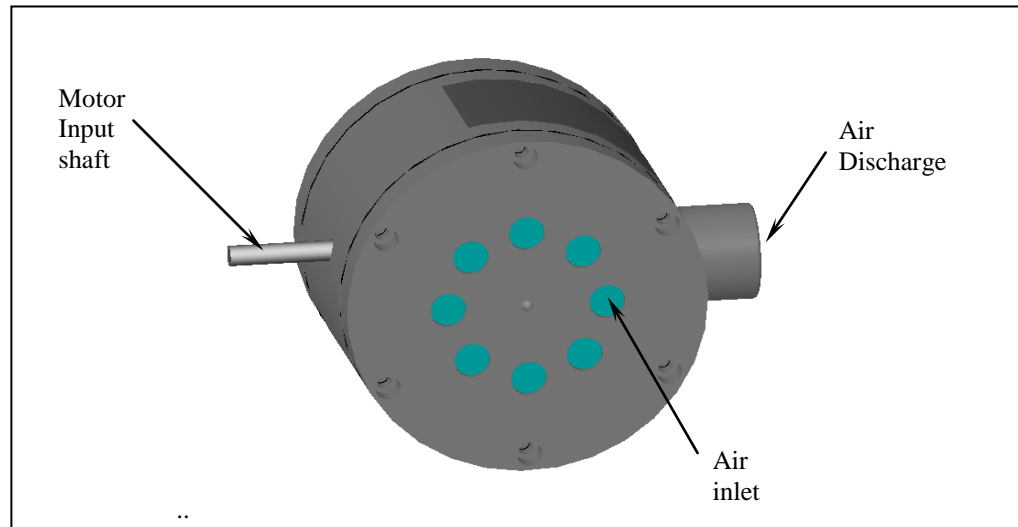


Figure 4.7 Completed diaphragm compressor.

5. The short connecting rods, made from 60/40 brass, require only a wipe of castor oil, selected for its non-toxic nature and high shear resistance properties, during final assembly.

4.7 Gear and Bearing Loads

In this section, a summary of all the necessary steps undertaken by this research to verify gear strength and bearing load capacity is presented.

4.7.1 Gear Design

Gear design is based on standard spur gear design principles; however, final selection of gear size and number of teeth was restricted by available gear hobs. Initial gear sizing is based on a gear centre distance of 20 mm, Figure 4.8, representing the closest centre distance the bearings, available to support the gears, could be located.

Offset teeth are utilised in the opposing diaphragm idlers gears 1 and 4, Figures 4.8 and 4.9, preventing these two gears from meshing which avoids compounding tooth pitch errors causing cyclic binding of the gears.

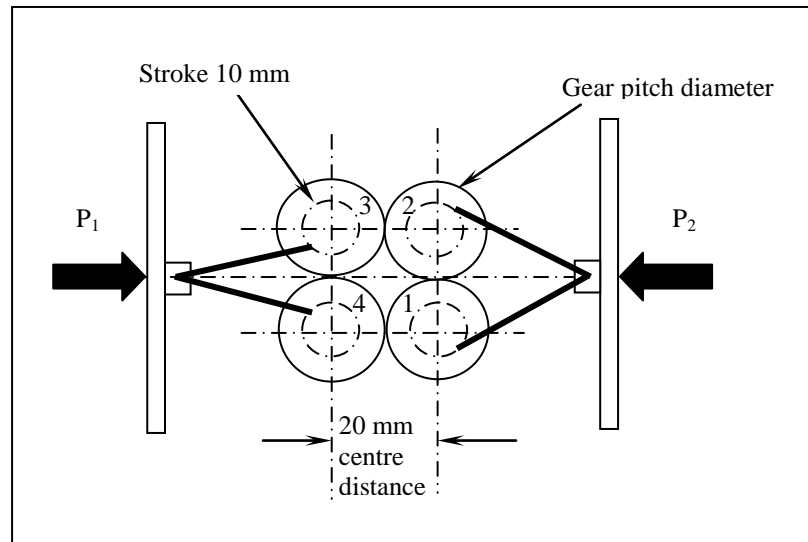


Figure 4.8 Schematic representation of compressor crank-gear actuation.

The smallest gear hob available, module (m) of 0.8, is utilised to minimise the compressor discharge volume and produce a compact prototype compressor unit. Each gear is determined to have 25 teeth (N) to avoid undercutting occurring at the root of the teeth leading to subsequent premature failure [41]. Based on these two requirements the gear pitch diameter (D) can be calculated [54] from:

$$D = m \times N \quad (4.5)$$

leading to the gear pitch diameter of 20 mm, with no backlash allowance, this dimension also represents the gear centre distances, Figure 4.8. With the gears also being utilised as crankshafts, Figure 4.10, requires the gear root diameter (D_{\min}) to exceed the compressor stroke of 10 mm. This is calculated by initially calculating the gear tooth dedendum height (K), derived from:

$$K = 1.157 \times m \quad (4.6)$$

resulting in a gear tooth dedendum height of 0.926 mm.

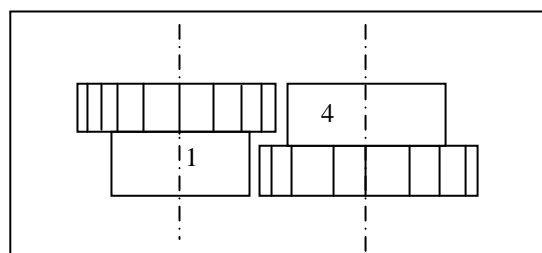


Figure 4.9 Side view of offset idler half width gears.

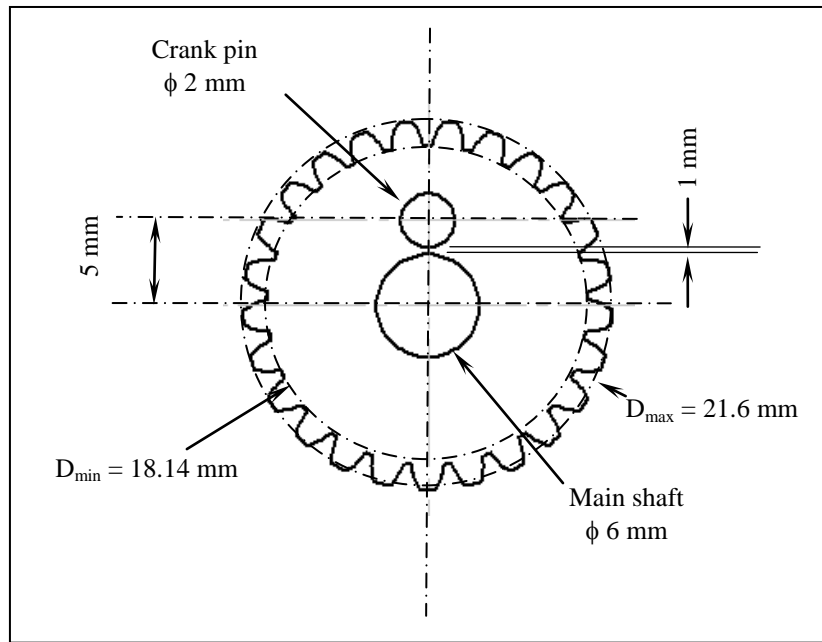


Figure 4.10 Gear crankshaft dimensions.

Since standard metric spur gear form is utilised, the root diameter is calculated from:

$$D_{\min} = D - (2 \times K) \quad (4.7)$$

leading to a gear minor diameter of 18.14 mm, well clear of the offset crank pin. The gear major diameter (D_{\max}) is calculated from:

$$D_{\max} = D + (2 \times J) \quad (4.8)$$

where the gear addendum height (J), equalling the gear module, gives a gear major diameter of 21.60 mm.

The compressor is driven through the main shaft of gear 3, Figure 4.8, with the driving torque path alternating between gear mesh sets 3-4 and 3-2-1 due to the offset phasing of the diaphragm compression strokes. Gears 2 and 3 are full width, nominally set at 10 mm, since they transmit the greatest force whereas the offset idler gears 1 and 4 carry half the force, permitting a reduction in tooth width. To provide 2 mm side clearance between these two idler gears, a tooth width of 4 mm is required.

Consideration is now given to the practicality of the proposed compressor actuator gear geometry. Utilising standard silver steel for both the gear main shaft of diameter 6 mm, determined by the available main bearings, and crank pin of 2 mm diameter, the smallest available, Figure 4.10, results in 1 mm of gear material between the two shafts.

4.7.2 Gear Forces

Calculation of gear forces is based on the maximum constant torque available from the driving motor rather than using the maximum diaphragm pressure force since this represents the maximum operational torque available.

With each diaphragm compression cycle being out of phase, the motor power (P_m) is assumed to be alternatively transmitted between either diaphragm gear sets, resulting in:

$$T = \frac{P_m}{2\pi n} \quad (4.9)$$

where the gear speed (n) in rev/sec produces a gear torque loading (T) of 1.43 N-m. Resolving gear forces onto tangential (F_t) and separating (F_s) components, Figure 4.11, enables both the gear stress levels and bearing reactions to be determined. Assuming the motor input torque is distributed equally to gears 3 and 4 and acts against the maximum air pressure force in diaphragm 1 (P_1), gear tangential force (F_t) is calculated from:

$$F_t = \frac{T}{D} \quad (4.10)$$

resulting in a maximum tangential force of 71.5 N. Maximum gear separating force, occurring between gears 3 and 4 is expressed as a function of gear tangential force and pressure angle (ϕ), using:

$$F_s = F_t \tan \phi \quad (4.11)$$

resulting in a maximum gear separation force of 26N for a pressure angle of 20°.

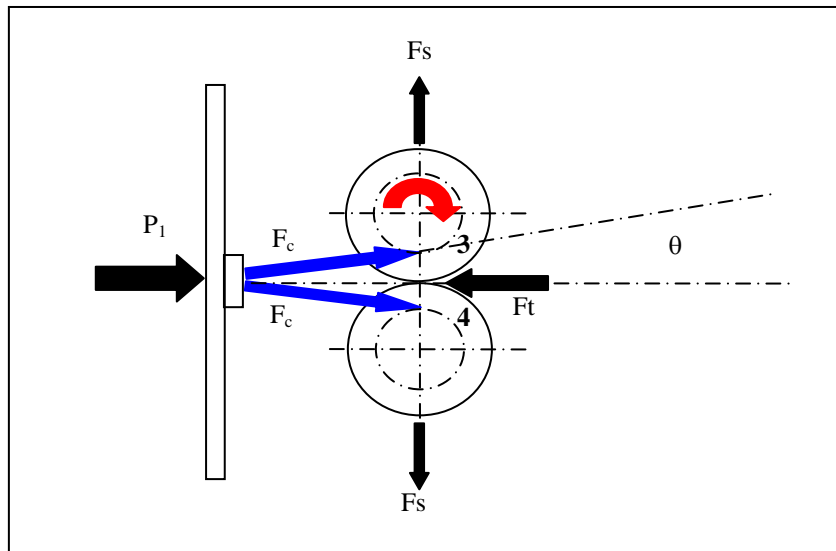


Figure 4.11 Gear forces.

The total gear radial force (F_r) is now expressed as a summation of both tangential and separating components, using:

$$F_r = \sqrt{F_t^2 + F_s^2} \quad (4.12)$$

resulting in a maximum gear radial force of 76.09 N.

The maximum connecting rod reaction force (F_c) fluctuates with variation in angular position (θ), Figure 4.11, and is calculated from:

$$F_c = \frac{P_1}{2 \times \cos\theta} \quad (4.13)$$

results in a maximum connecting rod reaction force of 85.30 N when considering the worst case loading scenario, where angle θ is 40° from the horizontal and maximum air pressure force (P_1) equals 90.48 N, given in Section 4.4.1.

4.7.3 Gear Tooth Strength

Calculation is now undertaken to ascertain the gear tooth strength based on previously determined gear forces. Initial gear module selection, based on design power, confirms the module size of 0.8 as being appropriate to transmit 180 W of motor power, however, this is based on the use of steel gears [41]. Normally gear strength calculations involve a complex series of equations, based on empirically

derived load and fatigue factors determined when using common gear materials such as steel. The prototype compressor, however, uses crank-gear sets meshed in aluminium and nylon pairs to avoid lubrication contamination of the air. Since these materials are not traditionally utilised in gear design it requires an analysis, based on first principles, utilising the strength properties of the weaker material, impregnated nylon 66 [53].

By considering the gear tooth to be a simple cantilever, Figure 4.12, with a tangential force (F_t) of 71.5 N applied at the pitch diameter results in:

$$M = F_t \times 1.157m \quad (4.14)$$

giving a maximum bending moment (M) at the root of the tooth of 0.066 N-m.

Conservatively assuming the tooth root thickness (t) is the same as the tooth chord thickness, at the pitch diameter, calculated from:

$$t = D \sin \frac{90}{N} \quad (4.15)$$

results in a tooth root thickness of a 1.26 mm

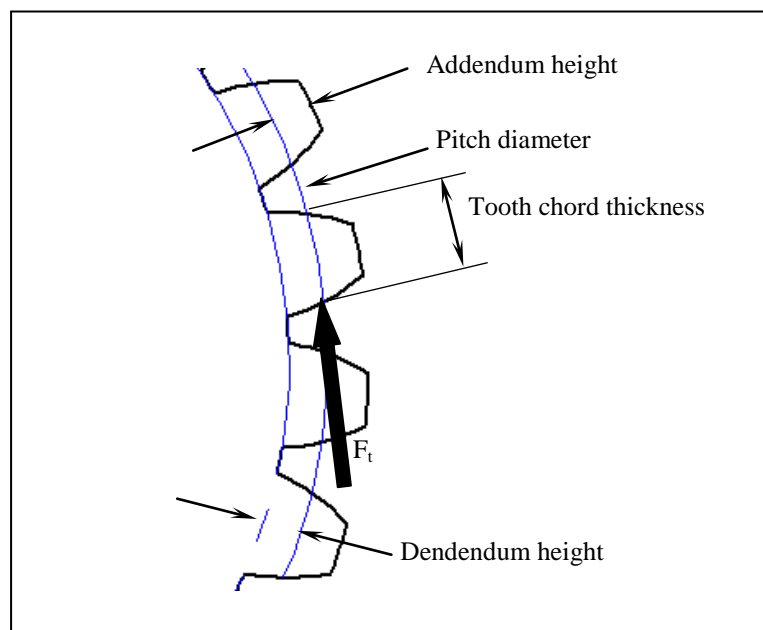


Figure 4.12 Gear strength analysis.

The maximum bending stress at the tooth root (σ_t) is calculated by assuming only one tooth carries the full driving force at any one time. By applying elementary beam theory, based on the second moment of area across the tooth root section (I), using:

$$\sigma_t = \frac{M \times t}{I} \quad (4.10)$$

results in a maximum bending stress of 31 MPa and 24.95 MPa for the 4 mm and 10 mm width gears respectively.

Gear shear stresses at the tooth root (τ_t) can again be calculated from elementary beam theory, for both tooth widths (W) using:

$$\tau_t = \frac{F_t}{W \times t} \quad (4.11)$$

results in shear stress of 5.7 MPa and 14.1 MPa for the 10 mm and 4 mm wide gears respectively.

Principal bending and shear stresses, (σ_{\max}) and (τ_{\max}) respectively, are determined by combining the induced bending (σ_t) and shear stresses (τ_t) in a two dimensional stress analysis, given by:

$$\sigma_{t,\max} = \frac{\sigma_t}{2} \pm \frac{1}{2} \sqrt{\sigma_t^2 + 4\tau_t^2} \quad (4.12)$$

$$\tau_{t,\max} = \pm \frac{1}{2} \sqrt{\sigma_t^2 + 4\tau_t^2} \quad (4.13)$$

Both calculations for maximum bending and shear stresses, using the higher stresses induced within the thinner idler gears, results in values of 31 MPa and 15 MPa respectively, well within the maximum values specified by the manufacturer of the nylon gears, Table 4.2, [53].

Table 4.2 Comparison between design and manufacturer maximum stress levels for GS nylon 66 gears [53].

	Design Calculated Stress (Mpa)	Manufacturer Maximum Stress (Mpa)
Bending stress (σ_{\max})	31	86
Shear Stress (τ_{\max})	15	72

4.7.4 Bearing Loads

Maximum bearing radial force (F_{br}) is determined by considering the worst case scenario of both the maximum connecting rod force (F_c) and total gear radial force (F_r), Section 4.7.2, acting together on the gear crank, Figure 4.13, supported on double 6260XX deep groove ball bearings available for this project. By taking moments about the support bearing furthest from the gear results in a maximum applied bearing radial force of (P_{brg}) 538 N. This represents the equivalent basic dynamic bearing load, since there is no axial force applied, and is well within the 2.3 kN basic radial load (C_{brg}) specified by the manufacturer for this bearing [55].

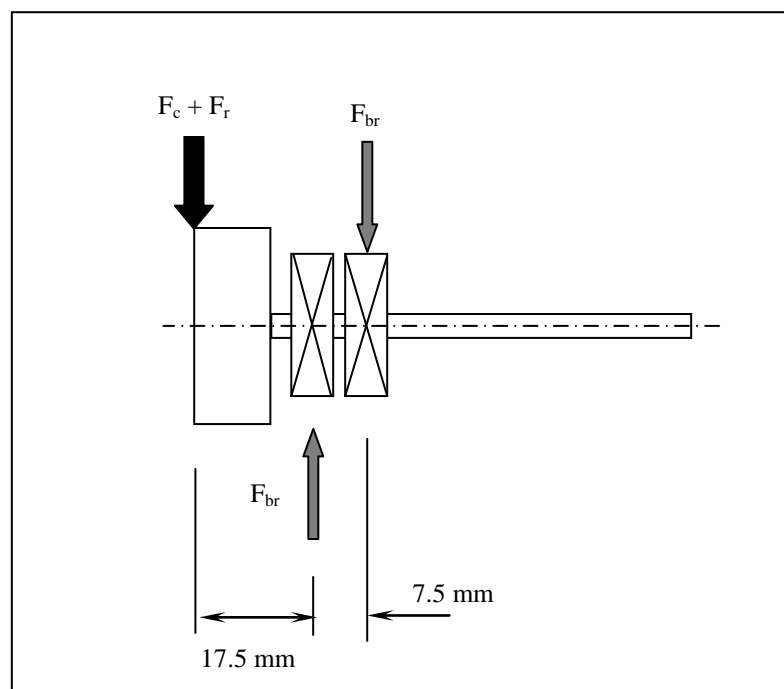


Figure 4.13 Bearing radial loads due to diaphragm air pressure force.

Basic rated bearing life (L_{10}), for 90% reliability, calculated from:

$$L_{10} = \left(\frac{C_{\text{brg}}}{P_{\text{brg}}} \right)^3 \quad (4.14)$$

results in a predicted bearing life of 61.4 million revolutions, more than sufficient for the prototype compressor

4.8 Closure

A mechanically actuated double diaphragm compressor has been designed to meet the prototype breathing system requirements, identified by system modelling. When driven by a variable speed 3 phase AC motor, regulated by a motor speed controller, forms the completed ADU element within the prototype breathing system.

Chapter 5 Testing Air Delivery Unit

5.1 Introduction

In this chapter the compressor is tested under both steady state and dynamic conditions to validate that it meets the I-CPAP system requirements, identified by model simulation.

The idealised zero order ADU element, previously utilised within the model simulation, is replaced by the characterised behaviour of the prototype ADU. Subsequent testing of the model, under simulated patient breathing load, is undertaken to verify that the ADU is capable of meeting the air requirements of the prototype system.

A direct comparison is also made between the completed prototype breathing system and model simulation under simulated patient breathing load.

5.2 Steady State Compressor Testing

In this section the performance characteristics of the diaphragm compressor are determined and assessed against the requirements predicted by the model simulation.

5.2.1 Test Setup

A schematic representation of the experimental setup used to determine the compressor characteristics is shown in Figure 5.1 and consists of the compressor attached to a mounting plate, supported on four small rubber feet, and driven by a variable speed electric motor attached to the compressor coupling.

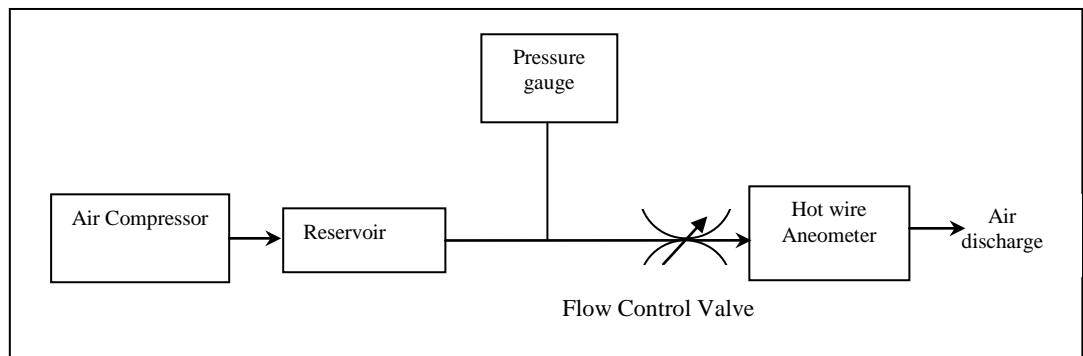


Figure 5.1 Schematic representation of steady state compressor test setup.

Air, discharged from the compressor, passes through the reservoir into a test manifold containing both a Bourdon tube pressure gauge, measuring reservoir air pressure, and a tapered needle valve, controlling the air mass flow rate being discharged to atmosphere. Connected in series to the discharge air stream is a hot wire anemometer used to measure the discharge air mass flow rate. Detail of equipment used is given in Table 5.1.

The experimental procedure consisted of operating the compressor at a constant speed whilst varying the air mass flow rate from the reservoir by adjusting the needle flow control valve to achieve increments in reservoir pressure, up to a maximum of 250 cm Wg. Air mass flow rate from the reservoir was recorded during each pressure increment.

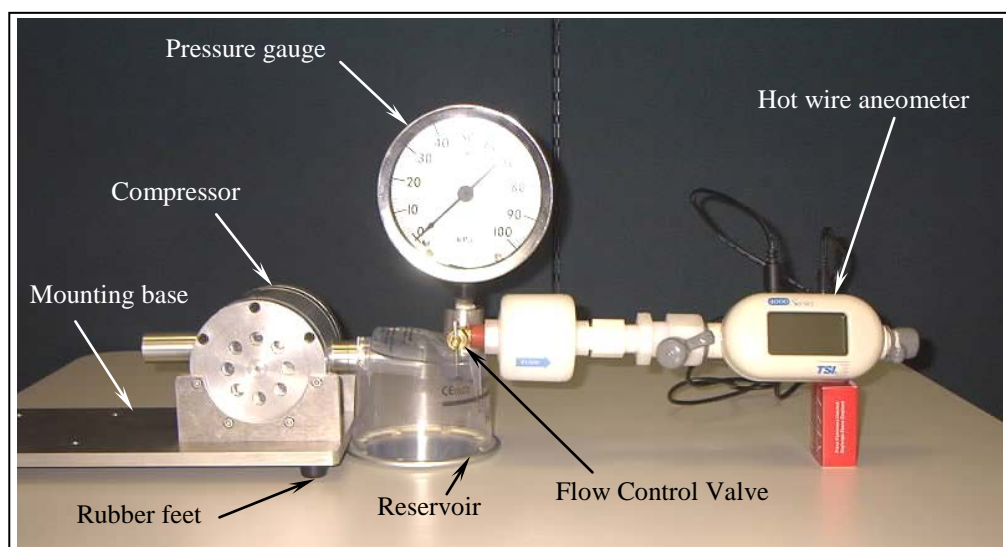


Figure 5.2 Steady state testing of diaphragm compressor.

Table 5.1 Detail of equipment used in compressor steady state test.

Equipment	Identification
TSI Hot Wire Anemometer	TSI 4050 34221
Pressure Gauge	0 – 100 kPa Aschroft 8437

5.2.2 Results

Compressor air mass flow rate, Figure 5.3, is shown as a function of pressure and operating speed. Also shown is the minimum air requirement of the prototype system, determined by model simulation. It is worth noting that the compressor steady state performance meets the prototype system air requirements identified by model simulation.

Fluctuations in reservoir pressure were noticed during steady state testing, when operating the compressor at low speeds of around 500 rpm and at reservoir gauge pressures above 20 kPa. This behaviour is attributed to the discharge characteristics of the double diaphragms, however, it is not likely to give operational problems within the breathing system for reasons given in Section 4.2.3. This behaviour did, however, require a visual average pressure to be recorded.

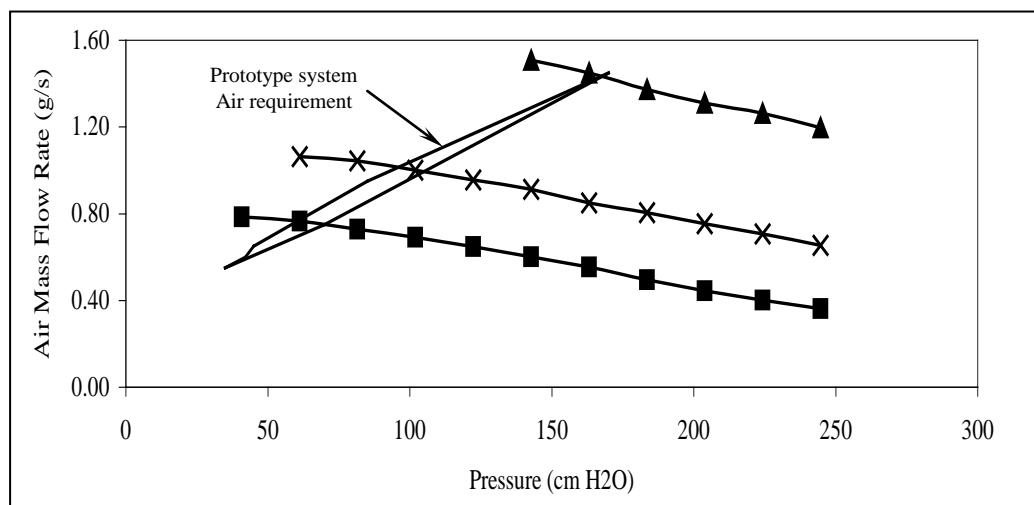


Figure 5.3 Steady state compressor performance over range of speeds; — model simulation operating envelope, ■ 500 rpm, x 750 rpm, ▲ 1000 rpm.

5.3 Assembly of Air Delivery Unit

Within this section, final assembly of the prototype ADU, incorporating the compressor, Figure 5.4, is undertaken. This required the compressor to be connected to the 3-phase speed controlled AC electric motor by means of a keyed rigid coupling and directly mounted to the compressor mounting plate. Regulation of compressor speed is achieved through a motor speed controller incorporating proportional, integral and derivative (PID) control action. The speed controller power supply is hardwired to a single phase domestic 3-pin plug via a 2 amp circuit breaker, and flexible wire links the speed controller to the motor.

5.4 Dynamic Testing Of Air Delivery Unit

In this section the dynamic performance characteristics of the completed ADU are determined to allow the dynamic behaviour of this element within the model simulation to be predicted.

Previously, the model simulation utilised an idealised, zero order, ADU behaviour, however, characterisation of this element is now required to permit the assessment of completed ADU performance.

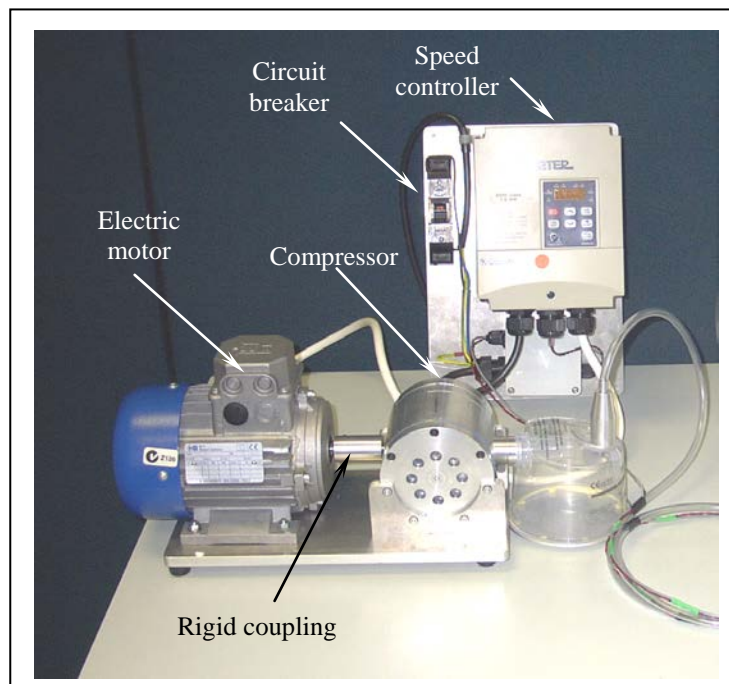


Figure 5.4 Completed air delivery unit.

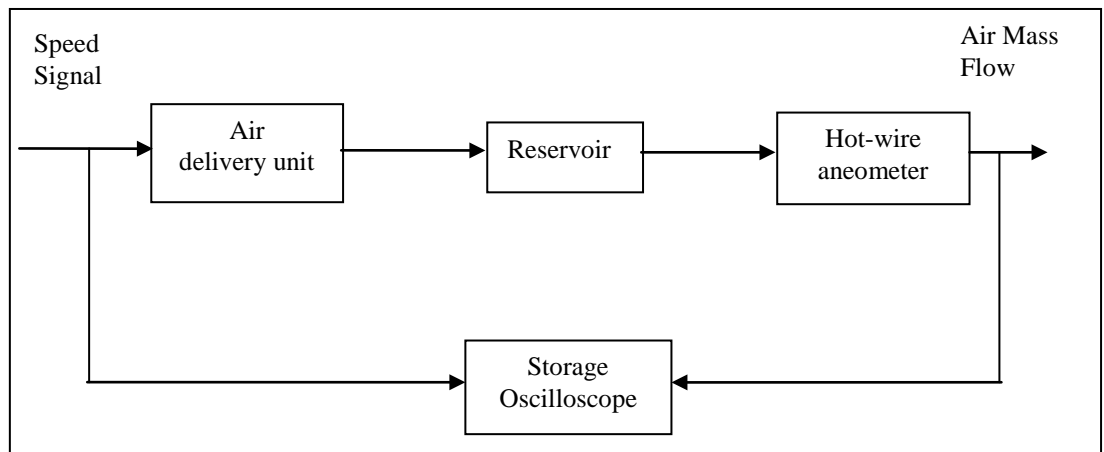


Figure 5.5 Schematic representation of ADU dynamic test setup.

5.4.1 Test Setup

Figure 5.5 shows the schematic representation of the experimental setup used to determine the dynamic behaviour of the completed ADU. The apparatus, Figure 5.6, consisted of the complete ADU, configured for manual operation of compressor speed by means of external manual control, connected to a storage oscilloscope measuring motor speed input signal. A 2 litre capacity reservoir was connected in series to the ADU discharge reservoir in order to dampen pulsating discharge pressure occurring at low compressor speed, identified during previous steady state testing. This additional capacitance should not influence the compressor dynamic response since there is no downstream resistance experienced. Air flow was measured by hot wire anemometer, configured to respond within 2 ms, the output signal of which is recorded by storage oscilloscope.

The experimental procedure consisted of operating the compressor at a steady speed whilst the air mass flow output was measured by the hot wire anemometer. A change in compressor speed, initiated by manual rotation of the speed control setting, produced an air flow response.

Table 5.2 Detail of equipment used in ADU dynamic test.

Equipment	Identification
TSI Hot Wire Anemometer	TSI 4050 34221
Pressure Gauge	0 – 100 kPa Aschroft 8437
Storage Oscilloscope	TDS 3040 B013155

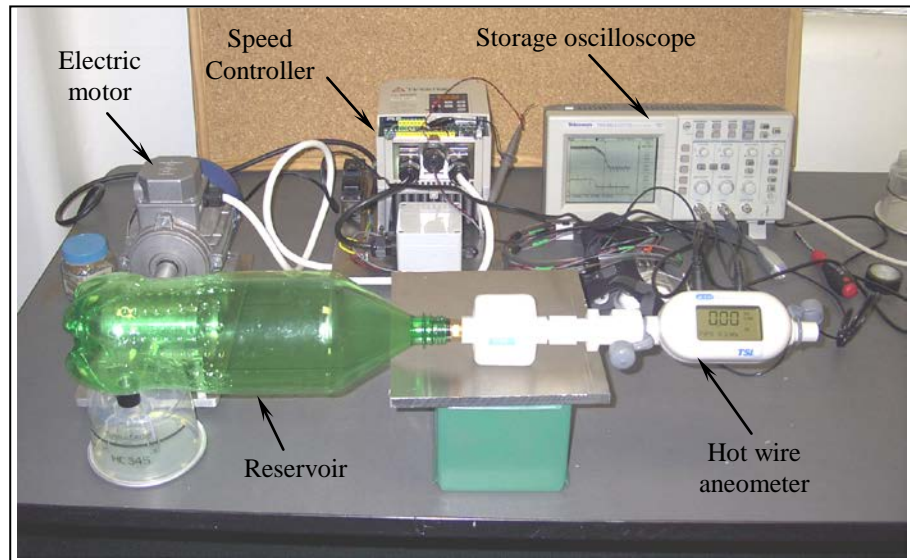


Figure 5.6 Photo of ADU dynamic test setup.

5.4.2 Results

A typical result of dynamic testing of the ADU, shown by Figure 5.7, indicates that increasing compressor speed from 300 rev/min to 1100 rev/min provides a corresponding increase in air mass flow from 0.45 g/s up to 1.4 g/s. It is noted that the compressor speed signal contains noise, seen as random spikes, however, this does not distract from the measured value.

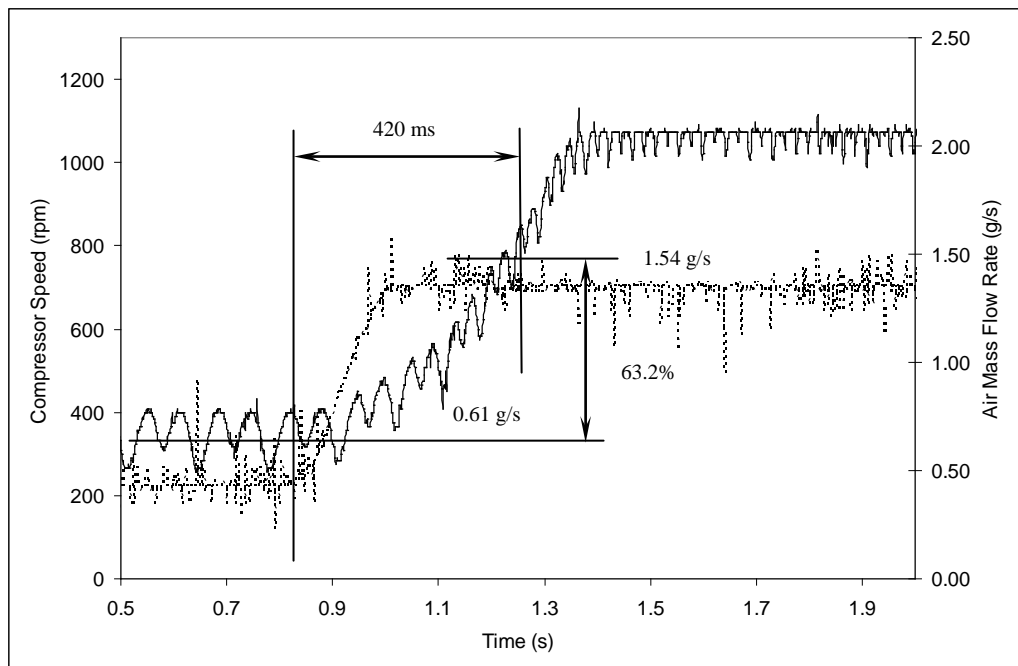


Figure 5.7 Dynamic response of ADU; --- .compressor speed signal, — compressor air mass flow response.

Manual actuation of the potentiometer controlling compressor speed could not achieve a perfect step input, rather, the input speed signal closely resembles a terminated ramp, however, several tests involving these types of inputs, Appendix E, were conducted on the ADU and all gave a similar response.

Oscillations in compressor air output massflow was recorded in all tests despite the damping effect provided by the additional reservoir, however, this effect can be seen to reduce as the compressor increases speed. This characteristic, typical of a diaphragm compressor, has been minimised by offsetting the phasing of diaphragm air discharge. Furthermore, the pressure attenuation of the small diameter air transmission tube utilised within the prototype system will eliminate this effect from being experienced at the mask.

For the purpose of predicting the ADU model element, it is assumed the completed prototype ADU has a first order system behaviour of time constant 420 ms.

5.5 Completion of Prototype system

In this section the system mask pressure transducer is selected and interfaced with the ADU, completing the prototype breathing system.

5.5.1 Pressure Transducer Selection

The prototype breathing system requires compressor speed to be regulated by a controller acting on the nasal mask pressure feedback signal. Selection of the mask pressure sensor is based on the following criteria:

- Accuracy over the low operating pressure range of 0 – 20 cm Wg being measured.
- Speed of response within 20 ms.
- Small size suitable for mask mounting.
- Low cost.
- Compensation for changing air pressure and temperature.

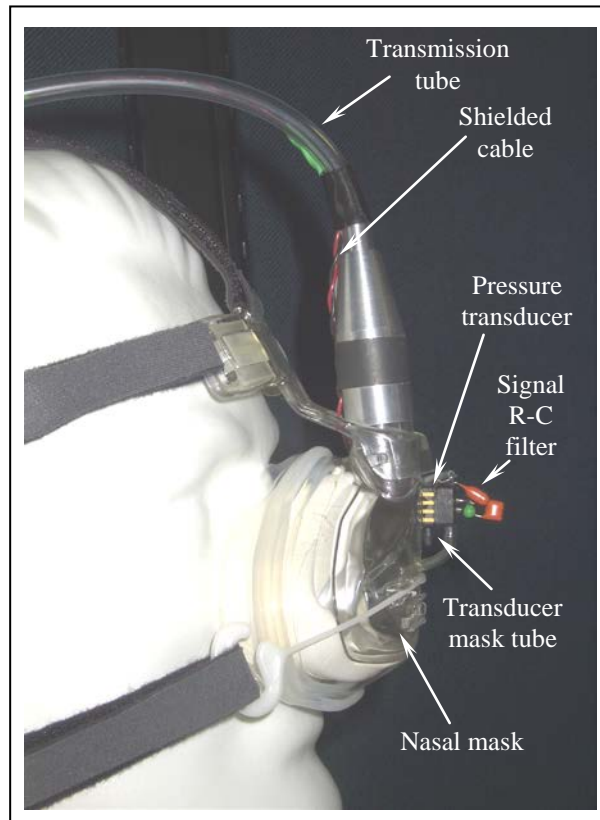


Figure 5.8 Pressure transducer mounted on nasal mask.

After an exhaustive search, both from local and international suppliers, a MOTOROLA piezoresistive monolithic silicon pressure sensor, was found to meet all of the desired criteria, Appendix F1.

Manufacturer's specifications, Appendix F2, show this sensor is capable of reading pressures of up to 40 cm Wg, to an accuracy of ± 0.6 cm Wg, with an output sensitivity of 98 mV/cm Wg. It would have been desirable to have sourced a pressure transducer with greater sensitivity over the mask air pressure range, however, none could be found. This transducer is located as close as possible to the nasal mask, Figure 5.8, to minimise any measurement time delays.

As suggested by the manufacturer, shielded cabling is utilised to avoid excessive signal noise and power supply decoupling and output filtering is achieved through the addition of R-C low pass filter, specifications given in Appendix F3.

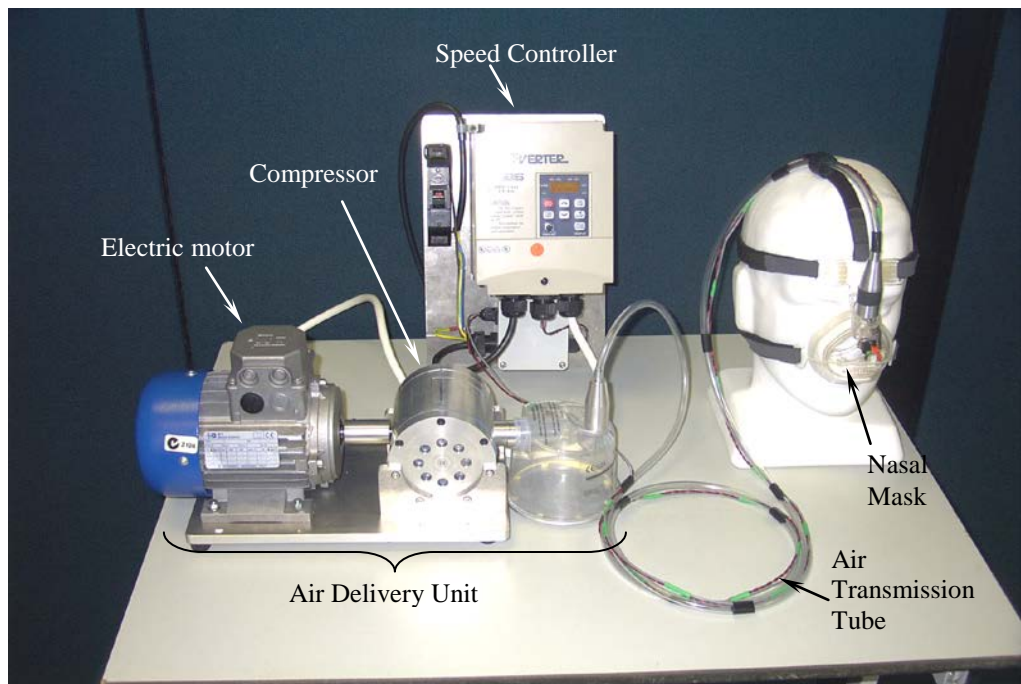


Figure 5.9 Completed prototype I-CPAP breathing system.

5.5.2 Final Assembly

The completed prototype breathing system, Figure 5.9, utilises a small, 5.5 mm internal diameter flexible PVC tube, 1.8 metres long, to transmit air from the ADU reservoir to the patient's nasal mask. Electrical cabling leading to the mask pressure sensor is taped to the air transmission tube to prevent entanglement with the patient.

5.6 Characterisation of Model Simulation

Within this section, characterisation of both the ADU and nasal mask elements within the simulation is undertaken, completing the model simulation and determining the suitability of the ADU to meet the prototype system dynamic air requirements.

5.6.1 Air Delivery Unit

Characterisation of the model simulation ADU element involves replacement of the idealised zero order behaviour previously used with a first order transfer function, with provision also being made for the time constant (T_d), in milliseconds, to be manually input into the model simulation, Figure 5.10.

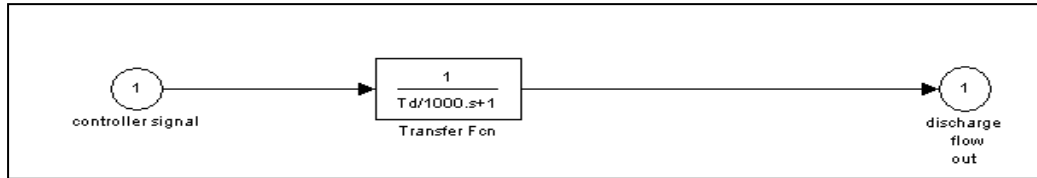


Figure 5.10 Characterised ADU element within model simulation.

5.6.2 Mask Pressure Transducer

Due to the absence of any dynamic response information on the mask pressure transducer, this device is considered to have zero order linear response, with output equal to input.

5.7 Model Simulation Dynamic Testing

Within this section, the complete characterised model simulation is tested under the dynamic patient breathing load.

5.7.1 Simulation Configuration

The SIMULINK model is configured in accordance with the prototype breathing system physical characteristics and air properties, Table 3.3, with the inclusion of the ADU time constant of 420 ms, and set to operate at a desired mask pressure of 19 cm Wg.

5.7.2 Simulation Results

The model simulation has produced a mask pressure within the desired tolerance of ± 0.5 cm Wg, Figure 5.11, utilising controller settings given in Table 5.3. This confirms that the prototype ADU does satisfy the breathing system air requirements. During patient inhalation, the mask pressure drops slightly, triggering an increase in air delivery from the ADU, however, when the patient exhales, the mask pressure slightly overshoots the set point before a reduction in air delivery occurs.

Table 5.3 Controller settings predicted by model simulation.

Controller Domain	Model Simulation
Proportional Action	30
Integral Time (s)	0.1
Derivative Time (s)	1

Increasing the ADU controller proportional action reduces the mask pressure fluctuation around the set point, however; the minimum controller settings required to achieve the desired mask pressure tolerance range are given.

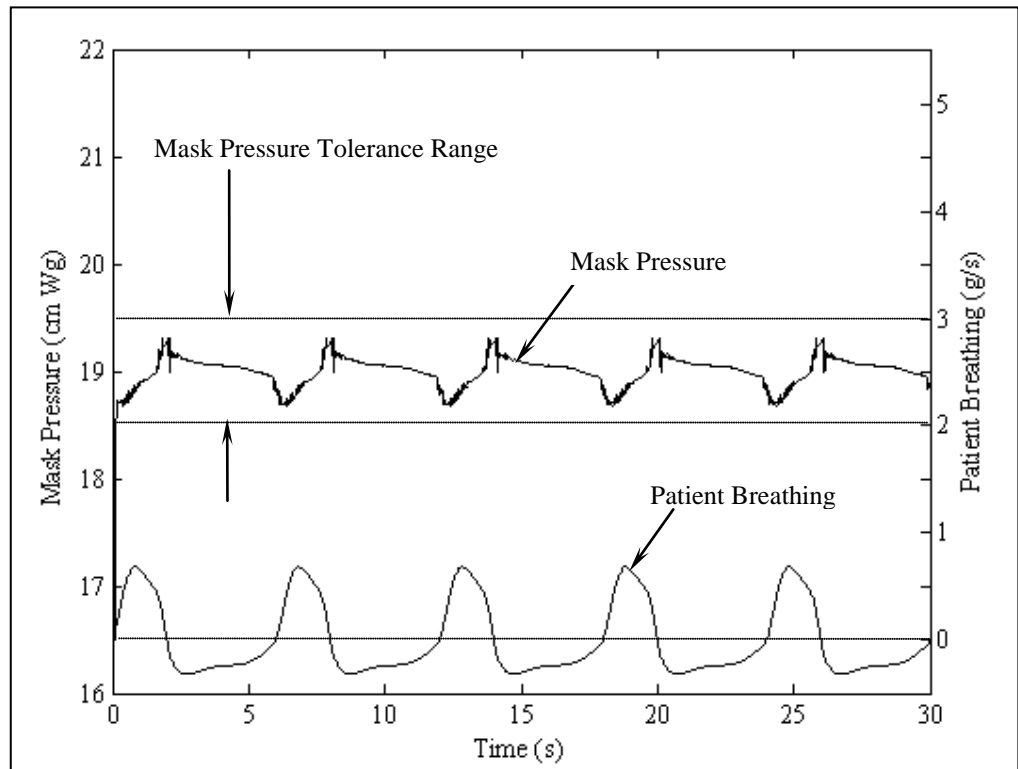


Figure 5.11 Model simulation mask pressure under simulated patient breathing load.

5.8 ADU Implementation within Prototype

Within this section, the performance of the ADU operating within the completed prototype breathing system is assessed.

5.8.1 Test Setup

A patient breathing simulator, Figure 5.12, was used to achieve a controlled load on the prototype system. The simulator consisted of a 7 litre lung syringe, driven by a linear actuator utilising positional feedback and computer controlled to continually read the same patient breath simulation text file, *breath.txt*, as that used by the model simulation. Tidal volume of the breathing simulator was calibrated to the patient model simulation load by measuring the volume of water displaced in a transparent sealed split level measuring unit.

During testing, a continuous dynamic measurement of simulated patient air mass flow rate was made by inserting the TSI hot wire flow anemometer in series with the air flow from the lung syringe, Figure 5.13.

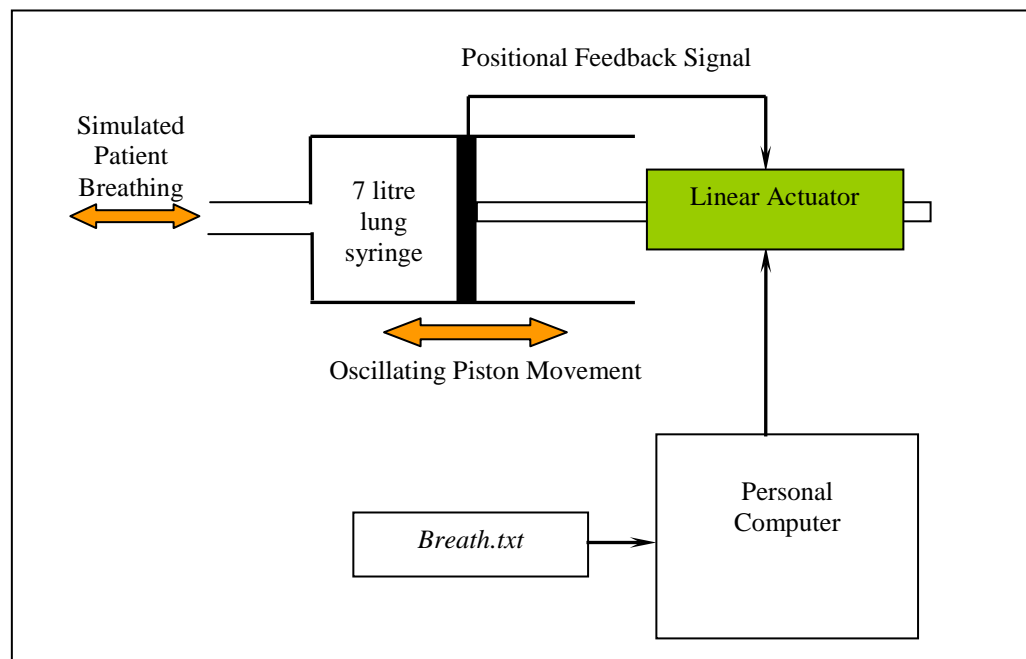


Figure 5.12 Schematic representation of patient breathing simulator.

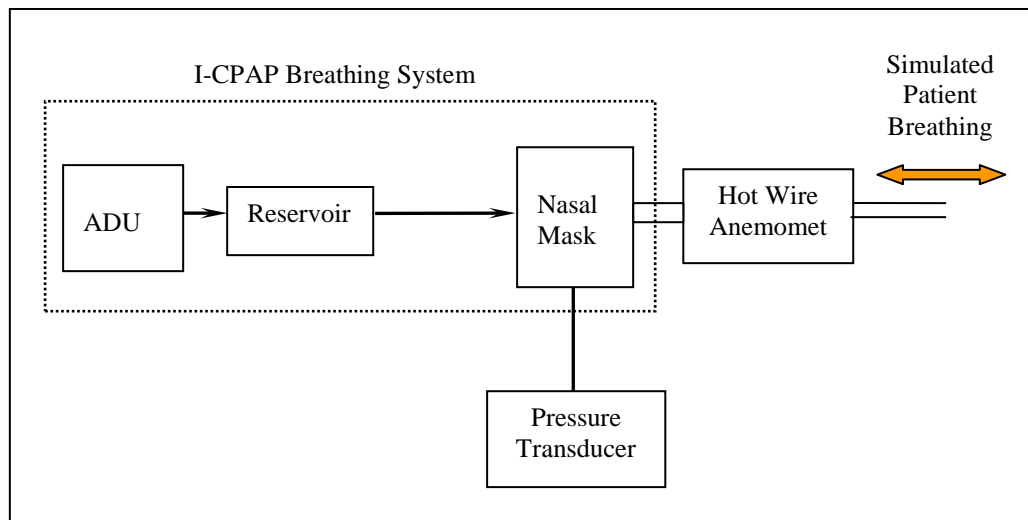


Figure 5.13 Schematic representation of simulated patient test setup.

A moulded plastic adult head provided an ideal means to mount the nasal mask and was fed air from the patient simulator through a hole cut into its nose, into which a plastic pipe had been glued, Figure 5.14. Nasal mask pressure was recorded by a pressure transducer, connected to a small tube inserted in the patient's nose. Details of measurement equipment used are given in Table 5.4.

The prototype system was tested whilst both nasal mask pressure and simulated patient breathing air mass flow rates were recorded.

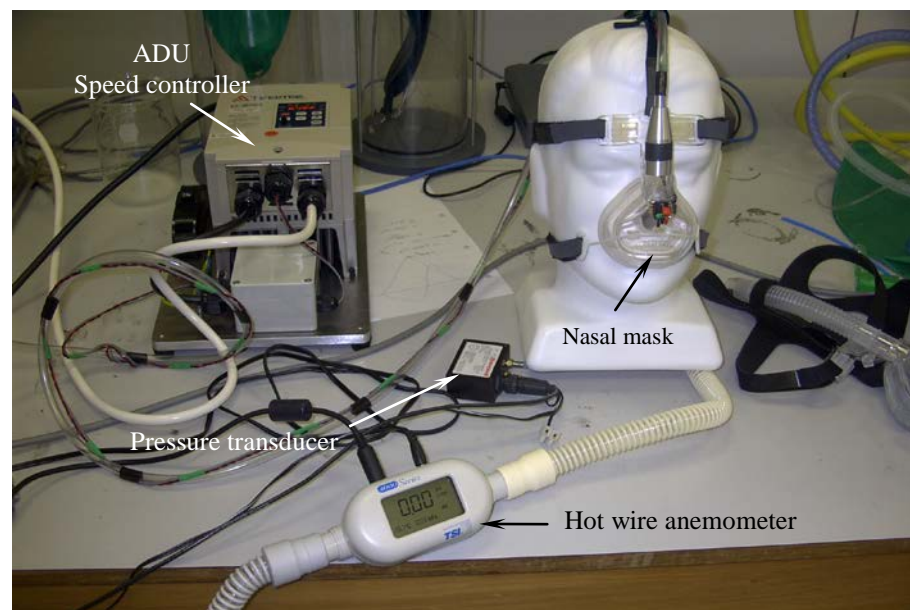


Figure 5.14 Patient simulation test setup.

Table 5.4 Details of equipment used in test.

Equipment	Marking
Hot Wire Anemometer	TSI
Precision Pressure Transducer	Honeywell
Lung Syringe	Hans Rudolph, inc. Unmarked
Lung Tidal Volume	Calibration Box Unmarked

5.8.2 Results

Although the intention of the speed controller was to solely regulate compressor speed in response to mask pressure, it became apparent during testing of the prototype, Figure 5.15, that the ADU controller gain setting was limited by instability occurring within the system. Exhaustive variations in controller settings were trialed; however, it was not possible to raise the proportional gain to a level where the prototype system mask pressure came within the desired tolerance range. The inability of the prototype system to achieve the controller proportional gain settings, predicted necessary by model simulation, suggests that the ADU controller is unable to regulate compressor speed in response to the mask pressure feedback signal. Comparison between model simulation and prototype breathing system controller settings achieved is shown above in Table 5.5.

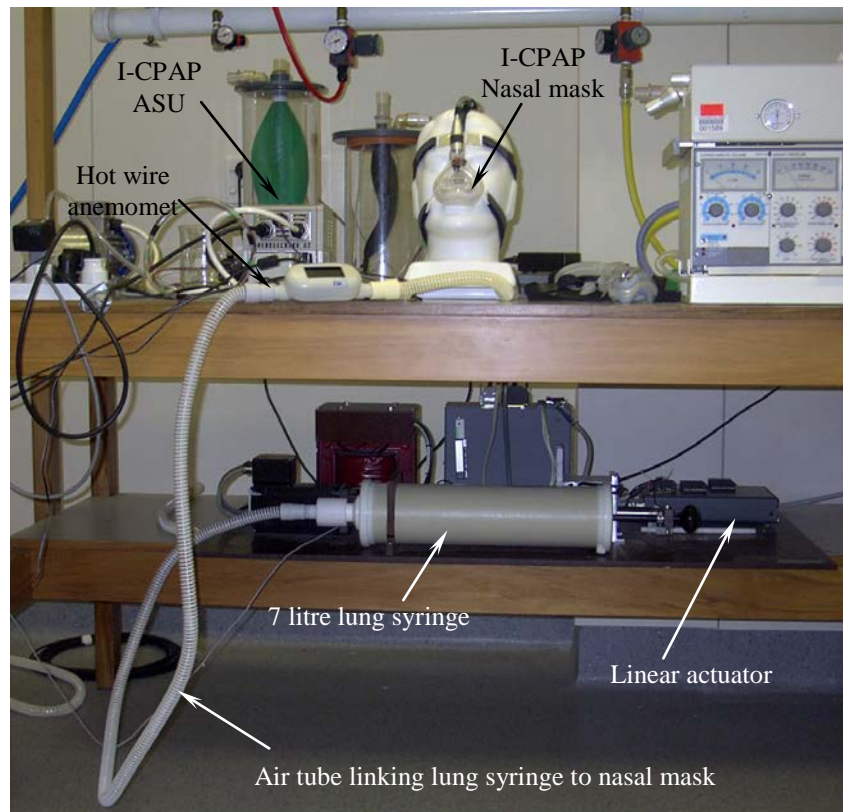


Figure 5.15 Patient breathing simulator connected to prototype system.

Table 5.5 Variation in prototype and model simulation controller settings.

Controller Domain	Prototype Breathing System	Model Simulation	Variation (%)
Proportional Action	10	30	300
Integral Time (s)	0.1	0.1	0
Derivative Time (s)	4.5	2	225

Figure 5.16 shows the results of the prototype system as well as the model simulation with both configured to use the same controller settings achieved during prototype testing, Table 5.5. It is indicated that the level of pressure required by the system is achievable, however, is not controllable due to the fact that this system needs an appropriate control scheme which is beyond the scope of this work.

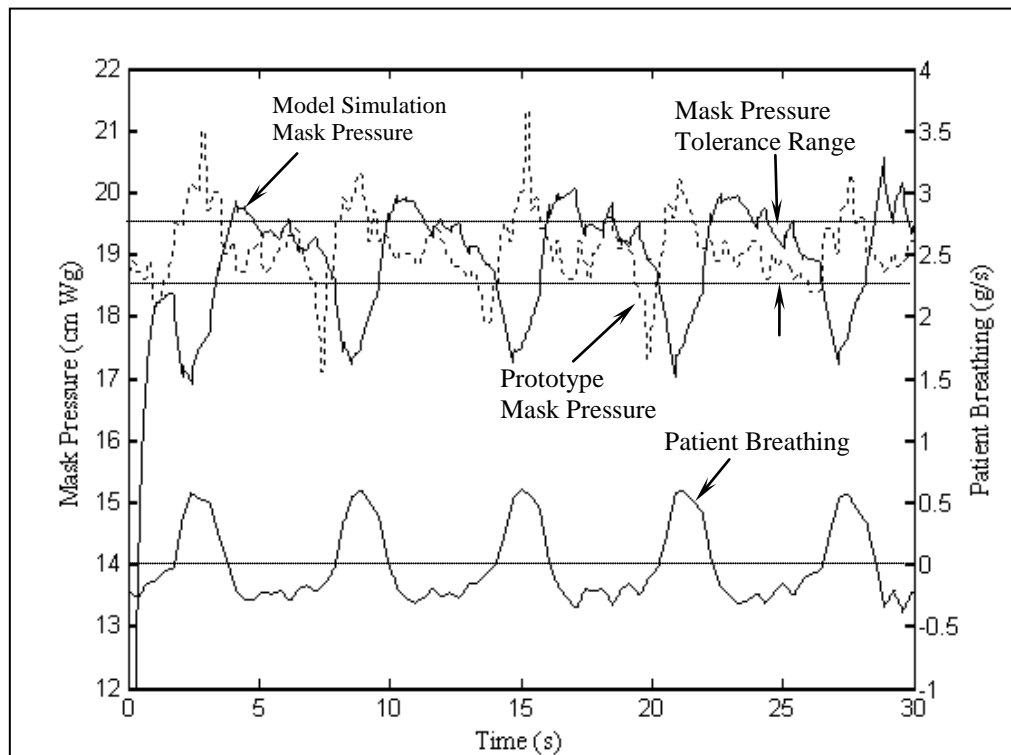


Figure 5.16 Comparison between prototype and model simulation mask pressures utilising lower controller gain setting.

An observation, from Figure 5.16, was made of fluctuation in simulated patient breathing air mass flow, occurring during the exhalation phase. This effect was noted during testing as minor sticking of the lung syringe producing a jerking motion in the linear actuator. Although it could not be eliminated from the test simulator, it is thought that this characteristic was not responsible for the prototype system mask pressure exceeding the pressure tolerance range, it simply modified the patient breathing load, characterising the mask pressure response.

5.9 Conclusions

A variable speed double diaphragm compressor has been designed and built to meet the prototype breathing system air requirements, identified by the system model, and has been proven, under both steady state and dynamic tests, to meet the system requirements. The compressor, contained within the prototype system ADU, produces the air pressure and mass flow output required by the prototype breathing system, however, the development of an appropriate mask pressure control scheme is required to maintain this parameter within the desired tolerance range which is beyond the scope of this research.

This thesis has accomplished the goals set out in the first chapter and has provided both a direction and resource for future work. The research has proven the feasibility of implementing a double diaphragm air compressor within the ADU of an I-CPAP breathing system, to supply air to a patient undergoing OSA therapy. Specifically, this work has:

- a) Developed an I-CPAP breathing system model and simulation, based on prototype component parameters.
- b) Proven the model simulation to be capable of accurately predicting both the steady state and dynamic behaviour of the breathing system.
- c) Utilised the model simulation to determine the air requirements of the prototype breathing system.

- d) Researched, designed and produced a variable speed air compressor capable of meeting the requirements identified by system modelling.
- e) Produced compressor performance and calibration charts through a process of steady and dynamic testing.
- f) Implemented the air compressor within the ADU element of a prototype breathing system.
- g) Conducted testing of the prototype breathing system and concluded the compressor and ADU meet the requirements of the I-CPAP system, despite limitations found in the speed control scheme.

5.10 Further Research

Having proven the feasibility of implementing a variable speed double diaphragm compressor within the I-CPAP system, there are many possible areas in which improvements can be made, including:

- a) Developing an improved mask pressure control scheme to enable the existing prototype system to meet its design goal of mask pressure tolerance.
- b) Design of an improved air compressor within the ADU, not limited to machining resources and available materials, which is quiet, compact and offers a smooth air pressure output. Possibilities include screw and rotor type compressors, operating at constant speed, utilising variable air flow control.
- c) Changes to nasal mask design to improve the air flow characteristics of the vent air flow. These could include the use of valves to control airflow both into and vented from the mask.
- d) Improvement in nasal mask pressure transducer type and location to keep the mask as robust as possible whilst addressing issues of hygiene and signal time delay.

These brief statements are provided merely as a guide to future work, any work to further develop the I-CPAP breathing system will likely be undertaken with regards to the commercial application of the system.

Appendix A Air Transmission Tube

Introduction

Within this appendix, the physical characteristics of the 5.5 mm flexible air transmission tube required by model simulation, but not presented within the main chapters, is given.

Appendix A1 Tube Air flow Resistance

Tube air flow resistance in terms of air flow velocity is given in Figure A1 below.

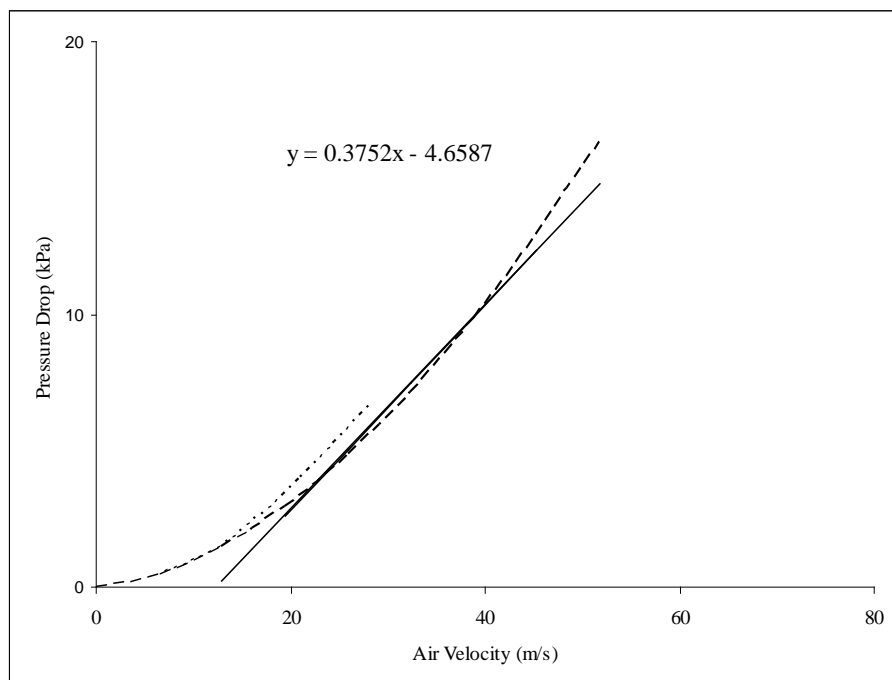


Figure A1 5.5 mm internal diameter, airflow pressure drop; — measured, - - - predicted, . . . linear model.

Appendix A2 PVC Tube Properties

The physical properties of flexible PVC tube used for air transmission within the prototype system is given below in Table A1.

Table A1 Properties of flexible PVC tube [34].

Density	1.31 g/cc
Ultimate Tensile Strength	13.2 MPa
Yield Tensile Strength	5.5 MPa
Hardness, Shore A	74.9
Hardness, Shore D	55.2
Tensile Modulus	7.6 MPa
Elongation at Break	310%
Brittleness Temperature	-60 - -3°C
Flammability, UL94	HB
Oxygen Index	31%
Haze	3 - 5%
Linear Mould Shrinkage	0.0025 – 0.03 cm/cm
Processing Temperature	165 – 185°C
Transmission, Visible	80.7%

Appendix B Air Supply Options

Introduction

This section supplements the summary contained within Chapter 4 by presenting additional material on which the selection of compressor type is based.

B1 Non-Positive Type Air Compressors

Conventional CPAP devices, such as the Fisher & Paykel HC220, commonly utilise centrifugal fan units to generate air pressures much lower than that required by the prototype system, however, the option of enlarging this fan unit from 50 mm to 130 mm diameter to achieve the higher air pressure required by the prototype system needs investigation. Calculations, based on idealised fan equation [31], predict the behaviour of the enlarged, Figure B1, when operating at a rotational speed of 12,000 rpm, when utilising the same blade geometry as the existing HC 220 fan rotor.

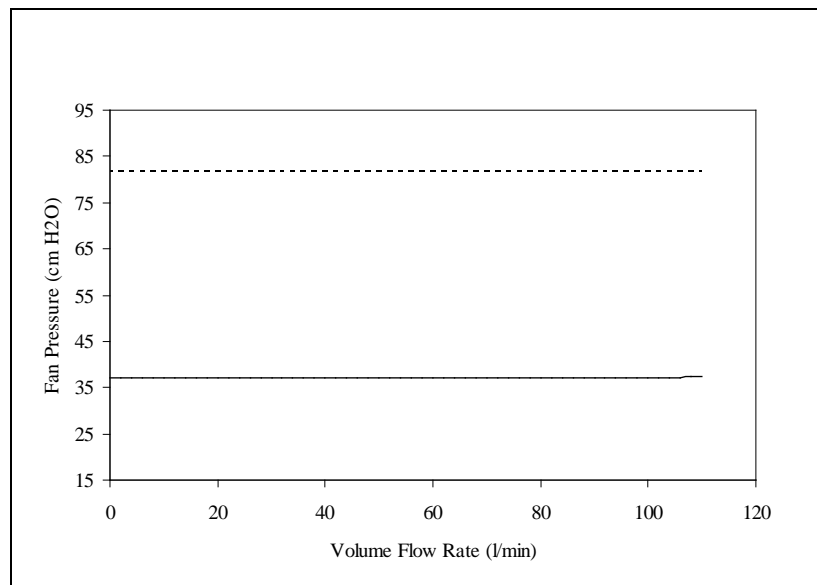


Figure B1 Fan air output characteristics —. CPAP fan operating at 21,000 rpm, -- enlarged 130 mm diameter fan operating at 12,000 rpm.

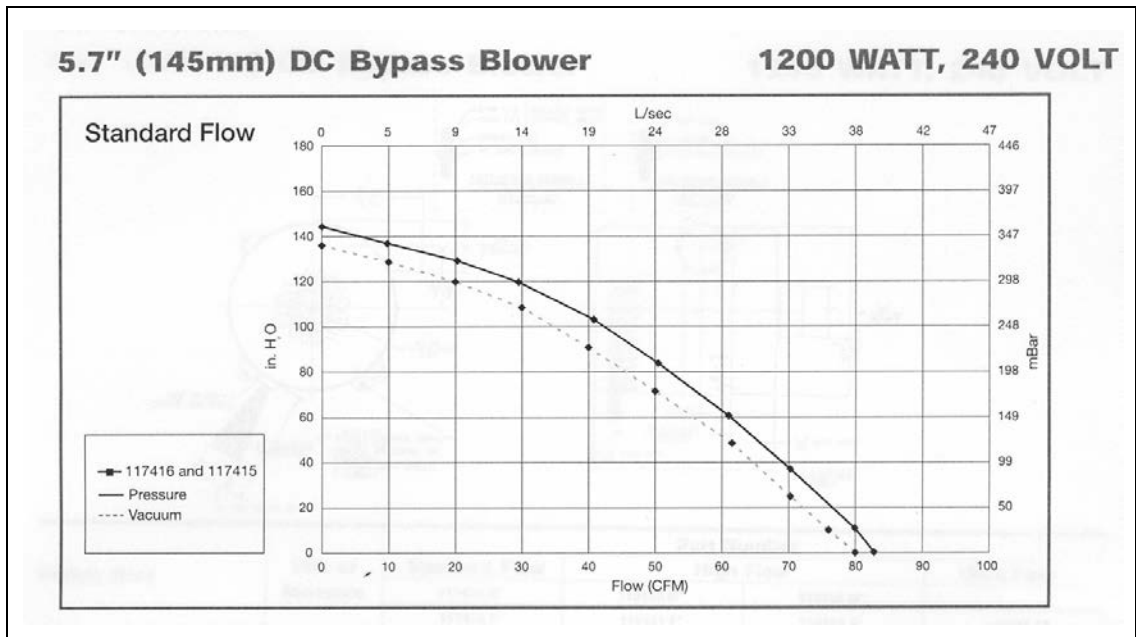


Figure B2 Commercial centrifugal fan performance curve [56].

This air pressure is well below the maximum air output pressure required by the prototype system and no consideration has been given to the mechanical forces and stresses within the enlarged fan rotor assembly.

Figure B2 shows the performance characteristics of a commercially available centrifugal fan unit that meets the requirements of the prototype system. This fan unit will supply an air volume flow rate that is well in excess of the 100 litres/min (3.5 SCFM) required by the I-CPAP system, however, it would additionally require some means by which the mass flow rate could be dynamically controlled. There is no data available on either the response of the fan unit to regulated air pressure or mass flow control. A possible alternative to the centrifugal fan is the regenerative blower, Figures B3 and B4, [38].

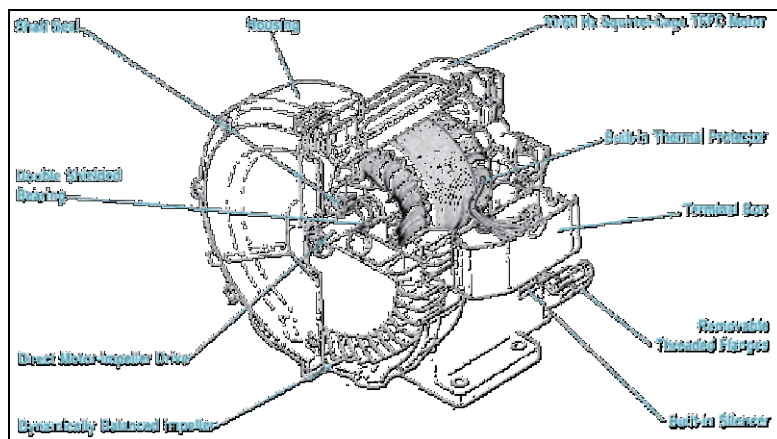


Figure B3 Pictorial view of regenerative fan [39].

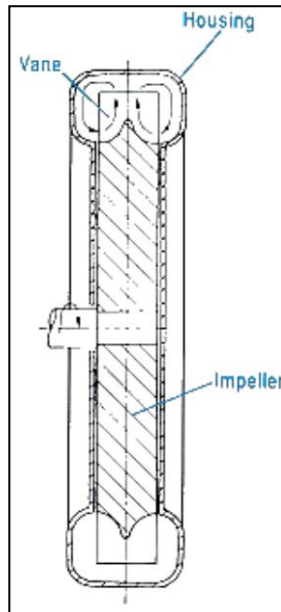


Figure B4 Sectional view of regenerative fan [39].

The higher air pressure, of up to 350 cm H₂O is achieved by redirecting the air leaving the rotor back into the successive spaces between the rotor blades, resulting in the flow following a vortex pattern. The air flowing within one revolution of the rotor will have been passed through the rotor several times, effectively increasing the air pressure for each cycle through the impeller. This flow cycling effectively results in multistage compression of the air. Regenerative blowers are most efficient when run in the middle of their operating range and efficiency drops off when operating at maximum or minimum airflows [39]. Because of this characteristic, manufacturers avoid showing the fan performance characteristics for low air mass flow rates, Figure B5. Due to the complex nature of both the airflow pattern and rotor/stator geometry, Figure B4, the prediction of the fan performance characteristics becomes a very complex and arduous exercise. A literature survey failed to produce any detailed information on predicting performance characteristics of these types of fans however basic descriptions on operating principles were found [39].

Commercially available regenerative fan units can supply an air volume flow rate well in excess of the 100 litres/min (3.5 SCFM), Figure B5, required by the prototype system, however, they also require some means by which the mass flow rate could be dynamically controlled. Because there is no data available on the pressure or mass flow response of either the centrifugal or regenerative fan units they are not considered suitable for implementation within the prototype system.

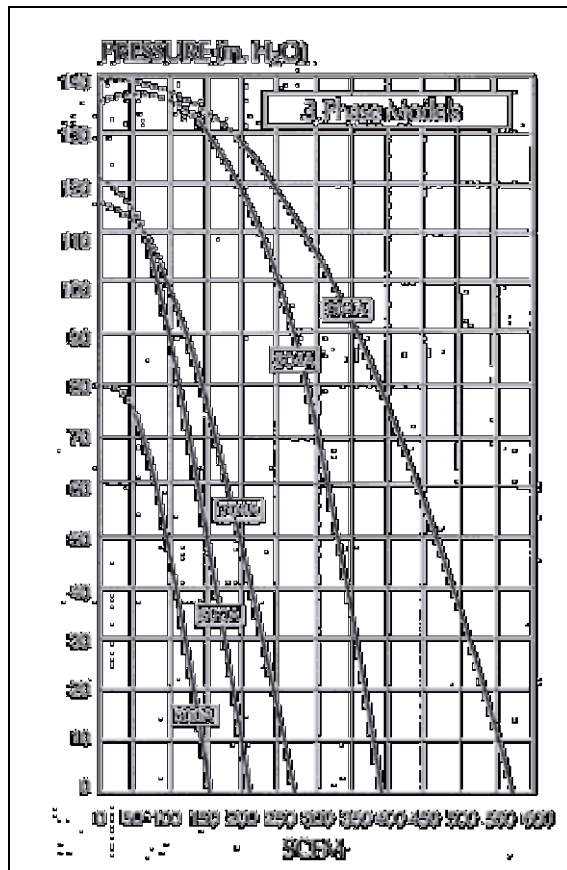


Figure B5 Regenerative fan performance graph [39].

B2 Positive Type Air Compressors

Positive displacement compressors, such as reciprocating and rocking piston, rotary vane, rotary screw and lobed rotor can achieve very high air pressures and mass flow rates, without the need for high operational speeds, however, a significant problem encountered in most of these types of compressors is the likely contamination of the breathing air through oil or carbon particles since most require some form of lubrication or liquid seal.

Diaphragm air compressors, Figure B6, avoid the problem of air contamination found in other types of positive displacement compressors, by utilising a thin elastic diaphragm to isolate the air flow from the operational mechanism.

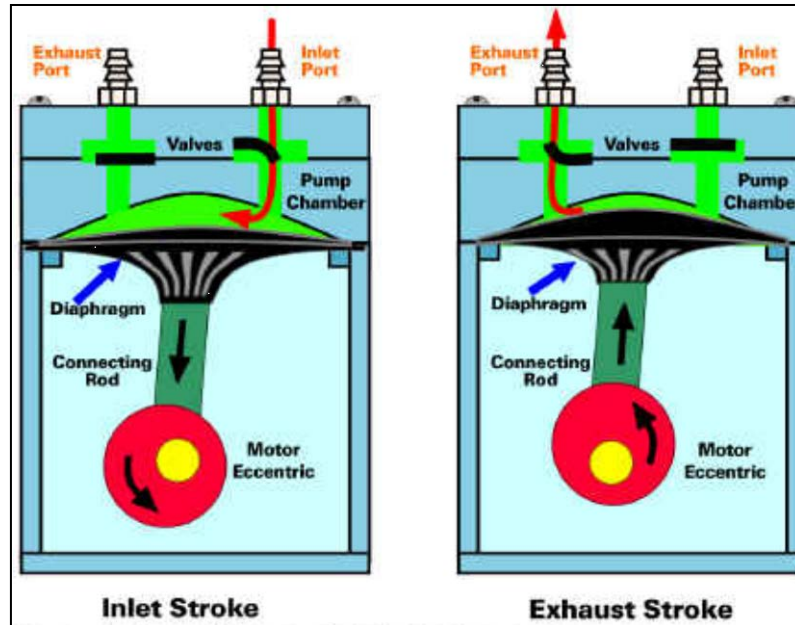


Figure B6 Schematic of diaphragm compressor operation [57].

The main disadvantage of a diaphragm air compressor is the cyclic operation creating pressure pulsations within the discharge airflow, however, this effect can be minimised through the use of multiple diaphragms or the use of stepper motor drives [58]. Tradition constant speed single diaphragm compressor output is characterised as approximately a square-wave form similar to that found in solenoid or linear magnetic drive powered pumps. Commercial diaphragm compressors are available that utilise stepper motor drive units where less than 1% of the airflow time is lost during the suction cycle due to a technique called sine-wave compensation [58]. This method utilises stepper motor position-feedback control where each revolution is made up from very small steps in angular change enabling speed changes to be made within one revolution. The pulsation of discharge air can also be reduced through the use of multiple diaphragms operating from a single eccentric shaft. Both of these techniques are used to produce near pulse-less discharge air flow.

There are many commercially available diaphragm compressor design options that range from micro-pumps flowing 0.45 litre/min through to high capacity compressors capable of displacing 280 litres/min [57]. A commercially available two-stage diaphragm air compressor, Figure B7, capable of providing 150 litre/min at an air flow at a pressure of 210 kPa, is suited for application within in the prototype system.



Figure B7 Two-stage stepper motor driven diaphragm air compressor [57].

B3 Regulated Air Supply

Air supply valve and pressure regulator are reviewed as a potential means of providing a functional ADU for the prototype system, however, it does not address the requirements of being portable. This option simply serves as a means to quickly implement an operational prototype system.

Two regulating schemes, control of air mass flow and the control of air pressure into the prototype system reservoir are considered:

1. Various electro-mechanical and piezoelectric actuated valves are commercially available to regulate air mass flow within the prototype system [59]. It is likely, however, that difficulty will be encountered due to the continual changes in pressure difference experienced across such a device. This problem could be overcome by controlling this valve through the use of a secondary control system that measures the air mass flow into the reservoir and that itself has a set point determined by the primary controller reacting to the sensed mask pressure. This form of air supply regulation would contribute significantly to the complexity in controlling the prototype system.
2. A simpler alternative would be the use of a signal actuated pressure regulator to supply air to the prototype system reservoir, controlled by the signal from the mask pressure transducer [60]. This method of air supply has already been implemented within the I-CPAP system, during early testing at Fisher & Paykel

Healthcare, however, the unfavourable dynamic characteristics of the pressure regulation valve resulted in uncontrolled pulsing of mask pressure. Investigation revealed the specifications for the FESTO precision proportional pressure regulator stated a valve hysteresis value of 30 cm Wg, representing 16% of the required dynamic range required by the prototype system. No specification was given for maximum air mass flow rate and sensitivity of the device. The electronically controlled proportional pressure-regulating valve with piezoelectric pilot actuation offers greater sensitivity with less hysteresis than the electro-mechanical type pressure regulator [61]. This pressure regulator has hysteresis of 0.42 cm Wg and a maximum pressure output of 210 cm Wg, making it well suited to implementation within the prototype system.

Whilst flow control valves and pressure regulators are commercially available that could enable the system to operate these methods still require an air supply and are therefore unsuited for practical implementation in a portable system and are therefore eliminated from consideration.

Appendix C Compressor Actuation

Introduction

This section contains actuator performance information in support of selection made within Chapter 4.

C1 Direct Acting Solenoid

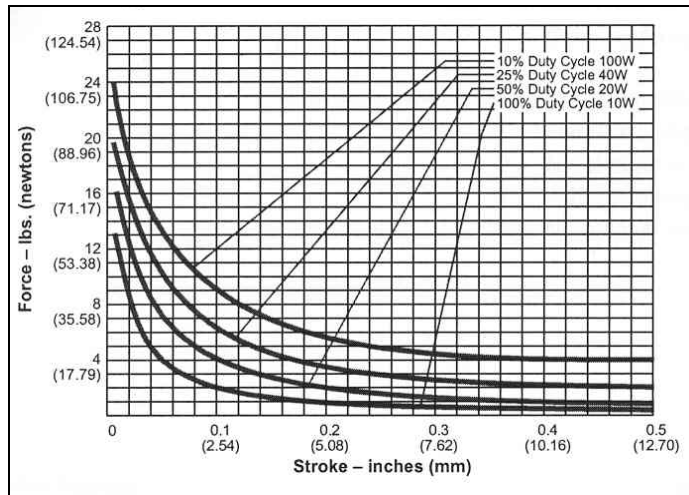


Figure C1 LEDEX STA 1" diameter x 2" direct acting solenoid performance specifications [62].

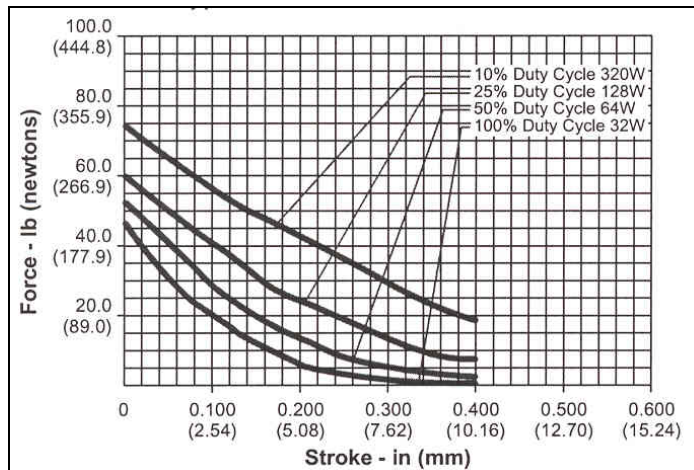


Figure C2 LEDEX 6EC Low Profile Solenoid performance graph [62].

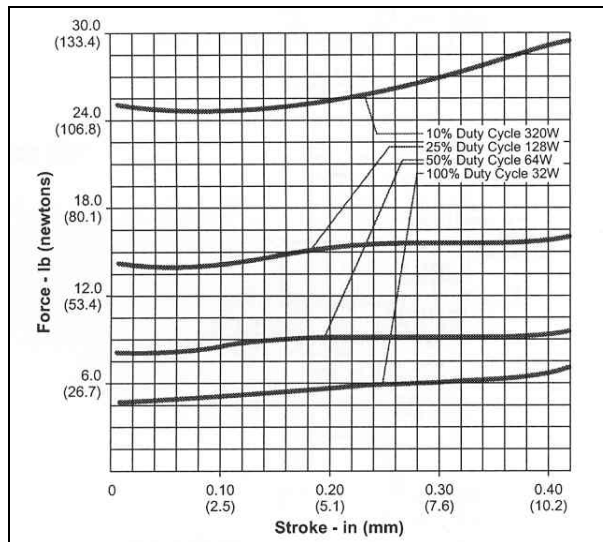


Figure C3 LEDEX soft-shift 6EP solenoid performance graph [62].

C2 Linear Motor

Table C1 Performance specifications for commercial linear servomotor [46].

Forcer Type	2504	2506	2508	2510	3804	3806	3808	3810	Units
Peak Force	624	936	958	959	1521	1521	1521	1522	N
Continuous Force	51	70	87	104	121	167	210	248	N
Peak Acceleration	297	312	312	288	327	334	282	243	m/s/s
Peak Velocity	14.5	9.7	7.3	5.9	6.4	4.2	3.1	2.5	m/s
Force Constant (sine Com.)	22	33	44	55	50	75	100	124	N/Arms
Back-emf Constant	18.0	27.0	36.0	45.0	40.0	61.0	81.3	101.6	Vpk/m/s
Electrical Time Constant	0.7	0.7	0.7	0.7	0.9	0.9	0.9	0.9	ms
Fundamental Motor Constant	6.2	7.6	8.8	9.8	11.8	14.4	16.7	18.6	N/√W
Continuous Working Voltage	320	320	320	320	320	320	320	320	V d.c.
Thrust Block Mass	1.05	1.50	2.00	2.45	2.15	3.15	4.15	5.15	Kg
Thrust Rod Mass/metre	3.5	3.5	3.5	3.5	8.3	8.3	8.3	8.3	Kg/m
Thrust Rod Diameter	25	25	25	25	38	38	38	38	mm
Forcer Length	121	174	225	276	167	238	309	380	mm

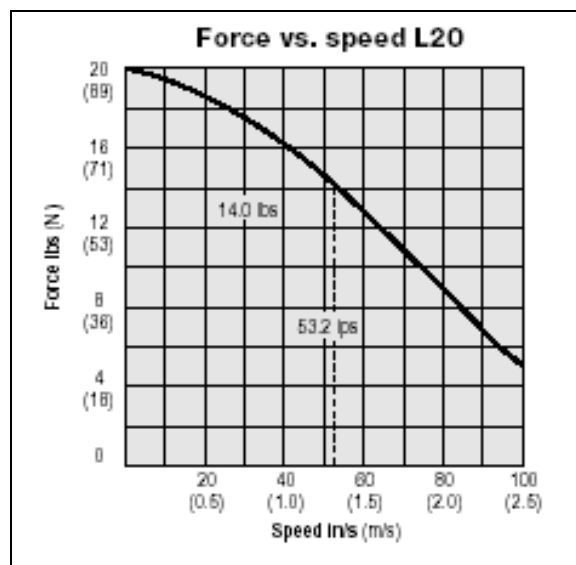


Figure C4 Performance characteristics for platen-type linear actuator [63].

C3 Rotary Solenoid

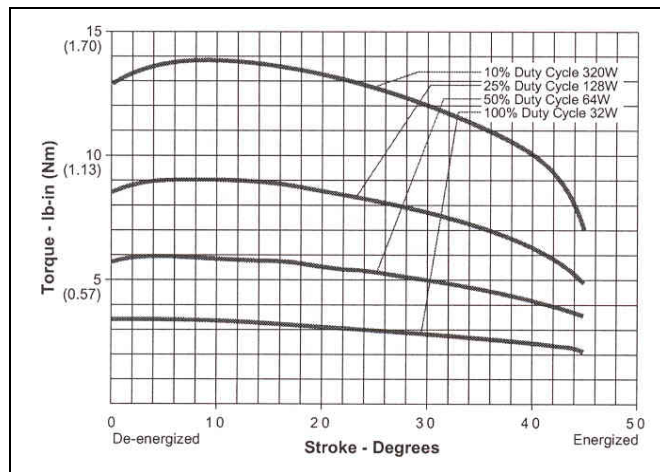


Figure C5 Torque characteristics of LEDEX 6EV BTA solenoid [48].

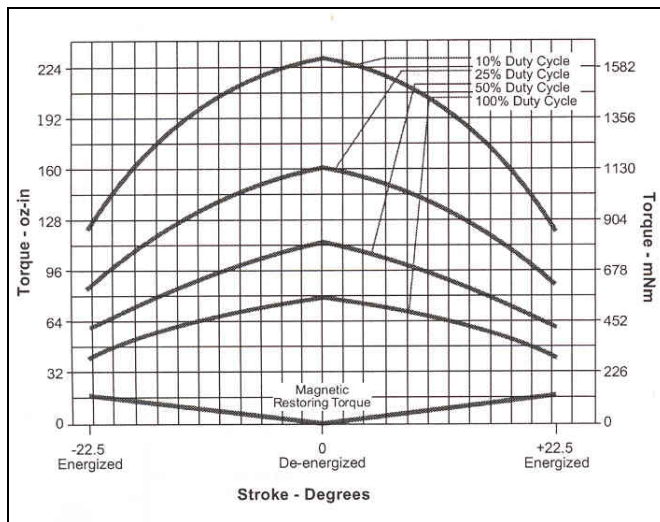


Figure C6 LEDEX Ultimag 6EM rotary solenoid torque output [49].

C4 Stepper Motor

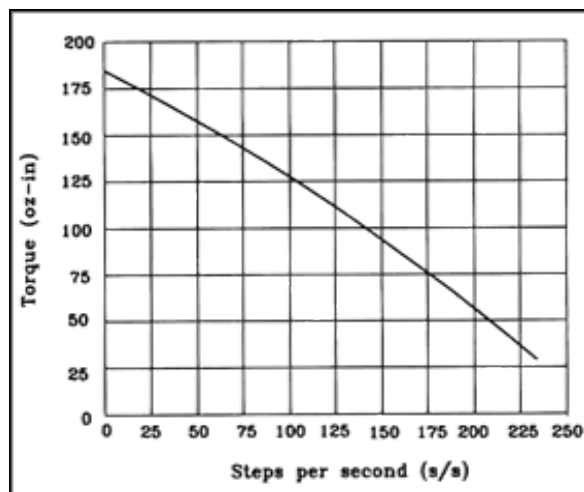


Figure C7 Typical torque output for hybrid stepper motor [64].

C5 Servomotor

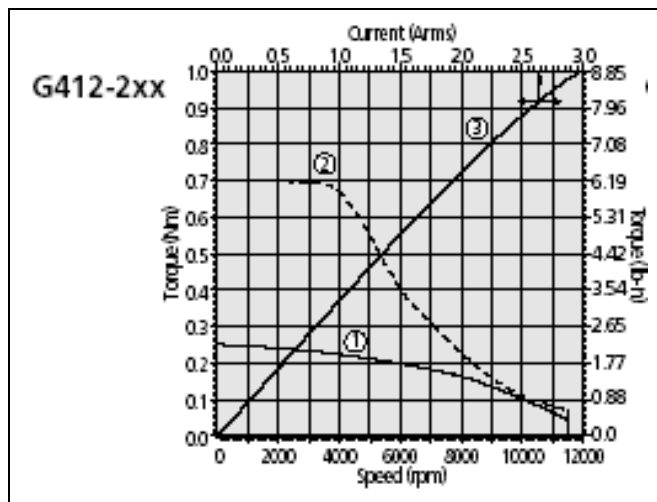


Figure C8 Moog model G412-2xx servomotor performance graph; 1 Continuous torque, 2 Peak torque, 3 Motor torque constant [65]

C6 Speed Controlled DC Motor

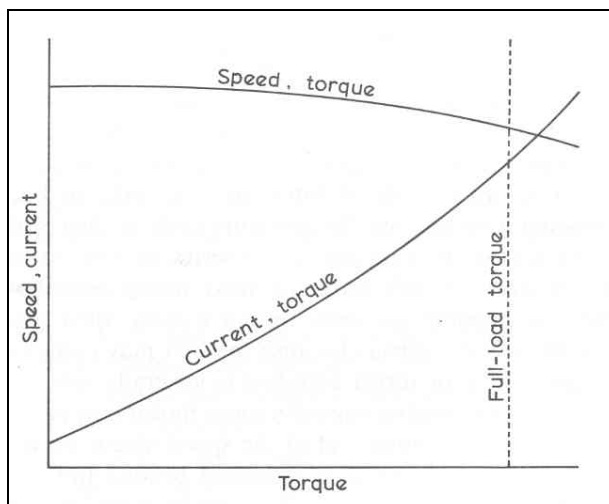


Figure C9 Shunt wound DC motor operating characteristics [52].

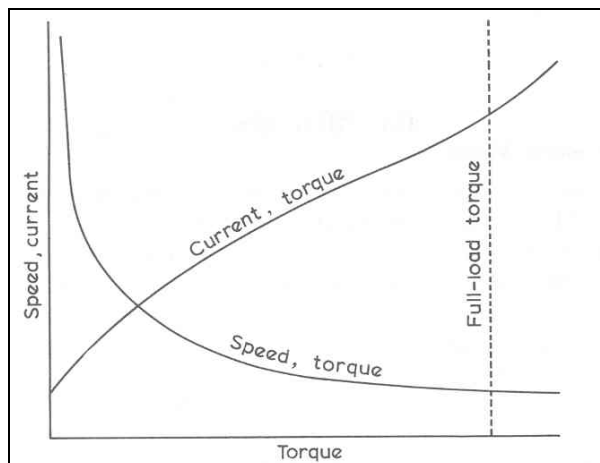


Figure C10 Series wound DC motor operating characteristics [52].

C7 Speed Controlled AC Motor

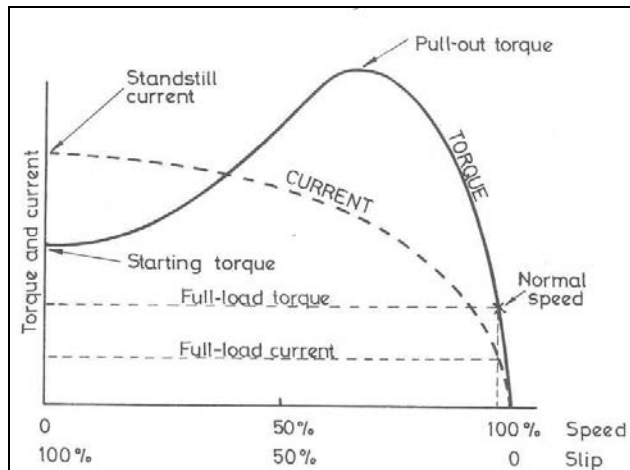


Figure C11 AC induction motor operating characteristics selected for compressor actuation [52].

C8 AC Induction Motor Specifications

This section contains motor manufacturers specifications, shown in Table C1.

Table C1 Compressor motor technical data [66].

11.0 DATI TECNICI		11.0 TECHNICAL DATA										11.0 TECHNISCHE DATEN		
MN XN		Motori monofase standard Standard single phase motors Standard Einphasenmotoren												
MF XF		Motori monofase autofrenanti standard Standard single phase brake motors Standard Einphasenbremsmotoren												
2 poli/pole/polig		3000 rpm												
Tipo Type Typ	kW	HP	n_{n-1} min ⁻¹	η %	cos ϕ	I_N (230V) A	I_{sp} I_N	M_N Nm	M_{sp} M_N	M_{MAX} M_N	C μ F	J Kg m^2	Kg (MN)	Kg (MF)
56 A	0.09	0.12	2740	54	0.90	0.85	2.4	0.28	0.58	1.4	6.3	0.00011	3	4.1
63 B	0.18	0.25	2750	54	0.92	1.5	2.5	0.62	0.62	1.6	8	0.00025	4.7	6.2
63 C	0.25	0.33	2750	56	0.94	2.2	2.5	0.65	0.66	1.6	10	0.00034	4.8	6.3
71 B	0.37	0.5	2780	60	0.94	3.2	3	1.28	0.70	1.8	12.5	0.00047	6.7	8.2
71 C	0.55	0.75	2800	64	0.96	4	3.5	1.9	0.70	1.8	16	0.00057	7.4	8.2
80 B	0.75	1	2820	70	0.96	5.5	3.5	2.5	0.74	1.8	20	0.00105	11	13.2
90 S	1.1	1.5	2830	70	0.98	8.5	3.6	3.8	0.76	1.9	30	0.00172	13.2	16.3
90 L	1.5	2	2830	74	0.98	11.5	3.6	5.1	0.76	1.9	35	0.00191	15.1	18.2
100 A	2.2	3	2830	76	0.98	16.8	4	7.4	0.70	1.9	60	0.00299	23	28.3
4 poli/pole/polig		1500 rpm												
Tipo Type Typ	kW	HP	n_{n-1} min ⁻¹	η %	cos ϕ	I_N (230V) A	I_{sp} I_N	M_N Nm	M_{sp} M_N	M_{MAX} M_N	C μ F	J Kg m^2	Kg (MN)	Kg (MF)
56 B	0.09	0.12	1340	54	0.90	0.95	1.6	0.65	0.90	1.4	6.3	0.00018	3.1	4.2
63 B	0.12	0.16	1370	58	0.90	1.2	2.5	0.84	0.74	1.6	6.3	0.00025	4.6	6.1
63 C	0.18	0.25	1370	58	0.92	1.6	2.5	1.3	0.78	1.6	8	0.00034	4.8	6.3
71 B	0.25	0.33	1380	58	0.94	2.3	2.5	1.8	0.78	1.6	14	0.00096	6.6	8.1
71 C	0.37	0.5	1380	58	0.94	3	2.8	2.5	0.82	1.6	16	0.00117	7.2	8.7
80 B	0.55	0.75	1400	62	0.94	4.2	3	3.7	0.75	1.8	20	0.00254	10.8	13
80C	0.75	1	1400	66	0.94	5.6	3	5.1	0.73	1.8	25	0.00285	11.8	14
80 D	0.88	1.2	1400	66	0.94	7	3	6	0.70	1.8	30	0.00316	12.3	14
90 S	1.1	1.5	1410	68	0.96	8.5	3.2	7.5	0.70	1.8	30	0.00320	12.9	16.0
90 L	1.5	2	1410	68	0.96	9.3	3.2	10.2	0.65	1.8	35	0.00398	14.5	17.6
100 A	1.8	2.5	1420	70	0.96	12.5	3.2	12.1	0.60	1.8	40	0.00520	21	26.5
100 B	2.2	3	1420	70	0.96	15.0	3.2	14.8	0.60	1.8	50	0.00688	25	30.5

C9 Motor Speed Controller Specifications

Manufacturer's specifications for the electric motor speed controller are shown below in Table C2.

Table C2 Speed controller general specifications [67].

Item	V2 TYPE	
Control type	V/F & vector control; space-vector PWM modulation	
Frequency control	Range	V/F control: 0.0 ~ 400Hz Vector control: 3.5 magnification of motor rated frequency
	Accuracy	Digital: 0.01% (-10 ~ 40°C); analog: 0.4% (25±10°C)
	Setting resolution	Digital: 0.01 Hz (note 1); analog: 0.06 Hz/60 Hz
	Output resolution	0.01Hz
	Keypad setting	Set directly with ▲ ▼ keys or the VR on the keypad
	External signal setting	External variable resistor/ 0-5V/ 0-10V/ 4-20mA/ 5-0V/ 10-0V/ 20-4mA Performs up/down controls, speed control or automatic procedure control with multifunctional contacts on the terminal base (TM2) (see descriptions of P_52)
	Other functions	Respectively setting up upper/lower frequency limits, start frequency, and three-stage prohibited frequencies
General control	Carrier frequency	2 ~ 16 kHz
	Acc/dec control	Two-stage acc/dec time (0.1 – 3,600 seconds) and two-stage S curve (see descriptions on P_21)
	Torque control	Torque up level can be set
	Multifunctional analog output	5 functions (see description of P_72)
	Multifunctional input	16 functions (see description of P_52~54)
	Multifunctional output	7 functions (see description of P_75/76)
	Other functions	Auto voltage regulation (AVR), auto slip compensation, auto energy saving, deceleration stop, free run stop or spin stop, malfunction retry, auto DC brake, spin start or normal start, 3-wire running control, PID function.
Four-digit seven-section display and status indicators	Frequency/speed/line speed/DC voltage/output voltage/current/inverter direction/inverter parameters/error record/program version displays	
Communication control	1. Can be controlled through RS232 or RS485 2. One-to-one or one-to-many (RS485 only) control 3. Baud rate / stop bit / parity bit can be set	
Operation temperature	-10 ~ 40°C	
Humidity	0 ~ 95% relative humidity (non-condensed)	
Vibration	Below 0.5G	

Appendix D Design Details of Diaphragm Compressor

Introduction

Detailed information on compressor material specifications and manufacturing drawings, not included within the main chapters, is presented within these appendices.

D1 Reed Valve Material

Physical properties of the plastic film used within the compressor as the reed valve is given below in Table D1.

Table D1 KKPC Kuhmo GP 125H high transparency GPPS specifications [68].

Thickness	0.35 mm
Density	1.04 g/cc
Water Absorption	0.03%
Hardness, Rockwell M	75
Ultimate Tensile Strength	49.9 MPa
Elongation at Break	2.5%
Flexural Modulus	2.89 GPa
Flexural Yield Strength	89.3 MPa
Deflection Temperature at 1.8 MPa	87°C
Vicat Softening Point	105°C
Flammability, UL94	HB
Linear Mould Shrinkage	0.003 – 0.006 cm/cm
Melt Flow	1.5 g/10 min
Transmission, Visible	80%

D2 Nylon Gear–Crank Material

Physical properties of the nylon gear material used in the gear – crank actuator mechanism within the compressor is given below in Table D2.

Nylatron GS Nylon is a nylon and molybdenum disulphide (MoS₂) composition designed to meet the mechanical, thermal and bearing properties of type 6/6 nylon while maintaining its basic electrical and mechanical characteristics. The compounding of finely divided particles imparts extra lubricity into this nylon, permitting GS parts to operate with little or no lubrication.

Table D2 Nylatron® GS nylon, type 66, MoS₂ filled, specifications [69].

Specific Gravity	1.16
Tensile Strength	86 MPa
Tensile Modulus	3,310 MPa
Elongation	25%
Flexural Strength	117 MPa
Flexural Modulus	3,172 MPa
Compressive Strength	110 MPa
Compressive Modulus	2,896 MPa
Hardness Rockwell M	85
Hardness Rockwell R	115
Coefficient of Friction	0.2
Wear Factor (k)	76.2×10^{-3} mm/m·hr
Deflection Temperature	93°C
Melting Point (Crystalline)	260°C
Continuous Service in Air	104°C

D3 Diaphragm Material

Physical properties of the neoprene – nylon diaphragm materials used within the compressor is given below in Table D3.

Table D3 Neoprene nylon diaphragm material [70].

Thickness	0.4 mm
Width	1,550 mm
Colour	Blue
Nylon Cloth Base Weight	110 gm ²
Finish Weight	390 gm ² ± 10 gm ²
Operating Temperature	100 °C to -15°C
Tensile Strength	Good
Features	<ul style="list-style-type: none">• High strength to weight ratio.• High flexibility and crack resistance due to high elastomer content of over 70%.• Good resistance to most oils, gasoline, alkalis and dilute acids.

D4 Compressor Drawings

This section contains detail and assembly drawings used to manufacture the compressor.

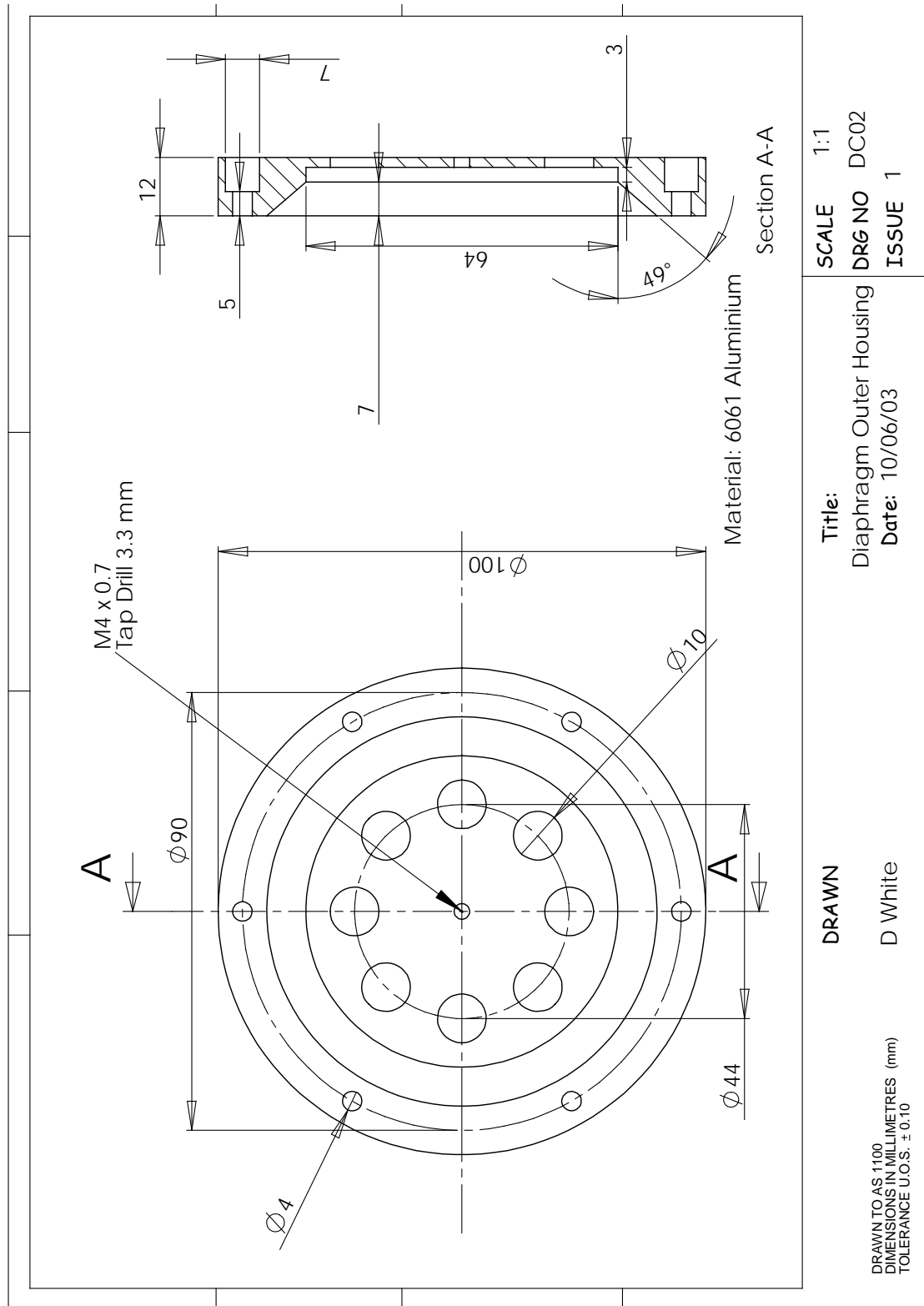
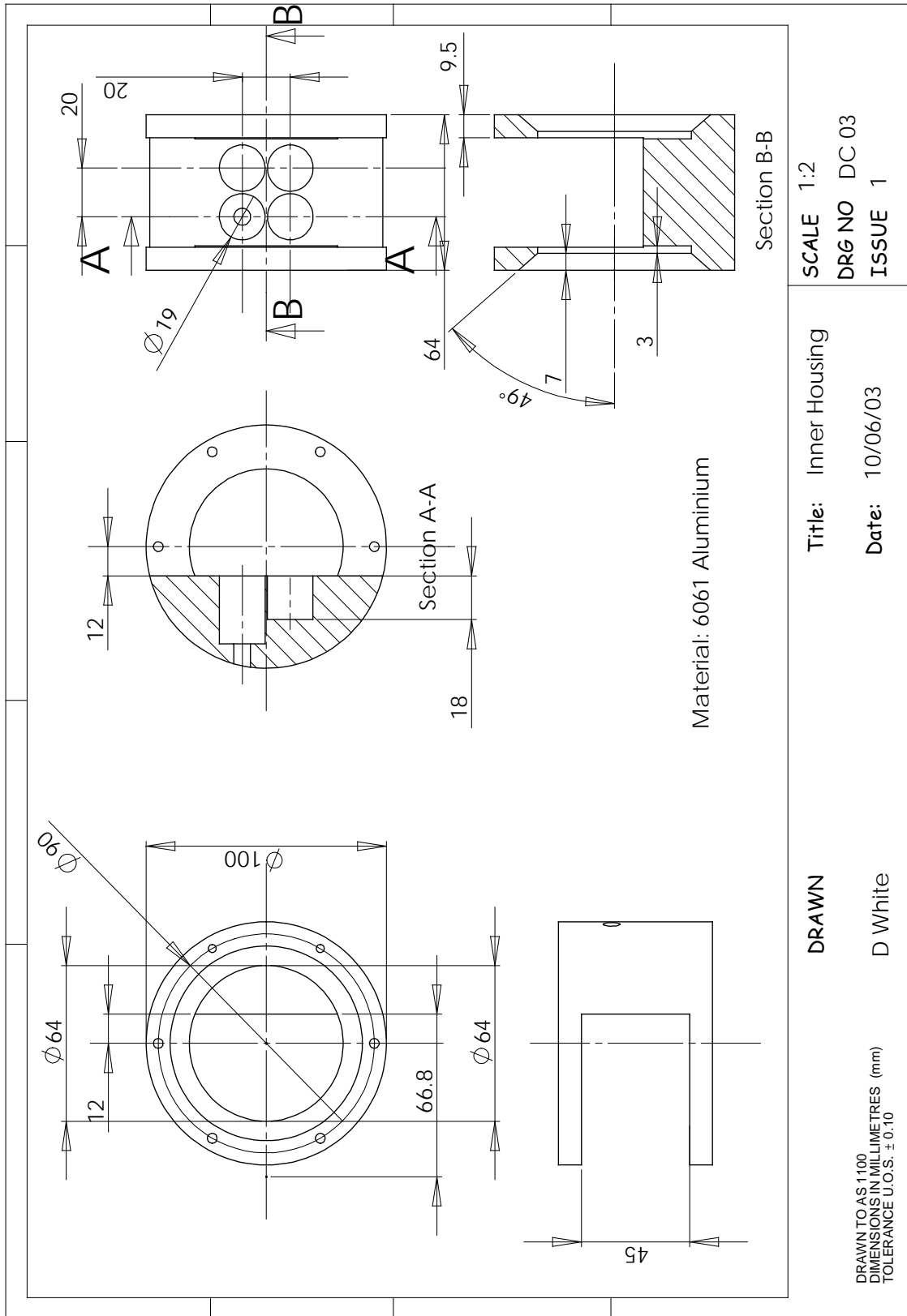


Figure D1 Detail drawing of diaphragm outer housing.



SCALE 1:2
 DRG NO DC 03
 ISSUE 1

Title: Inner Housing
 Date: 10/06/03

DRAWN
 D White

DRAWN TO AS 1100
 DIMENSIONS IN MILLIMETRES (mm)
 TOLERANCE U.O.S. ± 0.10

Figure D2 Detail drawing of inner housing.

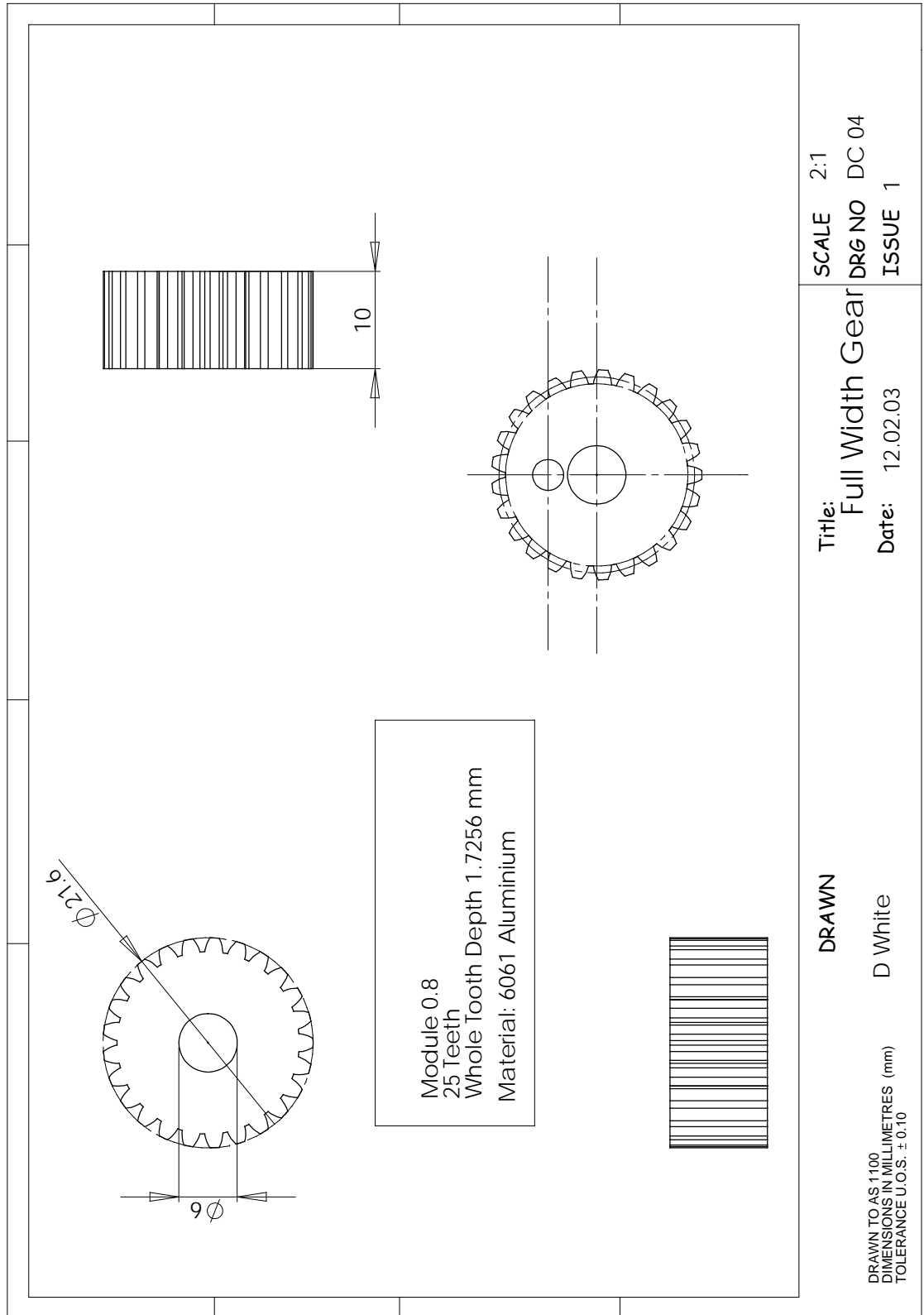


Figure D3 Detail drawing of full width gear.

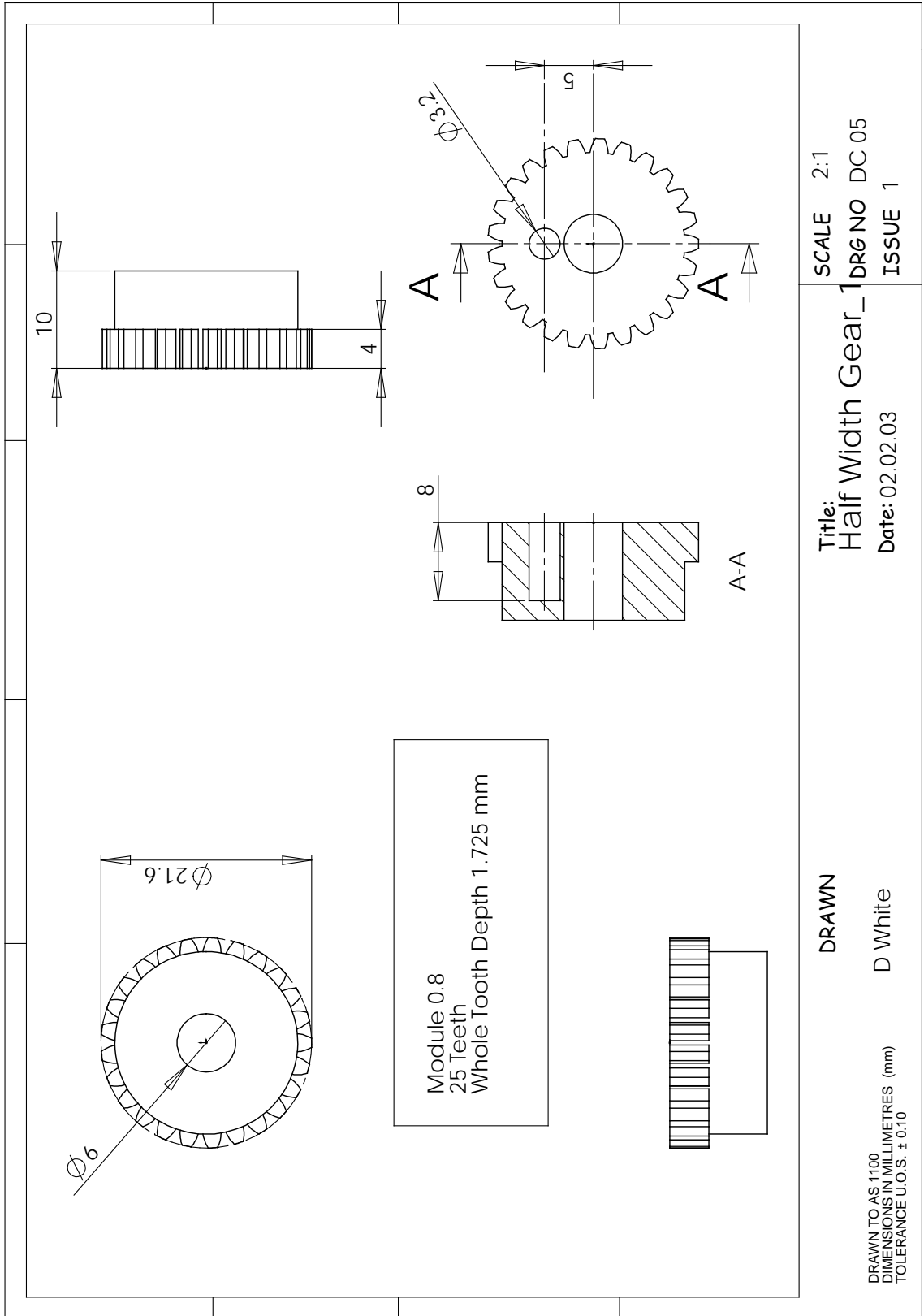


Figure D4 Detail drawing of half width gear_1.

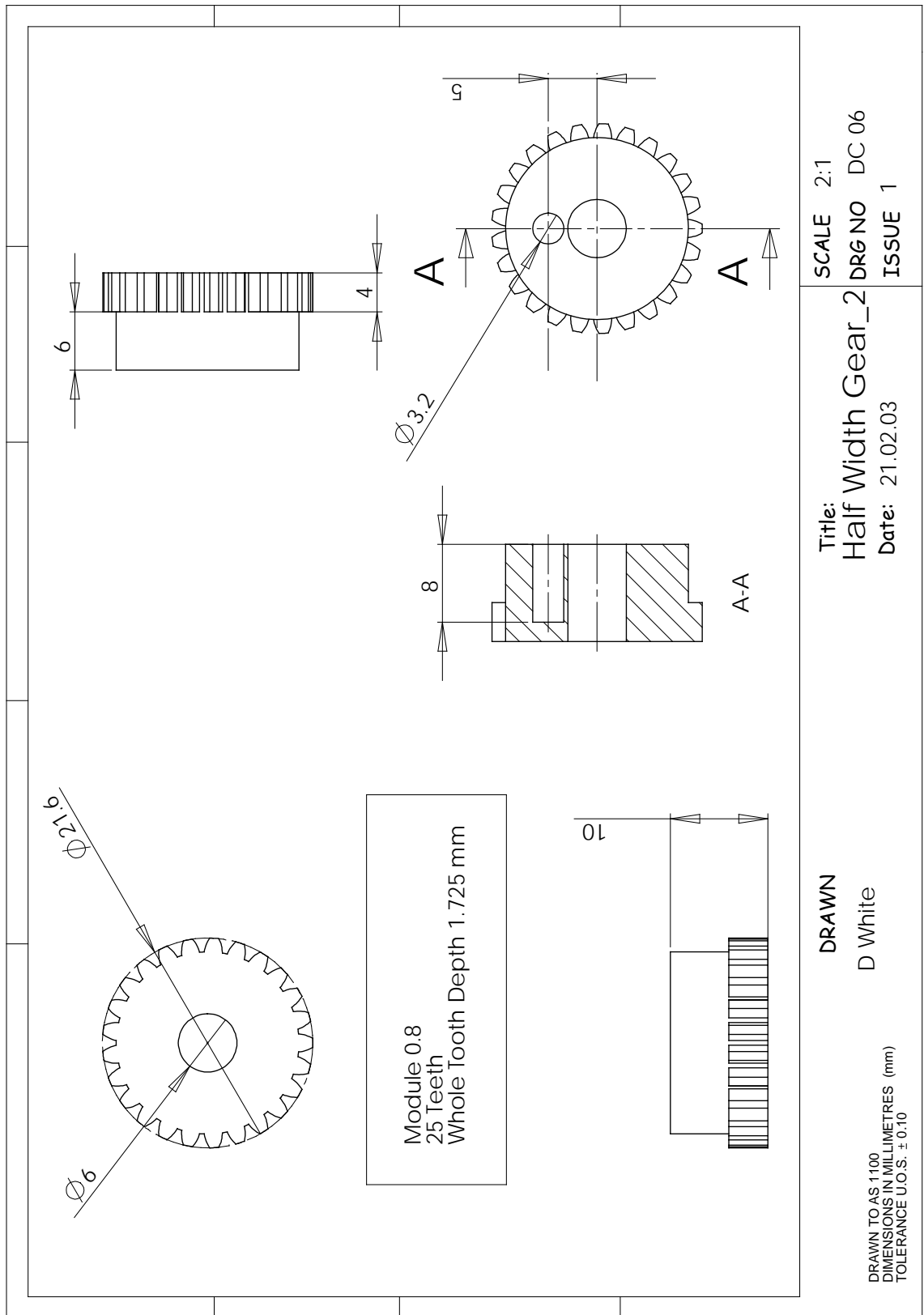


Figure D5 Detail drawing of half width gear_2.

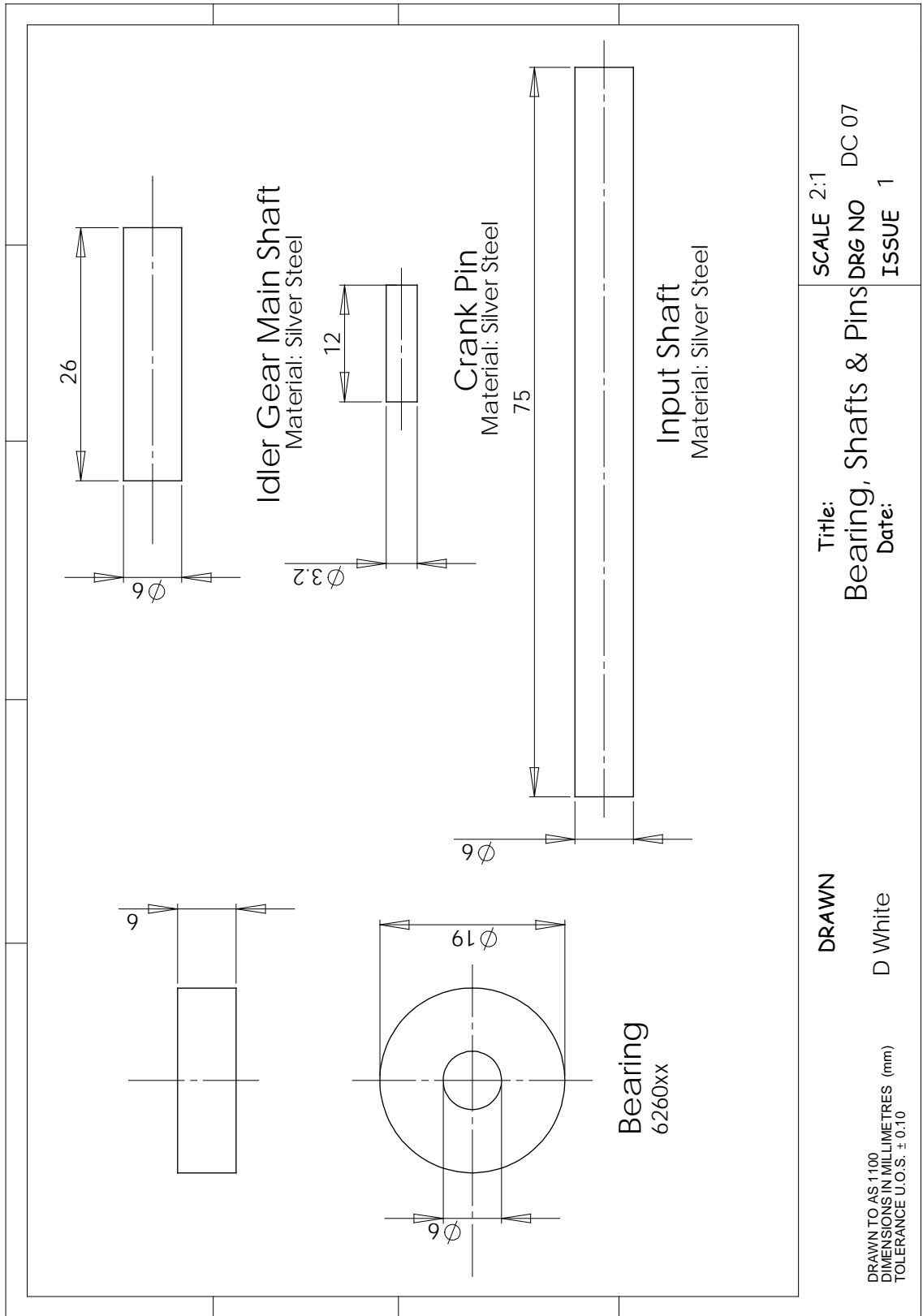


Figure D6 Detail drawing of bearing, shafts and pins.

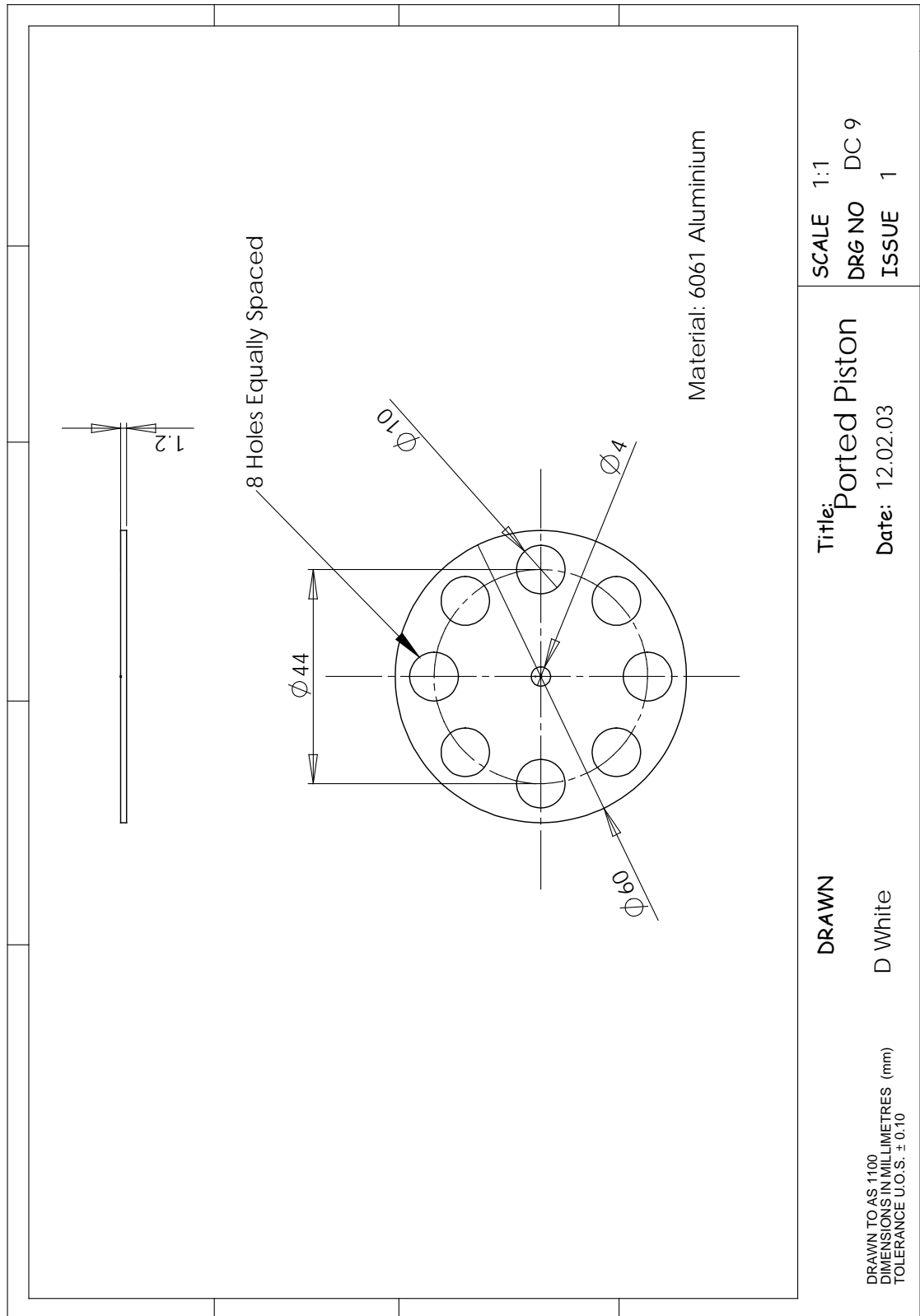


Figure D8 Detail drawing of ported piston.

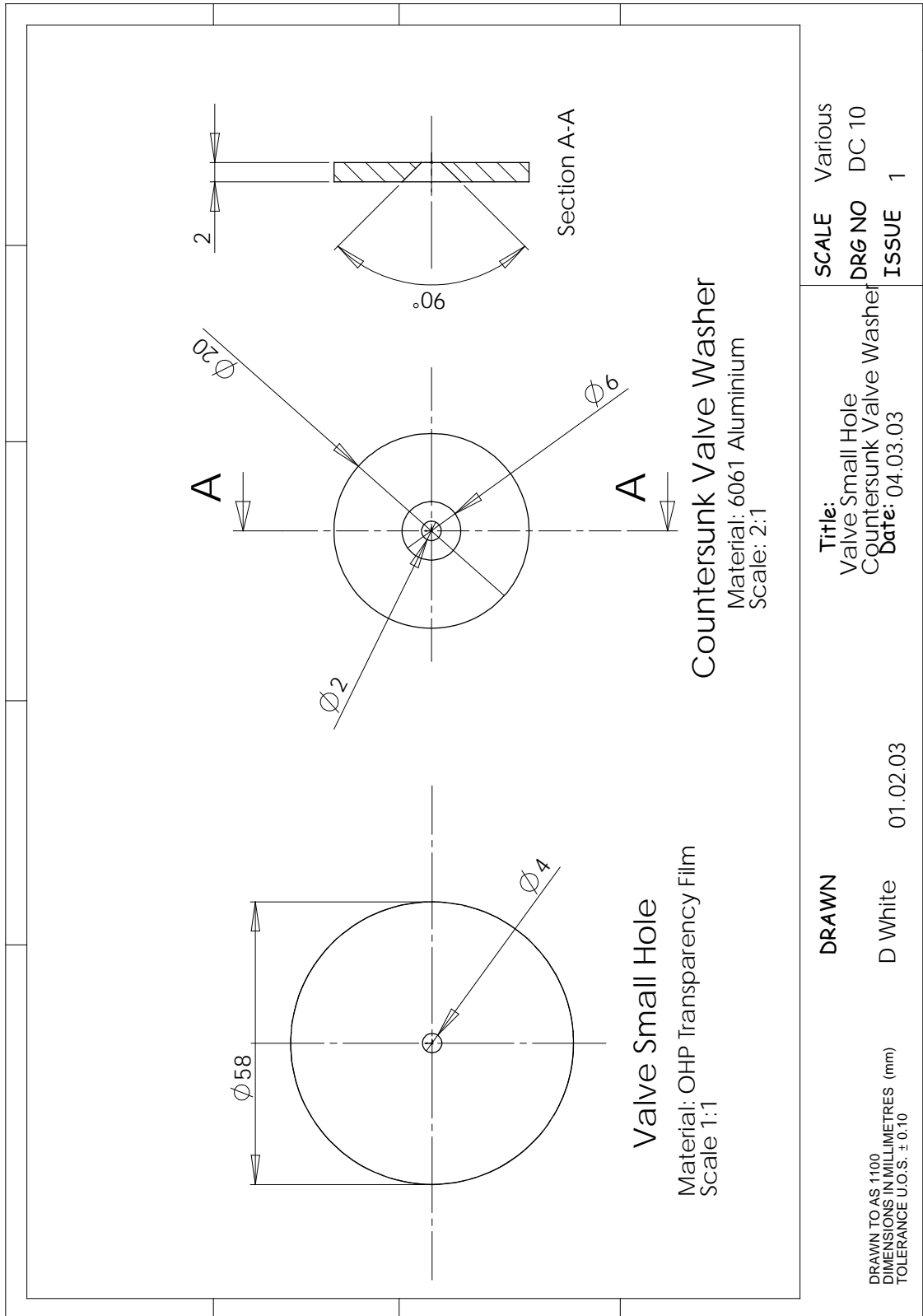


Figure D9 Detail drawing of valve small hole and countersunk washer.

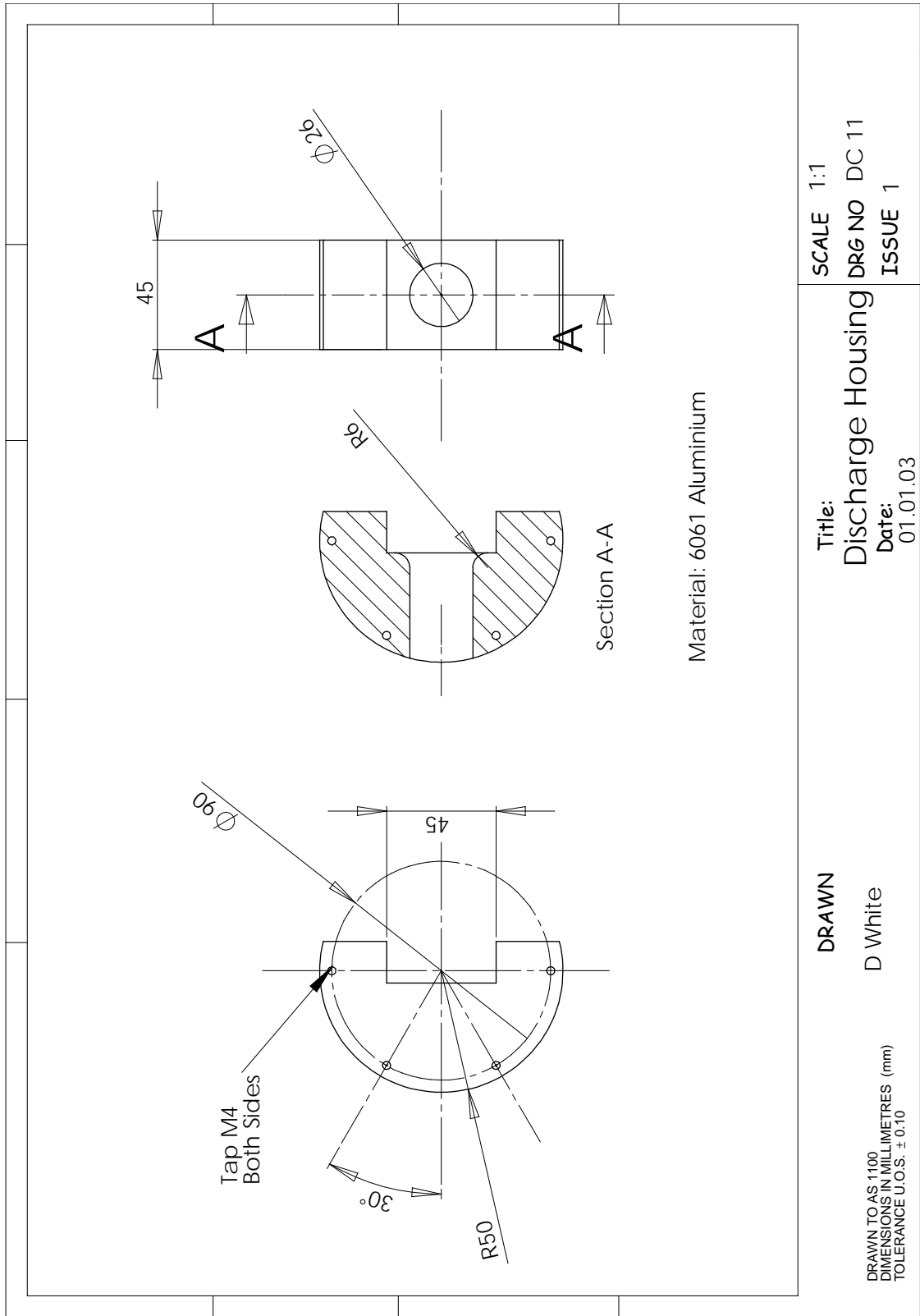


Figure D10 Detail drawing of discharge housing.

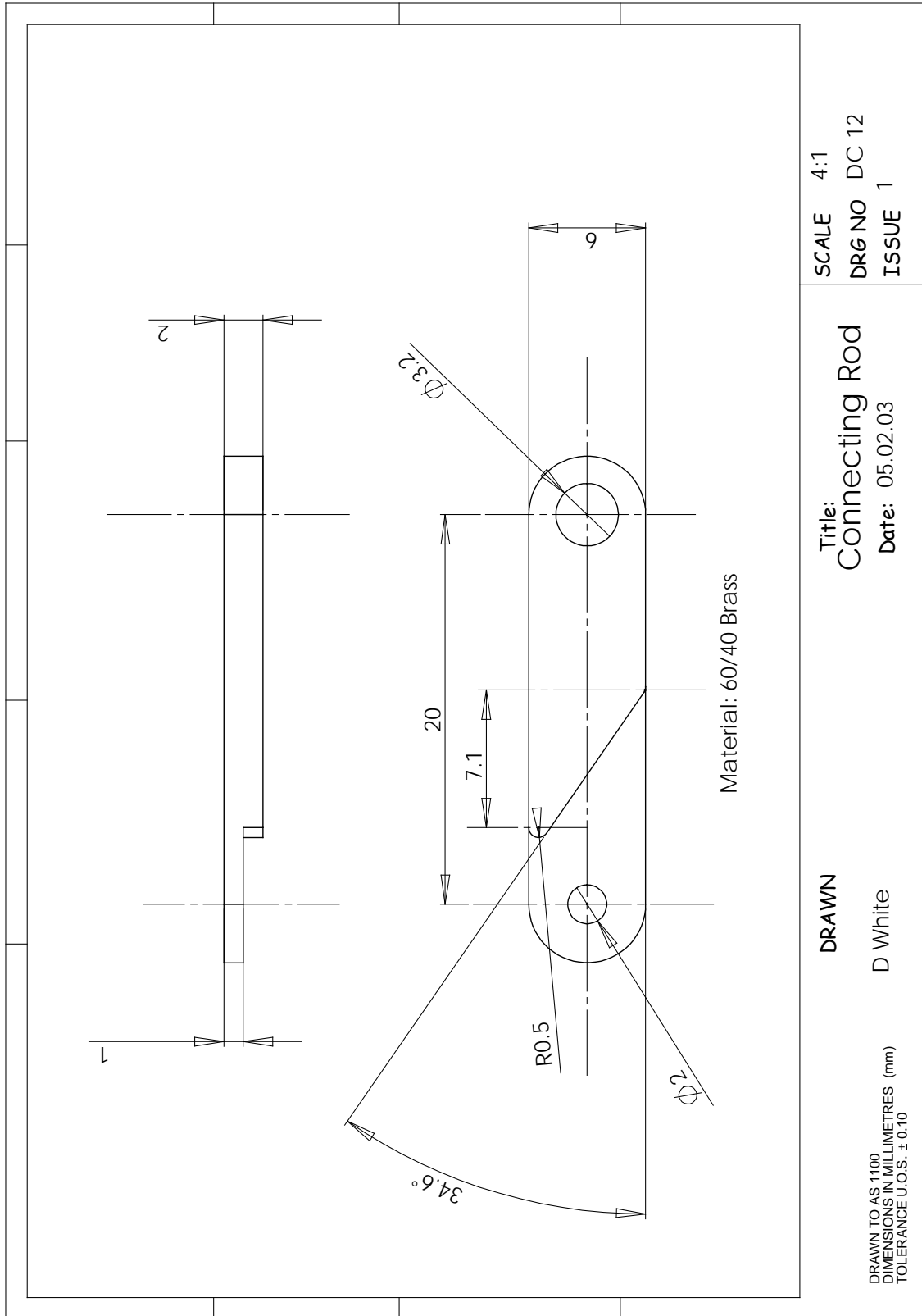


Figure D11 Detail drawing of connecting rod.

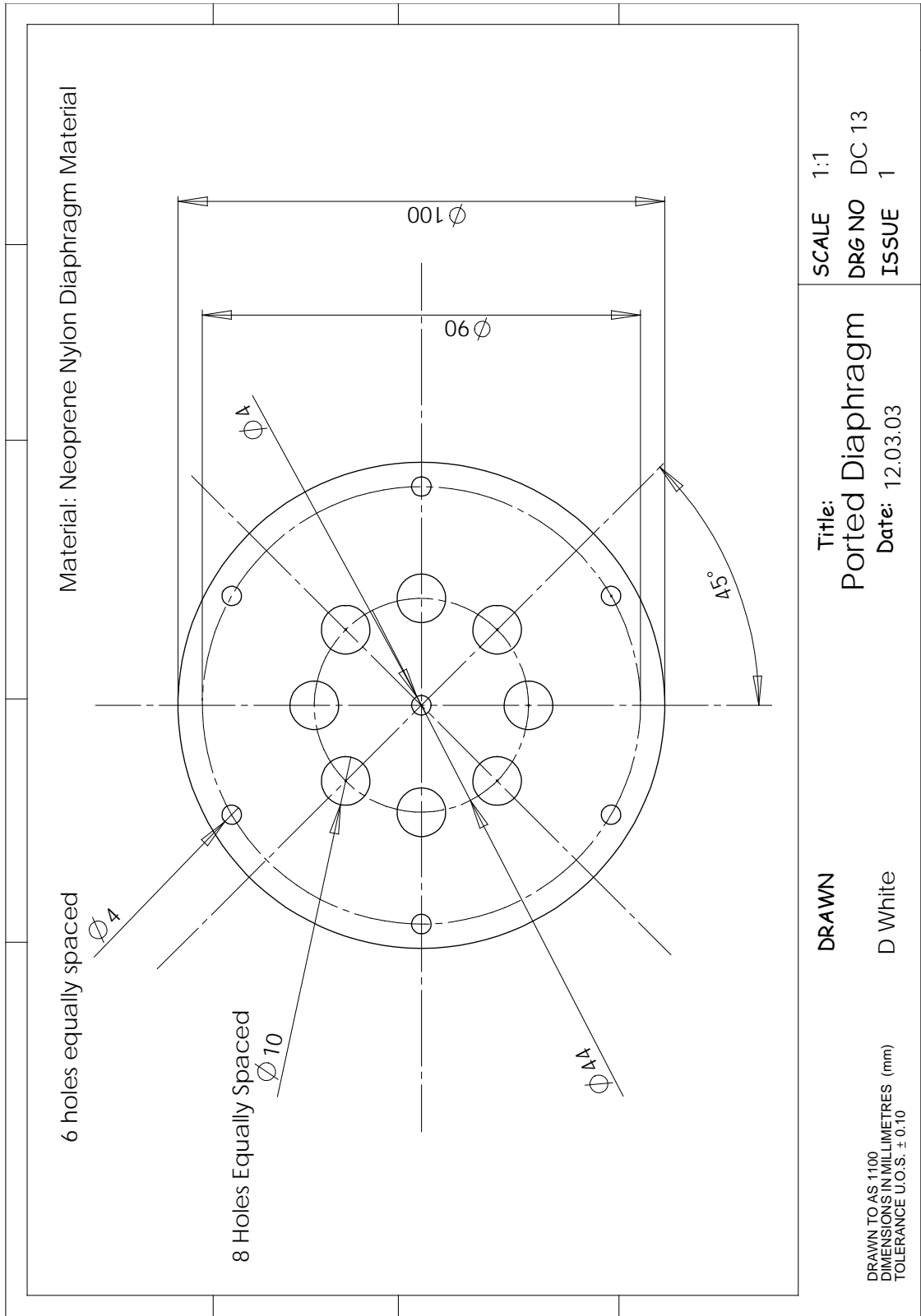


Figure D12 Detail drawing of ported diaphragm.

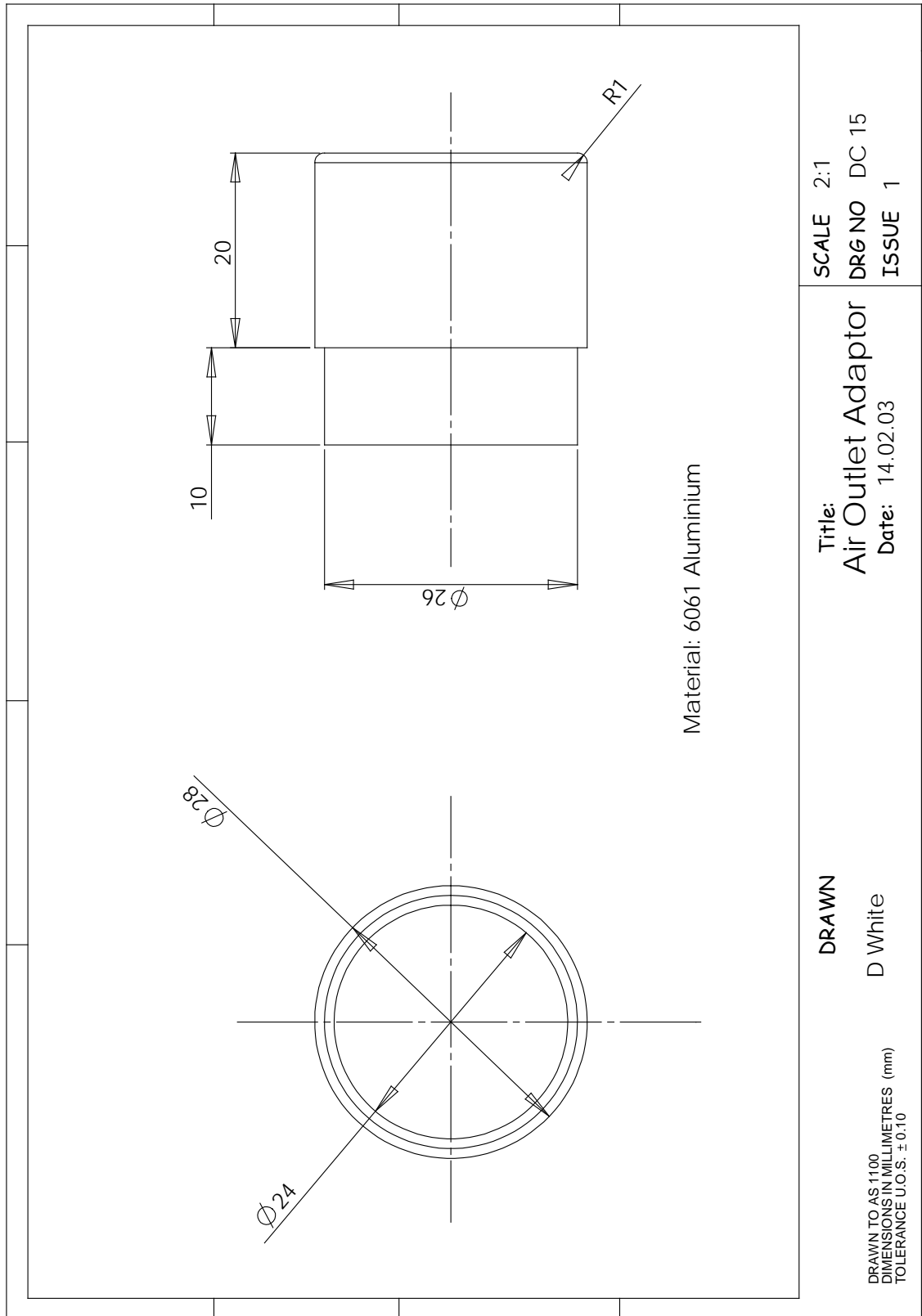


Figure D14 **Detail drawing of air outlet adaptor.**

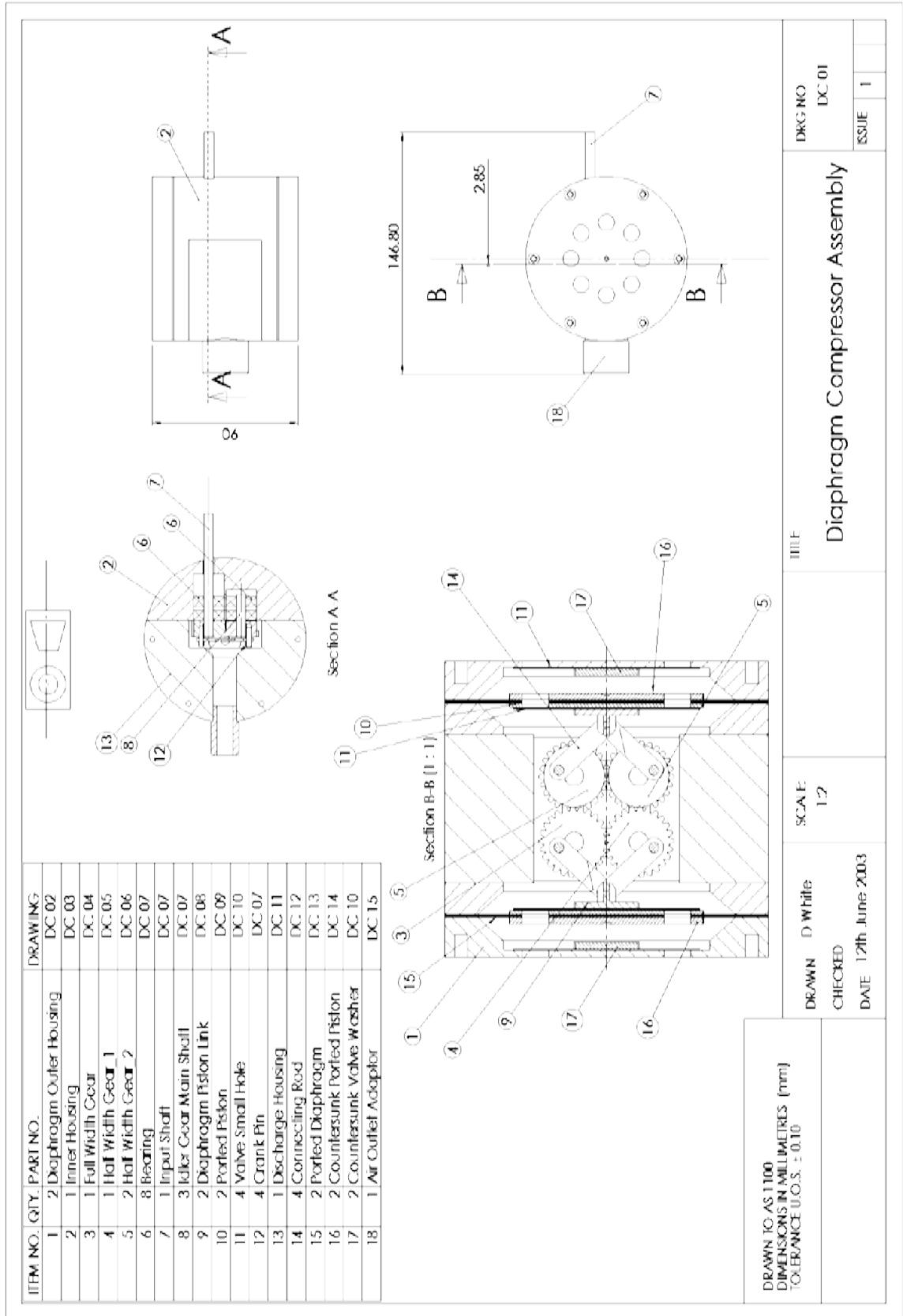


Figure D15 Diaphragm compressor assembly.

Appendix E ADU Dynamic Test Data

Introduction

This appendix contains results of prototype system ADU dynamic testing.

E1 ADU Dynamic Test Results

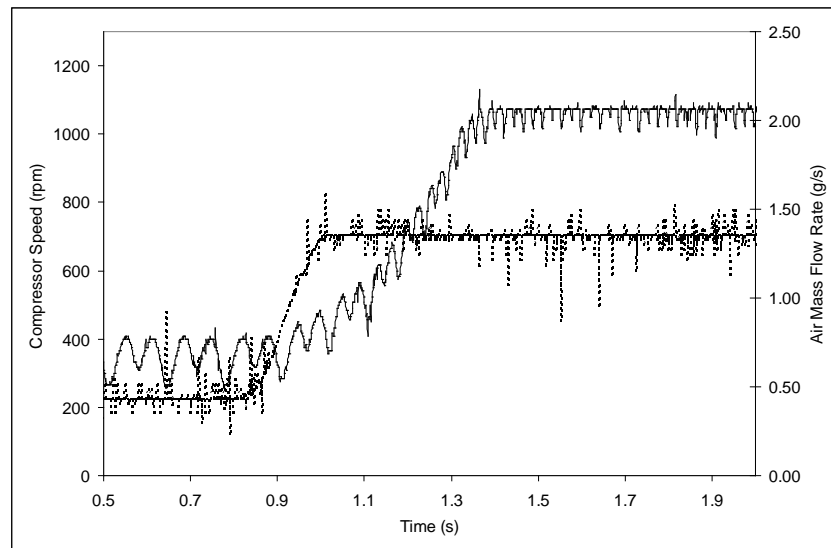


Figure E1 ADU response, test 1; ----- compressor speed, — compressor air mass flow.

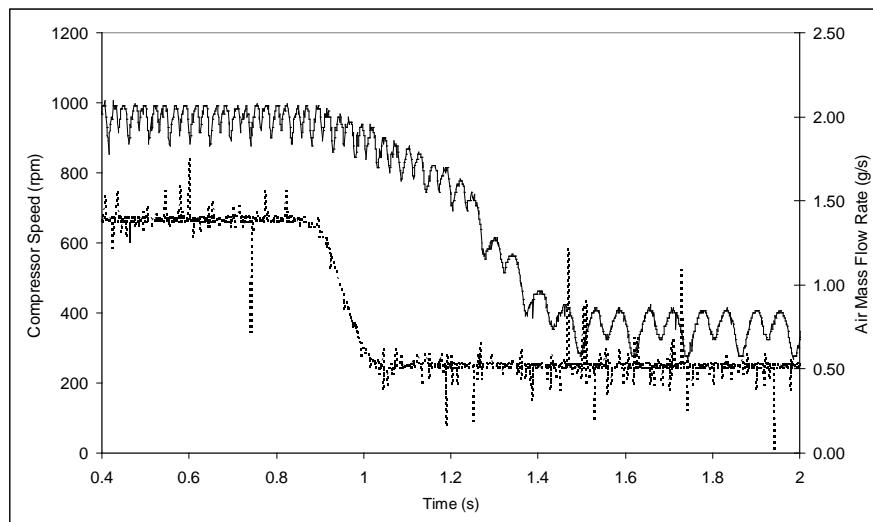


Figure E2 ADU response, test 2; ----- compressor speed, — compressor air mass flow.

Appendix F Mask Pressure Transducer

Introduction

This appendix contains manufacturer's information for the mask pressure transducer used within the prototype breathing system.

F1 Application Data

Configuration and features of mask pressure transducer is shown below in Table F1.

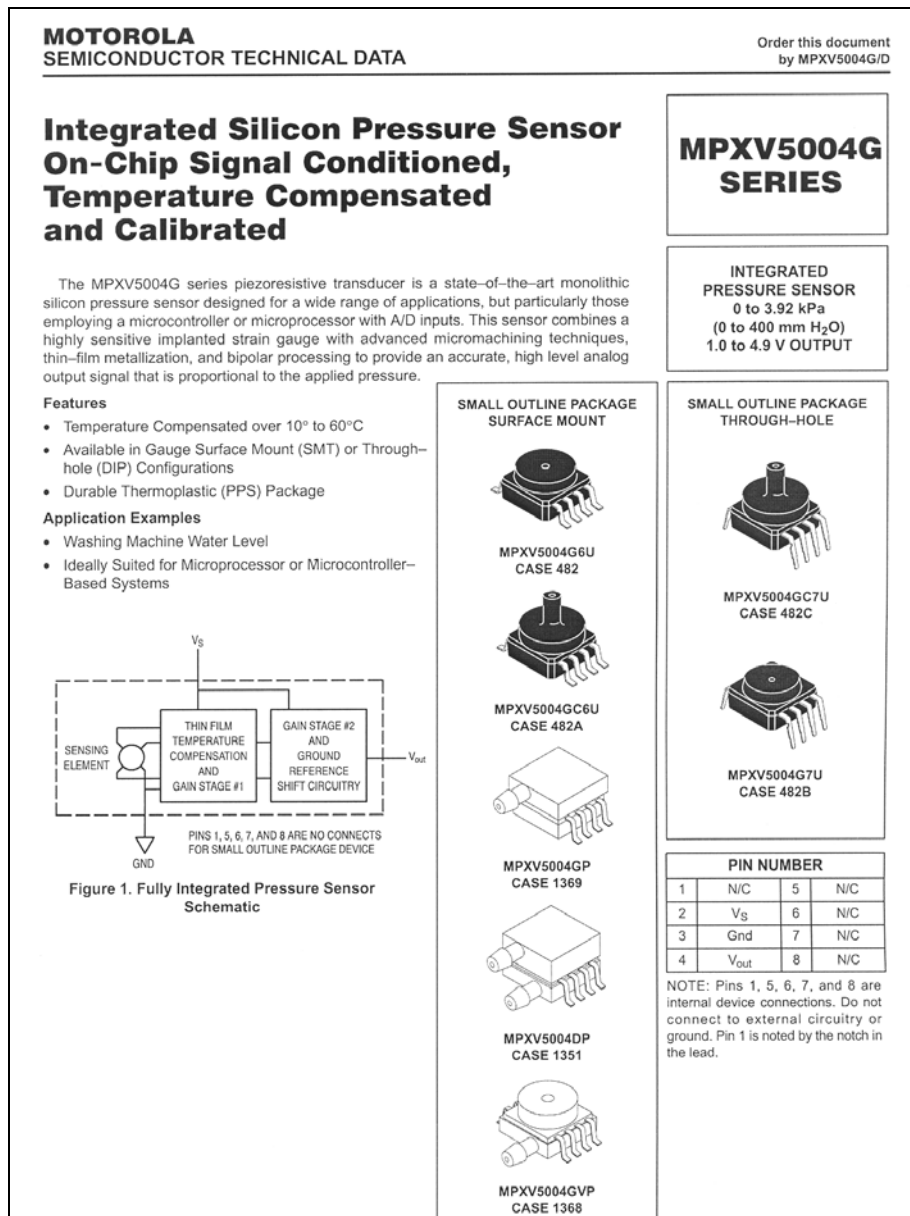


Figure F1 Motorola mask pressure transducer configuration data [71].

F2 Operating Characteristics

Operational Characteristics of mask pressure transducer is shown below in Table F2.

MPXV5004G SERIES						
MAXIMUM RATINGS(NOTE)						
Parameters	Symbol	Value	Unit			
Maximum Pressure (P1 > P2)	P_{max}	16	kPa			
Storage Temperature	T_{stg}	-30 to +100	°C			
Operating Temperature	T_A	0 to +85	°C			

NOTE: Exposure beyond the specified limits may cause permanent damage or degradation to the device.

OPERATING CHARACTERISTICS ($V_S = 5.0$ Vdc, $T_A = 25^\circ\text{C}$ unless otherwise noted, $P1 > P2$. Decoupling circuit shown in Figure 3 required to meet electrical specifications)

Characteristic	Symbol	Min	Typ	Max	Unit
Pressure Range	P_{OP}	0	—	3.92 400	kPa mm H ₂ O
Supply Voltage ⁽¹⁾	V_S	4.75	5.0	5.25	Vdc
Supply Current	I_S	—	—	10	mAdc
Span at 306 mm H ₂ O (3 kPa) ⁽²⁾	V_{FSS}	—	3.0	—	V
Offset ⁽³⁾⁽⁵⁾	V_{off}	0.75	1.00	1.25	V
Sensitivity	V/P	—	1.0 9.8	—	V/kPa mV/mm H ₂ O
Accuracy ⁽⁴⁾⁽⁵⁾	0 to 100 mm H ₂ O (10 to 60°C) 100 to 400 mm H ₂ O (10 to 60°C)	—	—	—	±1.5 ±2.5 % V_{FSS} % V_{FSS}

NOTES:

- Device is ratiometric within this specified excitation range.
- Span is defined as the algebraic difference between the output voltage at specified pressure and the output voltage at the minimum rated pressure.
- Offset (V_{off}) is defined as the output voltage at the minimum rated pressure.
- Accuracy (error budget) consists of the following:
 - Linearity: Output deviation from a straight line relationship with pressure over the specified pressure range.
 - Temperature Hysteresis: Output deviation at any temperature within the operating temperature range, after the temperature is cycled to and from the minimum or maximum operating temperature points, with zero differential pressure applied.
 - Pressure Hysteresis: Output deviation at any pressure within the specified range, when this pressure is cycled to and from the minimum or maximum rated pressure, at 25°C.
 - Offset Stability: Output deviation, after 1000 temperature cycles, -30 to 100°C, and 1.5 million pressure cycles, with minimum rated pressure applied.
 - TcSpan: Output deviation over the temperature range of 10 to 60°C, relative to 25°C.
 - TcOffset: Output deviation with minimum rated pressure applied, over the temperature range of 10 to 60°C, relative to 25°C.
 - Variation from Nominal: The variation from nominal values, for Offset or Full Scale Span, as a percent of V_{FSS} , at 25°C.
- Auto Zero at Factory Installation: Due to the sensitivity of the MPXV5004G, external mechanical stresses and mounting position can affect the zero pressure output reading. Autozeroing is defined as storing the zero pressure output reading and subtracting this from the device's output during normal operations. Reference AN1636 for specific information. The specified accuracy assumes a maximum temperature change of ± 5° C between autozero and measurement.

Figure F2 Motorola mask pressure transducer operating characteristics [71].

F3 Compensation, Calibration and Signal Conditioning

Temperature compensation, calibration and signal conditioning data for the mask pressure transducer are shown below in Table F3.

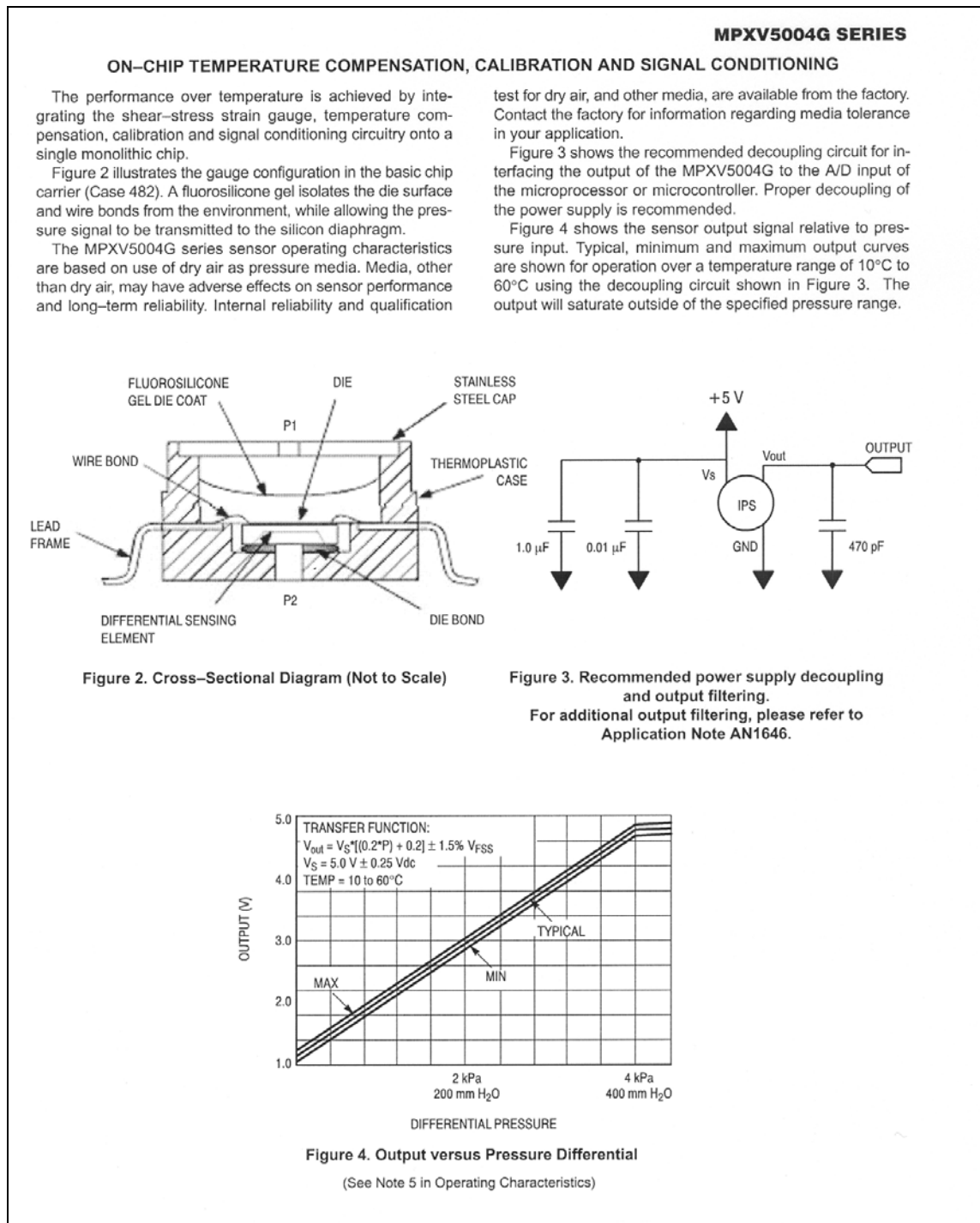


Figure F3 Motorola mask pressure transducer compensation, calibration and conditioning data [71].

References

- 1 Sleep Foundation. *Sleep Apnea*. WWW document (<http://www.sleepfoundation.org/publications/sleepap.html>). Accessed 12/12/02.
- 2 Várady, P., Micsik, T., Benedek, S. et al., (2002). *A Novel Method for the Detection of Apnea and Hypopnea Events in Respiration Signals*. IEEE Transactions on Biomedical Engineering **(49)** September, No. 9. p936-942.
- 3 American Academy of Family Physicians, (1999), *Obstructive Sleep Apnea*. American Family Physician, November 15. WWW document (<http://www.aafp.org/afp/991115ap/2279.html>.) Accessed 03/05/02.
- 4 American Medical Association, (1999). *Sleep Apnea Guidelines*. JAMA, April, (281) No. 16, p1480.
- 5 Piccirillo, J., Duntley, S., Schotland, H., (2000). *Obstructive Sleep Apnea*. JAMA September 27 **(284)** No 12. P1492-1494.
- 6 Demko, B. *Sleep Apnea Dentistry Using Oral Appliances. Mandibular Repositioning Devices*: WWW document (<http://sleepapneadentist.com/MRD-info.html>.) Accessed 12/05/02.
- 7 Teschler H., Berthon-Jones M., Thompson A.B., et al., (1996). *Automated Continuous Positive Airway Pressure Titration for Obstructive Sleep Apnea Syndrome*. Am J. Respir Crit Care Med. **(154)** p734-740.

- 8 Fisher and Paykel HealthCare. *Obstructive Sleep Apnea Product Range – HC220LE Series*. WWW document (<http://www.fphcare.com/osa/gppproduct.asp#-hc211>.) Accessed 04/03/02.
- 9 Verse, T., Pirsig, W., Stuck, B. et al., (2003). *Recent Developments in the Treatment of Obstructive Sleep Apnea*. American Journal in Respiratory Medicine, (2), No.2, p157-168.
- 10 CPAP SuperStore. *Fisher & Paykel Aclaim Mask 2*. WWW document (http://-cpapsuperstore.com/Merchant2/merchant.mvc?Screen=PROD&Product_Code=900HC401A&Category_Code=F%26PNasal+Mask.) Accessed 13/03/02.
- 11 Behbahani K., Yen F-C, Burk J.R. et al, (1995). *Automatic Control of Airway Pressure for Treatment of Obstructive Sleep Apnea*. IEEE Transactions on Biomedical Engineering, (42) 10th October, p1007-1016.
- 12 Bennett L., Davies, R., Stradling, J., (1998). *Oral Appliances for the Management of Snoring and Obstructive Sleep Apnea*. Thorax (53) Supplement 2:S58-64.
- 13 Metzger N., Kirbas G., Matthys, H., et al, (1997). *Technical Differences Between Common CPAP and Bilevel-CPAP Devices*. Pnuemologie (51), p789-795.
- 14 Lofaso, F, Heyer, L., Leroy, A. et al., (1994). *Do Turbines with Servo-Controlled Speed Improve Continuous Airway Pressure Generation*. European Respiratory Journal (7), p2077-2081.
- 15 Schäfer H., Ewig S., Hasper E., et al., (1998). *Failure of CPAP Therapy in Obstructive Sleep Apnea Syndrome: Predictive Factors and Treatment With Bilevel-Positive Airway Pressure*. Respiratory Medicine (92) p208-215.
- 16 Behbahani K., and Kang T.-H., (1989). *A Microprocessor-Based Sleep Apnea Ventilator*. Proceedings of the IEEE Engineering in Medicine & Biology Society 11th Annual International Conference. CH2770-6/89/0000-0332.

- 17 Nishimura, M., Takezawa, J., Imanaka H., et al., (1989). *Jet Flow-Regulated Expiratory Resistance to Maintain Constant CPAP During the Entire Respiratory Phase*. Chest, **(95)**, No4, April, p876-880.
- 18 Berry, R., Randall, M., (2002). *Auto-CPAP (APAP) for Treatment of Obstructive Sleep Apnea*. Proceedings of the Second Joint EMBS/BMES Conference Houston, Texas, October 23-26.
- 19 HÖk B., (1996). *Acoustic Sensors for Respiratory Air Flow From Basic Principles to Clinical Evaluation and Industrialization*. Proceedings of the 18th Annual Conference of the IEEE Engineering in Medicine and Biology Society, p 2152-2153.
- 20 Sinha S. and Donn S., (2001). *Volume-Controlled Ventilation: Variations on a Theme*. Clinics in Perinatology, **(28)** No 3, September 2001, p547-560.
- 21 Nikischin W., Gerhart T., Everett R., et al., (1996). *Patient-Triggered Ventilation: A Comparison of Tidal Volume and Chestwall and Abdominal Motion as Trigger Signals*. Pediatric Pulmonology, **(22)**, P28-34.
- 22 Várady, P., Bongár, S., and Benyó, Z., (2003). *Detection of Airway Obstructions and Sleep Apnea by Analysing the Phase Relationship of Respiration Movement Signals*. IEEE Transactions on Instrumentation and Measurement. **(52)** No.1 p2-6.
- 23 Guméry P.-Y., Levy P., Pepin, J.-L., et al. (1992). *Impedancemetry and Actimetry Sensors for Home Sleep Apnea Syndrome Monitoring*. Proceedings of the 14th Annual Conference of the IEEE Engineering in Medicine and Biology Society, p2618-2619.
- 24 D'Ortho M-P, Grillier-Lanoir V., Levy P., et al., (2000). *Constant vs Automatic Continuous Positive Airway Pressure Therapy*. Chest, **(118)** vol 4, p1010-1017.

- 25 Randerath W., Parys K., Feldmeyer F., et al., (1999). *Self Adjusting Nasal Continuous Positive Airway Pressure Therapy Based on Measurement of Impedance*. Chest, (116) No 4 October 1999. P991-999.
- 26 Konermann M., Sanner B.M., Vyleta M., et al., (1998). *Use of Conventional and Self Adjusting Nasal Continuous Positive Airway Pressure for Treatment of Severe Obstructive Sleep Apnea Syndrome*. Chest (113) No 3, March 1998. P714-718.
- 27 Al-Jumaily, A. M., Mithraratne, P., A., (2000). *Dynamic Simulation of Artificial Breather*. Final Report, Diagnostics and Control Research Centre, July 2000.
- 28 Woods R. and Lawrence, K., (1997). *Modelling and Simulation of Dynamic Systems*. Prentice Hall, New Jersey, p135-156.
- 29 Shearer, J., Kulakowski, B., and Gardner, J., (1997). *Dynamic Modelling and Control of Engineering Systems*. Prentice Hall, New Jersey, p5-10.
- 30 Ogata, K., (1998). *System Dynamics*. Prentice Hall, New Jersey, p190-198.
- 31 Fox R. and McDonald A., (1994). *Introduction to Fluid Mechanics*. John Wiley & Sons, fourth edition, New York, P335.
- 32 Streeter, V.,L., Wylie, E.,B., and Bedford, K.,W., (1998). *Fluid Mechanics*. McGraw-Hill, Singapore, ninth edition, P 466.
- 33 Doebelin, E., O., (1996). *Measurement Systems – Application and Design*. McGraw-Hill, New York, Fourth Edition, p 475.
- 34 MatWeb. *Engineering Plastic Products, PVC Flexible Grade*. WWW document (<http://www.matweb.com/search/SpecificMaterial.asp?bassnum=O5642>) Accessed 22/11/02.

- 35 White, F., (1994). *Fluid Mechanics*. McGrall-Hill, New York, Third Edition, p 198.
- 36 Fox R., W., and McDonald, A.,T., (1994). *Introduction to Fluid Mechanics*. John Wiley & Sons, New York, Fourth edition, p524.
- 37 Bleier, F., P., (1998). *Fan Handbook: Selection, Application and Design*. McGraw-Hill, New York P7.47.
- 38 Morgan, G., T., (1986). *Regenerative Blowers: High Flow at Low Cost*. Machine Design, July 24th, p107-109.
- 39 Fuji Industries. *Ring Compressors and Vacuum Pumps*. WWW document (<http://airpowerproducts.com/fuji/index.html>.) Accessed on 29/08/02.
- 40 Kishibuchi, A., Nosaka, M.,and Fukanuma, T., (1999). *Development of Continuous Running, Externally Controlled Variable Displacement Compressor*. SAE Transactions, **108**, part1, p 1674-1679.
- 41 Hoskins, A.,K., and Harris, M.,R., (1997). *Applied Mechanical Design*. H & H Publishing, Victoria, Third edition, p.3.1 – 3.49.
- 42 Ledex Corporation. *Standard Linear Solenoid Functional Comparisons*. WWW document (http://ledex.com/frames/frame_Lin_Sol.html). Accessed on 20/10/02.
- 43 Copley Control Corporation. *Thrust Tube Motors*. WWW document (<http://www.copleycontrols.com/motion/downloads/pdf/QM0001.pdf>). Accessed on 21/10/02.
- 44 H2W Technologies, Inc. Quotation 24990, Ref Ted Scheumann, Obtained on 14/11/02.
- 45 California Linear Devices Inc. *Linear Induction Motors*. WWW document (<http://www.calinear.com/>) Accessed on 15/09/02).

- 46 Copley Control Corporation. *Thrust Tube Motors*. WWW document (<http://www.copleycontrols.com/motion/downloads/pdf/QM0001.pdf>) Accessed 21/10/02.
- 47 Anaheim Automation Inc. *23A & 34A Series Linear Actuators*. WWW document (<http://www.anaheimautomation.com/23A34Aactuators.htm>) Accessed on 21/10/02.
- 48 Ledex Corporation. *BTA Series Brushless Torque Actuators*. WWW document (http://ledex.com/frames/frame_Lin_Sol.html). Accessed on 22/10/02.
- 49 Ledex Corporation. *Ultimag Rotary Actuators*. WWW document (http://ledex.com/frames/frame_Lin_Sol.html) Accessed on 22/10/02.
- 50 Euclid Research. *Stepper motors*. WWW document (http://www.euclidres.com/apps/stepper_motor/stepper.html). Accessed 24/10/02.
- 51 Kissell, T., E. *Servomotors*. WWW document (<http://zone.ni.com/devzone/prenticehall.nsf/webmain/OB12FOC5C73B63008625680A>). Accessed 25/10/01.
- 52 The New Zealand Technical Correspondence Institute, (1981). *Electrical Theory and Practice*. P. D. Hasselberg Government Printer, Wellington. P213 – 226.
- 53 MatWeb. *Engineering Plastic Products, NylatronGS Nylon, Type 66, MoS2 filled, extruded*. WWW document (<http://www.quadrantepp.matweb.com/Specific-MaterialNew.asp?bassnum=P1SM21&group=Gen...>). Accessed 21/12/02.
- 54 Jones, D., J., and Ryffel, H., H., (1961). *Gear Design Simplified*. Third edition, Industrial Press Inc. New York.
- 55 NTN Corporation, (2001). *Ball and Roller Bearings*, Cat, no. 2200II/E.

- 56 Roton Industries. *Roton Technical and Industrial Products – 145 mm Centrifugal Fan*. WWW document (<http://www.ametektmd.com/products/productPDFs-/1200w.pdf>). Accessed 29/08/02.
- 57 KNF. *Air, Gas & Liquid Diaphragm Pumps for the OEM*. WWW document (<http://www.knf.com/pdfs/oembrochure.pdf>) Accessed 05/09/02.
- 58 Pepe, E. and Halfinger, G. *A New Technology for Metering Fluids in Medical Devices*. WWW document (<http://www.knf.com/magmetering.htm>) Accessed 04/09/02.
- 59 Festo Corporation. *Festo One-Way Flow Control Valve, 151564 GRLZ-1/8-NPT-RS-B*. WWW document (<http://catalog.festo.com/enu/asp/DefaultPSresult.asp?ID=175064&L=001>). Accessed 05/09/02.
- 60 Festo Corporation. *Festo Proportional Pressure Regulator 161160 MPPE-3-1/8-1-010-B*. WWW document (<http://catalog.festo.com/enu/asp/DefaultPSresult.asp?ID=161160&L=001>). Accessed 05/09/02.
- 61 Hoerbigeroriga Corporation. *Electronically Controlled Pressure Regulating Valves*. WWW document (http://www.hoerbigeroriga.com/pdf_working-/PIEZO1.pdf). Accessed 29/08/02.
- 62 Ledex Corporation. *STA® Series Tubular Solenoids*. WWW document (http://ledex.com/frames/frame_Lin_Sol.html). Accessed 20/11/02.
- 63 Parker Hannifin Corporation. *L Series Microstepping Linear Motor Drive*. WWW document (<http://www.parker.com/parkersql/series1.asp?id=1893>). Accessed 21/11/02.
- 64 Simpson, C., D., *Types of Stepper Motors (detailed)*. WWW resource (<http://zone-ni.com/devzone/prenticehall.nsf/webmain/786DCA29F029AE588625688...>). Accessed 15/10/02.

- 65 MOOG. *Brushless Servo Motors*. WWW resource (<http://www.moog.com/Media-1/g410.pdf>) Accessed 26/10/02.
- 66 M.T. Motori Elettrici. (2000). *Technical Data - Electric Motors*. p 20.
- 67 Taian Electric Co. Ltd. *Microprocessor controlled Variable-frequency AC motor Drive User's Manual – V2 Series*.
- 68 MatWeb. *KKPC Kumho GP 125H High Transparency GPPS, Korea Kumho Petrochemical C. Ltd.* WWW document (<http://www.matweb.com/search/-SpecificMaterialPrint.asp?bassnum=PKKPCS10...>). Accessed 14/02/03.
- 69 MatWeb. Quadrant Engineering Plastics, Nylatron® GS Nylon, Type 66, MoS2 filled, Extruded. WWW document (<http://www.quadrantepp.matweb.com/-SpecificMaterialNew.asp?bassnum=P1SM21&group=Gen...>). Accessed 16/02/03.
- 70 Associated Gaskets NZ Ltd. *Material Specification Sheet - Neoprene Nylon Diaphragm Material*. Obtained 05/02/02.
- 71 Motorola Corporation. *MPXV5004 Intergrated Pressor Sensor*. WWW document (http://www.motorola.com/webapp/sps/site/prod_summary.jsp?code=MPXV5004&nodeId=01M98716). Accessed 21/02/03.